3-Axis Geomagnetic Magnetometer System Design Using Superconducting Quantum Interference Devices

Anton Theo Kilian

Thesis presented in partial fulfilment of the requirements for the degree Master of Engineering (Research) in the Faculty of Engineering at Stellenbosch University

Supervisor: Prof CJ Fourie
Department of Electrical & Electronic Engineering

April 2014

Declaration

By submitting this thesis electronically, I declare that the entirety of the work contained therein is my own, original work, that I am the sole author thereof (save to the extent explicitly otherwise stated), that reproduction and publication thereof by Stellenbosch University will not infringe any third party rights and that I have not previously in its entirety or in part submitted it for obtaining any qualification.

December 2013

Abstract

This work discusses the design of a 3-axis Geomagnetometer SQUID System (GSS), in which HTS SQUIDs are used unshielded. The initial GSS installed at SANSA was fully operable, however the LN2 evaporation rate and SQUID orientation required improving. Magnetic shields were also developed in case the SQUIDs would not operate unshielded and to test the system noise with geomagnetic variations removed. To enable removing the double layer shield from the probes while the SQUIDs remain submerged in LN2, the shield was designed to disassemble. The shields proved to be effective, however due to icing the shields could not be removed without removing the SQUIDs from the LN2.

After initial installation the $1/f$ noise remains to be determined, but the noise of the unshielded measurements above 10 Hz was shown to be better than 400 fT/$\sqrt{\text{Hz}}$, close to the maximum shielded noise of 300 fT/$\sqrt{\text{Hz}}$, with $1/f$ noise lower than geomagnetic field variations. This is achieved with commercial HTS SQUIDs, before implementing any improvements, justifying the project's research validity. It is suggested that the Kibble-Zurek theory be researched in more depth, as it explains that the SQUID's cooling rate would have to be very low to reduce flux trapping and improve $1/f$ noise. Shielding SQUIDs from high frequency EMR is also very important to improve the modulation depth and reduce $1/f$ noise.

Opsomming

Hierdie werk bespreek die ontwerp van 'n 3-as Geomagnetometer SQUID Sisteem (GSS), waarin HTS SQUIDs sonder magnetiese skilde aangedryf word. Die aanvanklike GSS geïnstalleer by SANSA was ten volle binnewerking, maar die LN2 verdamping en SQUID oriëntasie benodig verbetering. Magnetiese skilde was ook ontwikkel vir die geval dat die SQUIDs nie sonder skilde wou werk nie en om die ruis te toets na geomagnetiese variasies verwyder is. Die dubbele laag skild was ontwerp om uitmekaar gehaal te word terwyl die SQUIDs binne die LN2 bly. Die skild was doeltreffend, maar ys het verhoed dat die skild verwyder kon word vanaf die LN2 sonder om die SQUIDs ook te verwyder.

Na die aanvanklike installasie moet die $1/f$ ruis nog bepaal word, maar bo 10 Hz was die ruis minder as 400 fT/$\sqrt{\text{Hz}}$, na aan die maksimum magnetiese geskilde ruis van 300 fT/$\sqrt{\text{Hz}}$, met $1/f$ ruis laer as geomagnetiese veld variasies. Dit word bereik met kommersiële HTS SQUIDs, voor die implementering van enige verbeterings, en regverdig die projek se navorsing geldigheid. Daar word voorgestel dat die Kibble-Zurek teorie in meer diepte ondersoek word, want dit verduidelik dat die SQUID se koel tempo baie laag moet wees om minder magneetvloed vas te vang en $1/f$ ruis te verminder. Dit is ook belangrik om SQUIDs vanaf hoë frekwensie EMR te beskid, om die SQUID uittree te maksimeer en sodoende $1/f$ ruis te verminder.

Acknowledgements

I would like to express my sincere gratitude to the following people and organisations:

Prof. Coenrad J. Fourie (Associate Professor at E&E Engineering, Stellenbosch University), for giving me the opportunity to work on this project, for providing continual guidance and for his easy-going work ethic.

Wessel Croukamp (Chief Electronician at E&E Engineering), for his expert mechanical design advice, willingness to help and for putting in extra time to finish the manufacturing of the SQUID-lift.

Lincoln P. R. Saunders (Junior Technical Officer at E&E Engineering), for his expert machining skills and many hours spent machining the SQUID-lift and magnetic shield parts, as well as helping me fiddle with machining parts for a simple nitrogen ventilation system.

SANSA Space Science (Hermanus) for helping with installation, operating the SQUIDs and graciously providing me with data when requested.

Emile Lochner (Student at E&E Engineering), for his contribution to the project, helping to install the SQUID-lift and for his prompt response when information was needed.

Lucas Janse van Vuuren (Student at E&E Engineering), for programming and putting together the DAQ-system.

The National Research Foundation, for helping fund the project and my studies.

Lastly I would like to thank my parents, Anton and Amanda Kilian, for their ever enduring patience, providing me with moral and financial support through my years of study.

Table of Contents

Declaration i

Abstract ii

Opsomming iii

Acknowledgements iv

Table of Contents v

List of Figures viii

List of Tables x

Nomenclature xi

Chapter 1 Introduction 1

1.1 Background and Motivation 1

1.2 Project Goals 2

1.3 Thesis Overview 3

Chapter 2 Literature Review 4

2.1 Electromagnetic Fields 4

2.1.1 Electromagnetic Field Overview 5

2.1.2 Real photons and virtual photons 6

2.1.3 EM propagation parameters 8

2.1.4 Near-field and Far-field 11

2.2 Geomagnetic Field Spectrum 15

2.3 Superconductivity and SQUIDs 17

2.3.1 Superconductivity 17

2.3.2 Quantum Interference 26

2.3.3 SQUIDs 30

2.4 Magnetic and EMR Shielding 40
2.4.1 EMR Shielding 40
2.4.2 Magnetic Shielding 44
2.5 Literature Review Conclusion 49

Chapter 3 Design and Installation of the Geomagnetometer SQUID System 50

3.1 Data Acquisition System Requirements 51
3.1.1 Field Resolution and Dynamic Range 52
3.1.2 Timing Resolution and Accuracy 55
3.1.3 Data Acquisition System Conclusion 57
3.2 3-Axis SQUID System 59
3.2.1 SQUID-lift Design Considerations 61
3.2.2 3-Axis SQUID System Conclusion 64
3.3 Magnetic Shield Design 67
3.3.1 Design Considerations 67
3.3.2 Dimension Optimisation Simulation 69
3.3.3 Magnetic Shield Design Conclusion 71

Chapter 4 Performance Analysis and Recommendations 73

4.1 Magnetic Shield Performance 73
4.2 3-axis SQUID System Performance 74
4.3 Calibration and Slew Rate 76
4.4 DAQ-system Noise 82
4.5 SQUID Thermal Cycling 88
4.6 Recommendations Summary 90

Chapter 5 Conclusion 91

List of References 92

Appendices 97

A.1. Matlab Code: Magnetic Shielding 98
A.2. Matlab Code: Amplitude Spectral Density 102
A.3. SQUID vs. Fluxgate Correlation 103
B.1. Datasheet: M2700 SQUID 105
B.2. Datasheet: Z-axis SQUID Calibration Certificate 108

B.3. Datasheet: X-axis SQUID Calibration Certificate 109
B.4. Datasheet: Bio34 Dewar 110
B.5. Datasheet: Conetic Mu-metal 111

List of Figures

Figure 1: Different frequencies EMF propagation and evanescent fields. Blue lines are EMR, purple lines are the critical angles and red lines are evanescent fields. 14
Figure 2: Geomagnetic field spectrum. [9] 16
Figure 3: Schumann resonances spectrum at Silberborn. [11] 16
Figure 4: Band gaps of different materials. 18
Figure 5: Energy gap 2Δ($\boldsymbol{T}$)/2 in mV against normalised temperature $\boldsymbol{T/Tc}$. The solid line is the expected energy gap according to the BCS theory and the dots are the measured values for a HTS with $\boldsymbol{Tc}$ of 108K. [13] 20
Figure 6: Critical current density ($\boldsymbol{Jc}$) dependence on external magnetic field applied over a thin film of Nb, from temperatures 4.5K (top curve) to 8.5K (bottom curve). [14] 22
Figure 7: Magnetic flux quantisation in 'n superconducting ring. $\boldsymbol{Is}$ is the circulating supercurrent, moving with a coherent wave function. [12] 23
Figure 8: Vortex trapping in YBCO (HTS) film with different applied external magnetic fields. YBCO film is cooled down to 2K. 1mOe = 0.1μT [17] 25
Figure 9: Fraunhofer pattern, showing the dependence of $\boldsymbol{Ic}$ on magnetic flux penetrating a JJ. [18] 29
Figure 10: Dependence of $\boldsymbol{Ic}$ on magnetic fields perpendicular to a long LTS JJ. External magnetic field is enlarged by 0.5μT after every 50 cycles. 6.75μT ≈ 1$\boldsymbol{\Phi 0}$. [16] 29
Figure 11: SQUID modulation voltage $\boldsymbol{V(\Phi a)}$ normalised to $\boldsymbol{IcR}$, for several values of normalised current $\boldsymbol{i = IbIc}$. (a) and (c) are strongly over-damped SQUIDs ($\boldsymbol{\beta C \ll 1}$), (b) and (d) are intermediately damped. (a) and (b) are without thermal fluctuations, while (c) and (d) include noise from thermal fluctuations ($\boldsymbol{\Gamma > 0}$). [19] 34
Figure 12: Microwave radiation (390 MHz) of a HTS DC SQUID. Noise at 6 kHz (a) and $\boldsymbol{Vpp}$ (b) is plotted against different values of $\boldsymbol{Ib}$, for different amounts of radiation. [21] 36
Figure 13: Flux Locked Loop: (a) Small-signal SQUID output $\boldsymbol{V(\Phi a)}$, with workpoint indicated (b) Circuit diagram of a basic FLL. [19] 37
Figure 14: Sources of noise and modulation schemes. [19] 38

Figure 15: SQUID calibration curves locked to different working points..... 39
Figure 16: Plane-wave EMF propagation through a conductive medium. 41
Figure 17: 18-bit field resolution and dynamic range for the model M2700 SQUIDs. 54
Figure 18: SQUID specification requirements with ±10 V 18-bit DAQ, plotted for three different field resolutions. 54
Figure 19: SQUID-hut and 3-axis SQUID system. (1) SQUID-lift; (2) PFLs; (3) Probes; (4) SQUIDs; (5) SQUID-lift pillar; (6) Dewar. 60
Figure 20: SQUID-lift dimensions. 9 mm rubber flooring included. 30 mm wood block.. 66
Figure 21: Permeability curve-fit for Co-Netic AA perfection annealed Mu-metal. 69
Figure 22: Dimension optimisation of double layer shield. $\boldsymbol{r1}$ is 29 mm. Thickness ($\boldsymbol{t}$) is varied, while the outside radius ($\boldsymbol{r2}$) is varied in the top graphs and length ($\boldsymbol{l}$) is varied in the bottom graphs. Bottom graphs x-axis are the length to outside radius (40 mm) ratio. The transverse Shielding Factor does not account for flux leakage at shorter shield lengths. Shielding Factors are calculated at 77 K, with permeability reduced to 15% of room temperature permeability. The calculated room temperature shielding factors are roughly 37 times larger. 70
Figure 23: Magnetic Shield design. (1) Outer half-cylinder (2) Inner half-cylinder (3) Outer half cylinder lid (4) Inner half-cylinder lid. Layer thickness is 1 mm. 72
Figure 24: SQUID amplitude spectral density (ASD) using the 1 MΩ feedback resistors compared to the fluxgate spectrum. 76
Figure 25: SQUID and fluxgate comparison using 1 MΩ feedback resistor. 77
Figure 26: Z-axis SQUID and fluxgate data comparison. 5-7 February 2013. [35] 78
Figure 27: Illustration of -3 dB flux error. The slope of the modulation voltage at $\boldsymbol{\Phi a = 0.125\Phi 0}$ is 3 dB less than that of the transfer function. 79
Figure 28: Worst $\boldsymbol{f3dB}$ when selecting maximum $\boldsymbol{Rf}$ and $\boldsymbol{\tau}$ for two $\boldsymbol{\partial V \partial \Phi 0}$ values. 80
Figure 29: Magnetic field variations that exceed the slew rate, plotted for two values of SQUID calibration while assuming the worst possible slew rate. 82
Figure 30: DAQ-system noise spectrum (Amplitude Spectral Density) of unfiltered SQUID measurements for different feedback resistors. 84
Figure 31: Shielded SQUID measurements after immersion in LN2. Measurements started at 12:30 UTC on 4 November 2013. The amplitude spectral density given in dB. 85

Figure 32: DAQ-system shielded noise spectrum after shield settling time. Geomagnetic field variations are reduced by a factor larger than 50. 87
Figure 33: Internal SQUID noise before and after defluxing. 88

List of Tables

Table 3.1: DAQ-unit Specifications 58
Table 3.2: Materials for use in magnetically clean environments. 63
Table 4.1: SQUID electronics internal voltage noise spikes. 87

Nomenclature

Acronyms

1PPS:	One pulse per second, 58
AC:	Alternating current, 28
BCS:	Bardeen, Cooper and Schrieffer, 20
CED:	Classical electrodynamics, 6
DAQ:	Data acquisition, 39
DC:	Direct current, 27
EM:	Electromagnetic, 6
EMF:	Electromagnetic field, 5
EMI:	Electromagnetic interference, 43
EMR:	Electromagnetic radiation, 7
FLL:	Flux-Locked-Loop, 39
GSS:	Geomagnetometer SQUID system, 2
HTS:	High-temperature superconductors, 18
JJ:	Josephson Junction, 27
LN2:	Liquid-nitrogen, 63
LSB:	Least significant bit, 56
LSBB:	Laboratoire Souterrain à Bas Bruit, 2
LTS:	Low-temperature superconductors, 18
PCI:	Personal computer interface unit, 54
PFL:	Programmable feedback loop, 54
PVC:	Polyvinyl Chloride, 64
QED:	Quantum electrodynamics, 7
RF:	Radio frequency, 28
SANSA:	South African National Space Agency, 2
SQUIDs:	Superconducting quantum interference devices, 1
TCXO:	Temperature controlled crystal oscillator, 58
ULF:	Ultra Low Frequency, 1
UTC:	Universal Time Coordinated, 54
YBCO:	$YBa_2Cu_3O_7$, 29

Constants

c	Speed of light (299.7925×10^6 m/s)
h	Planck constant (6.6261×10^{-34} J · s)
k_B	Boltzmann constant (1.3807×10^{-23} J/K)
ϵ_0	Permittivity of free space (8.8542×10^{-12} F/m, (F/m = A · s/V · m))
Φ_0	Flux quantum (2.0678×10^{-15} Wb , (Wb = V · s))
μ_0	Permeability of free space ($4\pi \times 10^{-7}$ T · m/A , (T · m/A = Wb/A · m))

Frequently Used Symbols

T_c	Superconductor critical temperature (K)
I_c	Superconductor circuit critical current (μA)
$V(\Phi_a)$	SQUID modulation voltage (μV)
V_{pp}	SQUID modulation depth (μV)
$\partial V/\partial \Phi$	SQUID transfer function ($\mu V/\Phi_0$)
I_b	SQUID bias current (μA)
$1/f$	Low frequency (when referring to noise)
M_f	SQUID feedback coil mutual inductance (H = Wb/A)
$1/M_f$	SQUID feedback coil coupling ($\mu A/\Phi_0$)
R_f	SQUID feedback loop feedback resistor (Ω)
V/Φ_0	SQUID calibration (V/Φ_0)
SF	Shielding factor

Chapter 1

Introduction

1.1 Background and Motivation

Ultra Low Frequency (ULF) oscillations in the geomagnetic field are valuable sources of information. The ULF spectrum is internationally defined between 1 mHz and 1 Hz (different sciences may define different bandwidths), conveying information about the Earth's and its atmosphere's magnetohydrodynamics, as well as the sources of the ULF waves [1]. This information can be used to form predictive models for many different fields of study. The predictive models could also serve as early warning systems for natural hazards. Correlations between earthquakes and the intensity of ULF waves prior to earthquakes have been made, but require further study [2, 3]. ULF geomagnetic field research has however been limited due to the resolution of available geomagnetic field data. Currently most magnetic observatories are part of an international network called Intermagnet, which shares standardised geomagnetic field data with the public through a near real-time open data exchange webserver. Intermagnet observatories are required to have magnetometer resolutions of 0.1 nT, while ULF oscillation amplitudes roughly range between 1 pT and 20 nT (shown in Section 2.2). Therefore, this project stems from the need for a global network of ultra-sensitive geomagnetic magnetometers.

Superconducting quantum interference devices (SQUIDs) are ultra-sensitive differential vector magnetometers. Low temperature (Low-T_c) SQUIDs have less intrinsic noise than High-T_c SQUIDs. High-T_c SQUIDs also have much more internal low frequency noise ($1/f$ noise) when operated in static fields (such as the geomagnetic field). Therefore, High-T_c SQUIDs are rarely used without magnetically shielding it from the environment. However, High-T_c SQUIDs are less expensive and require liquid-nitrogen to function, as opposed to liquid-helium, making them more appealing especially for long period use. Precise models for shielded SQUID sensitivity exist, but little research has been done to

improve unshielded SQUID sensitivity. Using SQUIDs as geomagnetic magnetometers (geomagnetometers) creates a scientific platform to study unshielded SQUID performance. This allows the possibility to contribute to further developments in SQUID design, electronics and operation for improved sensitivity in unshielded environments.

The universities of Stellenbosch, Avignon and Savoie in France have started a collaborative project together with the South African National Space Agency (SANSA) and the French Laboratoire Souterrain à Bas Bruit (LSBB), to investigate using SQUIDs as ultra-sensitive geomagnetometers. The French laboratory employs Low-T_c SQUIDs in a decommissioned nuclear control bunker, 500 m underground. The geomagnetic field variations are then slightly damped, but the Low-T_c SQUIDs and low noise environment allows for very high resolution measurements in the fT range. SANSA and Stellenbosch University has opted for installing High-T_c SQUIDs at SANSA. The project at SANSA therefore explores a more economically viable and scientifically lucrative option, by using High-T_c SQUIDs unshielded as geomagnetometers, with higher environmental noise than that at LSBB. SANSA also provides a magnetically clean environment conforming to magnetic observatory standards.

1.2 Project Goals

The main objective of the project at SANSA is to develop a geomagnetometer SQUID system (GSS) capable of 1 pT sensitivity. The measurements will be uploaded to a near real-time open data exchange webserver at Stellenbosch University Electrical Engineering department, available for public access at http://geomagnet.ee.sun.ac.za.

The project is in the design and installation phase, where the objective is to achieve system stability. System stability entails employing the SQUIDs in a manner to ensure constant operating conditions for repeatable measurement results. This is done by providing the SQUIDs with a stable operating platform free from disturbances, optimising the data acquisition and determining the best operating parameters for the SQUID electronics. System stability is achieved when all parameters have been determined to allow the system to operate at its full potential.

The project will gradually enter the developmental phase as the design and installation phase nears its end. The objective of the developmental stage is to explore different techniques to further reduce the SQUID's internal noise as well as man-made and environmental noise. This can be done by for example, exploring shielding materials and designs to reduce magnetic fields above frequencies of 10 Hz, exploring new modulation techniques or electronics, or exploring unshielded SQUID circuit design. Ultimately, active shielding may be used to cancel the static magnetic fields and improve sensitivity to achieve the project goal.

The goals of the design and installation phase, in sequential order, were as follows:

1. Design the data acquisition system around the specialized SQUID equipment
2. Design an operating platform for the SQUID equipment
3. Install the GSS and get the SQUIDs operational
4. Time stamp and upload the measurement data to the webserver
5. Determine the optimal operating parameters for system stability

1.3 Thesis Overview

During the design and installation phase of developing a GSS, SQUIDs are exposed to harmful circumstances. SQUIDs are delicate sensors and their quality easily degrades due to handling and cooling from room temperature. In fact, SQUIDs should not be handled at all without proper grounding, as static discharge alone could blow the circuits. This thesis therefore provides information on the design and installation phase which would allow reducing SQUID quality degradation when developing a GSS.

In this thesis, the basic theory, design and installation, analysis of the GSS performance after initial installation and recommended improvements to achieve system stability is described. Chapter 2 provides a comprehensive literature review of the basic knowledge required for this project. In Chapter 3, the initial design and installation decisions of the GSS are described. In Chapter 4 the overall performance of the GSS is analysed and recommendations towards improving system stability are thoroughly investigated. Chapter 5 concludes with a quick summary of the thesis and remarks on the project.

Chapter 2

Literature Review

Initially research is undirected, due to not having the necessary insight to gauge the relevance of the information. Handbooks often assume the reader has basic knowledge of all relevant subjects, which necessitates a more in depth study of the subjects. Subjects are often explained using the same textbook derivations, which does not aid the learning process. This hinders a project's progression when the team members are periodically renewed, having to repeat the task of first attaining the relevant knowledge before the project can commence. Therefore it was decided to provide a diligent literature review, which enables progression of the project by lending insight.

This chapter serves two functions. The first function is to share all of the information that facilitated gaining insight into the various subjects. The relevant theoretical background is explained in a brief yet comprehensive manner, while refraining from using arduous textbook derivations. The second function is to examine published information to support project goals, objectives and design decisions.

2.1 Electromagnetic Fields

There is some ambiguity involving electromagnetic fields (EMFs), due to different applications analysing specific frequency ranges, which requires the adaptation of methodologies and terminology. Suffice it to say this is not a problem when only a single application is studied, but does cause confusion when integrating different subjects. For this reason, this interpretation follows a more holistic approach by explaining the general behaviour of EMFs over the whole frequency spectrum. It should be noted that EMFs do incur all manners of resonance, for example nuclear magnetic resonance or electron spin resonance, which may lead to different behaviour when looking at specific frequency ranges.

2.1.1 Electromagnetic Field Overview

The electromagnetic (EM) force is the most prevalent of the four fundamental forces, which are the building blocks of all known interactions between matter particles. Its interactions are seen all around and used in everyday life, from Coulomb forces between charged particles to lightning. Electrically charged particles, such as electrons, are constantly emitting and absorbing the carriers of the EM force, called photons. An EMF is a measure of the net force that photons deliver to charged particles. According to classical electrodynamics (CED), an electric field is created due to a potential difference in charge exerting a force on stationary charged particles. The electric force accelerates the particles in the direction of the field, measured in units of volt per meter (V/m or N/C). The magnetic field is created due to the movement of charge exerting a force on other moving charged particles. The magnetic force accelerates the particles perpendicular to the direction of its movement and the field, measured in units of Tesla (T or Ns/Cm). A time-varying magnetic field can also create a spatially-varying electric field and vice versa, as described by the Maxwell-Faraday equations.

Electric and magnetic fields were first understood as two separate yet interrelated phenomena before EMFs were quantised and time was discovered to be a dimension. One of Einstein's supporting arguments for his special theory of relativity unified electric and magnetic field theories. By referring to Maxwell's equations it concluded that the distinction between the two fields is due to considering only one inertial frame of reference. For example, a charged particle moving at very high speed relative to the earth's inertial frame of reference encountering a time-varying magnetic field, would encounter a spatially varying electric field relative to its own inertial frame of reference (where the particle is stationary). In this scenario the magnitude and direction of the force exerted on the particle remain the same, but changing the frame results in perceiving another type of field. This shows that the relative motion and distance between the charged particles emitting and absorbing the energy quanta (photons), is what determines the direction and magnitude of the force. Therefore electric and magnetic fields are not two separate yet interrelated fields, but rather a single field having two components dependant on the observers inertial frame of reference. [4]

In quantum electrodynamics (QED) a photon can be described as a packet of energy moving at the speed of light, relative to all inertial frames of reference. Photons are easily confused with something having physical shape, when in fact they are simply the smallest amount of EM energy associated with a single interaction at a specific frequency. A larger EMF has more photons that can interact with more charged particles, while the frequency determines how much energy is transferred in the interactions. This was made evident by the photoelectric effect. With QED, photons' interactions with charged particles can be calculated with probability distributions. CED is used when the EMF is large enough for the sum of the interactions to have macroscopic effects. From a CED perspective, these interactions are better understood with knowledge of the propagation parameters of EMFs, but first it is necessary to understand the constituents of EM energy from a QED point of view.

2.1.2 Real photons and virtual photons

Real photons are massless gauge bosons, propagating linearly through space and time at a constant speed, the speed of light (c), with energy determined by its characteristic frequency, expressed through Planck's Law as,

$$E_p = hf = \frac{hc}{\lambda} \qquad \textbf{(2.1.1)}$$

where E_p (eV) is the energy of the photon, h is Planck's constant, f (Hz) is the frequency of the EMF and λ (m) is the wavelength. Real photons are the constituents of EM radiation (EMR), which is the net amount of EM energy being radiated away from its source, resulting in a definite loss of EM energy in the source. The intensity (power) of EMR decreases with increasing radius from the source with the inverse-square law, as the energy quanta (real photons) disperses. EMR can then be approximated as plane waves due to having known energy and dispersive properties. The electric and magnetic waves of EMR are in phase, perpendicular to each other and the direction of propagation, with a fixed amplitude ratio and a predominant electric field component. This is because the field components are directly coupled to each other without being

affected by potential difference in charge or charge movement. The ratio of the electric to magnetic field amplitude of EMR is the speed of light. Affected

EMFs that are not radiated will return to the source or can interact with other particles within a certain distance. This is seen with electric and magnetic dipoles, induction field coupling and in the near-field of antennas. This EM energy cannot be quantised by following Planck's law, as individual interactions are not observable and there is an uncertainty in energy until it is measured. Therefore, the quanta of this EM energy are called virtual photons. Virtual photons are said to exist when there is a 50% or higher probability that they can interact with other particles. Virtual photons may then only exist as long as they adhere to Heisenberg's uncertainty principle, more specifically the time-energy uncertainty principle. The principle states that the uncertainty in energy (ΔE) multiplied by the time it exists (Δt), must be less than the reduced Planck's constant ($\hbar$):

$$\Delta E \Delta t \ < \ \hbar \tag{2.1.2}$$

For time varying fields, virtual photons can only contribute to interactions within a certain distance due to the time they are allowed to exist. This distance can be calculated by combining Planck's law with the time-energy uncertainty principle:

$$\frac{hc}{\lambda} \Delta t \ < \ \hbar \tag{2.1.3}$$

Knowing the time the virtual photon is allowed to exist is the distance (*D*) it is allowed to travel at the speed of light, Equation (2.1.3) becomes:

$$\frac{hc}{\lambda} \frac{D}{c} \ < \ \hbar \tag{2.1.4}$$

Rearranging Equation (2.1.4) and substituting $h = 2\pi\hbar$:

$$D < \frac{\lambda}{2\pi} \tag{2.1.5}$$

This means that virtual photons are said to exist and interact with other particles within a sixth of their wavelength. From this it is clear that longer wavelength or lower frequency virtual photons may travel much further to interact with other particles. However, the intensity of EMFs consisting of virtual photons decreases exponentially with increasing distance from the source, except for electric and magnetic dipoles in which the field decreases with the inverse square law. The more rapid decrease in intensity makes sense when considering that the field returns to the sources and does not disperse.

For time varying fields, which always has an electric and magnetic field component, closer than a sixth of a wavelength the EMF is predominantly virtual photons. At a sixth of a wavelength the EMF consists of equal amounts of virtual and real photons. At further distances the probability that the photons are being radiated becomes higher. The electric and magnetic fields of virtual photons do not have fixed ratios to one another and are 90˚ out of phase due to being directly coupled to electrically charged particles. At a sixth of a wavelength, the electric and magnetic fields of a time-varying EMF will be 45˚ out of phase due to having equal amounts of virtual and real photons.

2.1.3 EM propagation parameters

The atomic and molecular structure of a medium dictates how the electrically charged particles respond to EMFs. The permeability, permittivity and conductivity are EM properties that describe different aspects of the response, but are also interrelated due to the coupling of electric and magnetic fields. These properties are also temperature and pressure dependant, but only its EMF dependence will be discussed in this section.

Permeability is a measure of the degree to which magnetic dipoles are reorientated or migrated within a medium. Thus it relates to the ease at which a medium is magnetically polarized, expressed as [5]

$$B = \mu_0(H + M) = \mu H \,, \qquad \textbf{(2.1.6)}$$

where B is the magnetic flux density or magnetic field (T or Vs/m^2) in the medium, μ_0 is the permeability of free space ($4\pi10^{-7}$ H/m or Ωs/m), H is the auxiliary magnetic field or magnetic field strength (A/m) and M is the magnetic polarization of the medium. It can be seen that the magnetic field induced within the medium differs from the field which would be encountered in free space ($\mu_0 H$), because the material becomes polarized. Dipoles can either be reorientated to conduct (positive polarization) or oppose (negative polarization) the applied field. Polarization has a linear response to the applied field, except in a high permeability medium (ferromagnetic) where dipoles are migrated, leading to hysteresis due to residual fields after the applied field is removed.

Polarization of high permeability material has a linear response at very small applied fields, resulting in a constant permeability, called the initial permeability. As the applied field increases, polarization increases exponentially until there are no more magnetic dipoles available to migrate, at which point the permeability of the medium reaches a maximum. Thereafter, further increasing the applied field will not lead to larger polarization, resulting in a decreasing permeability as the medium reaches its saturation induction.

At higher frequencies (relative to a medium) magnetic dipoles cannot be reorientated or migrated fast enough, causing a phase delay between the applied magnetic field and magnetic polarization, which results in a decrease in permeability. If the energy surpasses the binding energy, electrons are freed from their orbitals, in which case they cannot conduct the magnetic field at all. Permeability therefore strives to μ_0 at higher frequencies. [5, 6, 7]

Permittivity relates to the amount of electric dipoles that can be reorientated or the charge that can migrate or shift within a medium, thus it relates to electric polarization. This means it is a measure of the degree to which an electric field can be conducted or "stored" within a medium, expressed as [8]

$$D = \epsilon_0 E + P = \epsilon E \ , \tag{2.1.7}$$

where D is the displacement field (C/m^2), ϵ_0 is the permittivity of free space (8.854×10^{-12} F/m or s/Ωm), E is the electric field (V/m) and P is the electric polarization density. Comparing Equations (2.1.6) and (2.1.7), it can be seen that permeability for magnetic fields is analogous to the inverse of permittivity for electric fields. Permittivity does not lead to inducing an electric field larger than the incident electric field. The electric field created by the electric dipole reorientation and charge migration always opposes the incident electric field. The displacement field is not an actual measurable field within the material, but rather the effect that an electric field has on the charge density. The divergence of D gives the free charge density. Materials with high permittivity are easily polarized, allowing electric fields to propagate with a low loss in energy. Permittivity varies with a range of parameters, including the magnitude (except in dielectric materials) and frequency of the electric field. Higher frequency EMFs also leads to electric polarization having a phase delay, causing the permittivity to strive to ϵ_0 as the electric field frequency increases. [8, 9]

Conductivity (S/m or 1/Ωm) is a measure of the mobility of electrical charge within a material. This means that conductivity is the ability of an electric field to induce a current flow of free charges, expressed as

$$\sigma = \frac{J_f}{E} \ , \tag{2.1.8}$$

where J_f is the conduction current density (A/m^2), which is the product of the free charge density and mean drift velocity. Conductivity increases with increasing frequency as the electric field lends more kinetic energy to free electrons, increasing the mean drift

velocity. Of course in conductors the valence band and conduction band overlap and many more free electrons are available at much lower frequencies. If the valence electrons receive enough energy to enter the conduction band, it results in a smaller permittivity and larger conductivity. With increasing frequency, the conductivity however starts to reach a maximum as the frequency approaches the energy gap between lower electron bands, increasing lattice vibrations and hence resistance. Increasing the frequency further, would result in electrons hopping to higher electron bands or photoelectrons escaping from the material if the work energy is surpassed. An increase in electric field intensity leads to more photons that can interact with electrons, which can increase either the mean drift velocity or free charge density depending on the frequency. Increasing the electric field intensity further after the maximum J_f has been reached results in a decrease in conductivity, due to the increased free charge density resulting in more electron scattering.

2.1.4 Near-field and Far-field

Even though photons move at the speed of light, EMFs do not necessarily propagate at the speed of light. Photons of EMFs propagating through a medium are continuously being absorbed and reemitted or transformed into other forms of energy. Being the first to describe EMFs as propagating waves, Maxwell discovered that EM waves propagate at the speed of light in free space, concluding that light was also EMR. The propagation velocity or phase-velocity v (m/s) of an EM wave in any medium is given by [6]:

$$v = \left(\frac{\mu\epsilon}{2} \left[\sqrt{1 + \left(\frac{\sigma}{\omega\epsilon} \right)^2} + 1 \right] \right)^{-1/2} \qquad \textbf{(2.1.9)}$$

where ω (rad/s) is the radial frequency. $\frac{\sigma}{\omega\epsilon}$ is known as the loss tangent, which compensates for absorption by free charge, leading to attenuation of the EM wave. As frequency increases, the loss tangent will only become negligible at much larger frequencies than normally encountered, as the conductivity increases to a maximum value and the permittivity decreases.

However, it is still evident that as the frequency increases, the propagation velocity will eventually strive to the speed of light as the propagation parameters strives towards that of free space:

$$c = \frac{1}{\sqrt{\mu_0 \epsilon_0}} \tag{2.1.10}$$

It also makes sense that higher frequencies will propagate faster when considering that charged particles absorb energy on the basis of using all or nothing. This means that lower frequencies are absorbed and reemitted, while higher frequency photons are more likely to be transformed into kinetic or other forms of energy when absorbed. Higher frequency EMFs are therefore attenuated more, while lower frequencies are absorbed and reemitted more, contributing to a larger decrease in propagation velocity.

When EMFs encounter a boundary between different media, the waves are reflected and refracted to compensate for the change in speed or wavelength. A wave will be refracted closer to the norm when decreasing in speed and closer to the boundary surface when increasing in speed (conductor to air), expressed as

$$\frac{\sin\theta_1}{v_1} = \frac{\sin\theta_2}{v_2}. \tag{2.1.11}$$

In Equation (2.1.11), subscripts 1 and 2 denote the incident and refracted wave and θ the angle of propagation relative to the norm of the boundary surface. In optics the different refraction angles due to the frequency dependence of the propagation velocity is called dispersion. Within the visible spectrum, most transparent material have normal dispersion, where higher frequencies are refracted more, while some have anomalous dispersion where higher frequencies are refracted less (the refraction angle will be closer to the incident angle). Considering the whole of the frequency spectrum, higher frequencies propagate faster than lower frequencies within a medium, requiring less refraction to compensate for the change in velocity when transitioning to free space. Anomalous dispersion will therefore be the general behaviour of EMFs.

The critical angle θ_c is known as the incident angle at which refraction reaches 90°. All of an EMF transmitted from conductor to air incident below the critical angle is refracted (with some reflection) to radiate the full 180°, and becomes EMR (real photons in QED). Total internal reflection occurs where the incident angle is larger than the critical angle. However, it is not possible for an EMF or any particle to abruptly change direction, as explained by Schrödinger's wave-function. This means that internally reflected EMFs do propagate a distance outside the source, but eventually find their way back (virtual photons in QED). These fields are then called evanescent fields, due to returning to the source and decreasing in intensity more rapidly away from the source.

Higher frequency EMFs generally have larger critical angles, due to being refracted less when transmitted from conductor to air. Therefore, higher frequency EMFs have less internal reflection and smaller evanescent fields. As previously explained through QED, higher frequency virtual photons have shorter distances in which they can exist.

Figure 1 is a visual representation of EMFs propagating from a conductor to air. The placement of the frequency sources within the conductor was done for illustration convenience, only the propagation of the field is relevant. Note that internal reflection is omitted and scaling is not accurate. The four frequency sources start emitting EMFs at different times to allow all the first field lines to reach the boundary simultaneously, as seen by the EMR having travelled the same distance. This illustration shows how lower frequency EMFs have slower propagation speeds within the conductor, smaller critical angles (straight purple lines) and larger evanescent fields (small, red curved lines). Lower frequencies also have a larger change in wavelength when transmitted to the air, due to the larger change in propagation velocity. EMFs transmitted from a source are therefore divided into two zones. The near-field zone is where the waves have a relatively high probability of returning to the source, and the far-field zone where the waves are indefinitely being radiated from the source.

The near-field refers to the region wherein the evanescent field is larger or comparable in magnitude to the EMR, which is closer than half a wavelength from the source. Closer than a sixth of a wavelength distance from the source, evanescent fields dominate the EMF. The electric and magnetic field of the evanescent field does not have a fixed ratio

to one another, because the fields are affected by potential difference in charge and charge movement, which is frequency dependant. The same amount of energy that flows out, resulting in a positive Poynting vector ($\vec{S} = \vec{E} \times \vec{B}$), will flow into the source again, resulting in a negative Poynting vector ($-\vec{S} = \vec{E} \times -\vec{B}$). This results in phase quadrature, which means half the time the electric and magnetic field components will have opposite signs, which is indicative of a 90° phase shift [10]. As the evanescent field decreases and EMR becomes comparable in magnitude, the phase shift decreases. At a sixth of a wavelength distance (where real and virtual photons have equal probability of existing), evanescent fields and EMR have equal magnitudes, which means the electric and magnetic fields will be 45° out of phase.

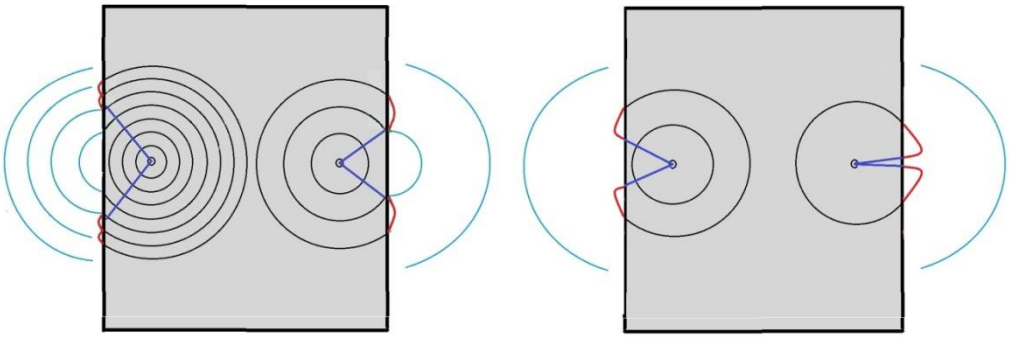

Figure 1: Different frequencies EMF propagation and evanescent fields. Blue lines are EMR, purple lines are the critical angles and red lines are evanescent fields.

2.2 Geomagnetic Field Spectrum

The geomagnetic field is generated by the low viscosity flow of molten iron in the earth's outer core, referred to as the geodynamo. The geodynamo is affected by the earth's rotation and geometry, which only causes secular variations (seen in Figure 2). Shorter period variations are absorbed in the mantle and crust. Variations in the geomagnetic field within a period of 4 months ($> 10^{-7}$ Hz) can be ascribed to sources outside of the geodynamo. Therefore the geodynamo is modelled as a dipole tilted 11.5˚ from the rotation axis or as a combination of dipoles for accuracy better than 90%, with the magnitude ranging from 23 µT to 67 µT at the Earth's surface. [11]

The amplitude spectral density of the geomagnetic field above 0.1 Hz is usually smaller than 0.1 nT/$\sqrt{\text{Hz}}$. This is why geomagnetic observatory magnetometer measurements with 0.1 nT resolution are only required to have 1 Hz sample rates, with a low-pass cut-off frequency at 0.1 Hz. Between 1 Hz and 100 Hz, the geomagnetic field amplitude spectral density has a noise floor around 1 pT/$\sqrt{\text{Hz}}$. The noise floor is caused by man-made sources and Schumann resonances. [11, 12]

Schumann resonances, discovered by Winfried Otto Schumann, are caused by EM waves from lightning, resonating in the space between the highly conducting ionosphere and earth, which acts as a waveguide. Schumann approximated the fundamental frequency by dividing the speed of light by the circumference of the Earth. Taking spherical geometry and damping due to finite conductivity in the ionosphere into account, the resonant frequencies can be approximated by [13]

$$f_n \approx 6\sqrt{n(n+1)}\ , \qquad \textbf{(2.2.1)}$$

where $n = 1, 2, 3 \ldots$ represents the harmonics. Figure 3 shows the typical spectrum of the first 7 Schumann resonances, measured at Silberborn in the Solling Mountains Germany. The German railroad and powerline signals are also seen in this spectrum, with a 0.5 pT/$\sqrt{\text{Hz}}$ noise floor.

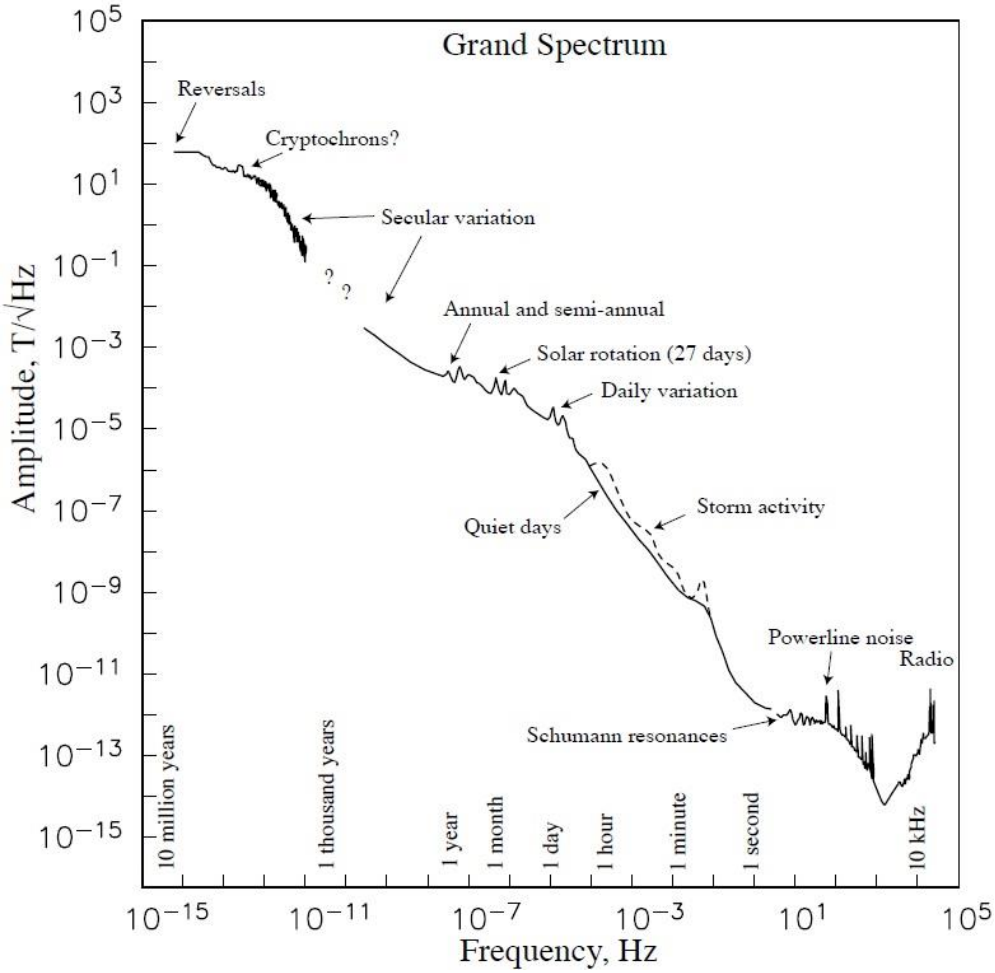

Figure 2: Geomagnetic field spectrum. [11]

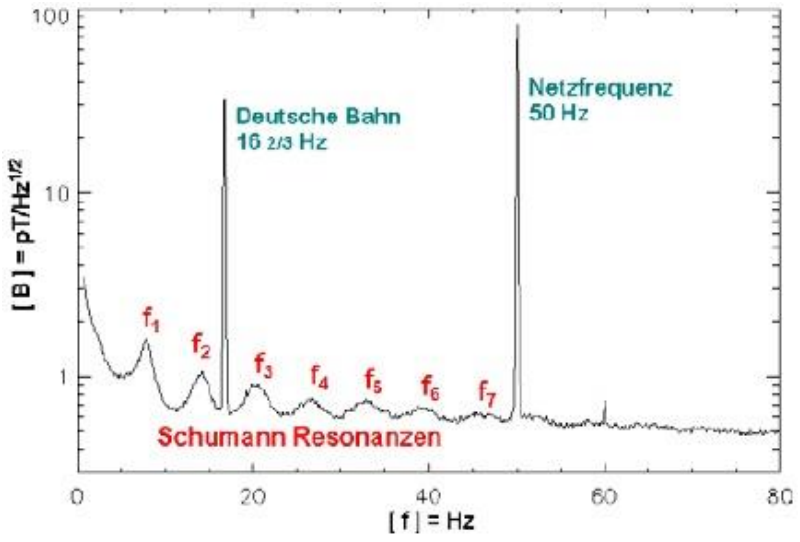

Figure 3: Schumann resonances spectrum at Silberborn. [13]

2.3 Superconductivity and SQUIDs

To understand normal electrical components, knowledge of classical electrodynamics is required. Here electrons move independently from one another and only the net behaviour of all electrons (e.g. current flow) is considered and described with macroscopic equations. For superconductors the picture changes considerably. Here the behaviour of every electron is dependent on the behaviour of the whole system. Superconductivity is described as quantum effects on a macroscopic scale, which requires knowledge of quantum electrodynamics.

This section provides a short description of superconductivity and how SQUIDs use quantum interference to measure minute changes in magnetic fields. This will lead to an understanding of problems encountered when using SQUID magnetometers and how measurements could be improved when using a specific SQUID. The theory is explained as it pertains to engineering or applied superconductivity.

2.3.1 Superconductivity

For different metals, alloys and metal oxide ceramics, there exists a critical temperature (T_c), at which the material starts to allow a limited current density (up to the critical current density J_c) to flow without encountering resistance. The more the temperature is lowered beneath T_c, the larger J_c becomes. This phase is called superconduction.

For low-temperature superconductors (LTS), T_c is lower than 24K. For special metal oxide ceramics or high-temperature superconductors (HTS), T_c is higher than 24K, with a maximum T_c of 165K achieved thus far for HgBaCaCuO at a pressure greater than 25GPa. Only certain parts of the specialised crystal lattice of HTS react suitably for superconductivity to take place at their higher T_c. HTS therefore consist of a mixture of normal and superconducting material when cooled below T_c.

2.3.1.1 Current flow

Coulomb forces between charged particles allow electrons to only exist in specific energy bands or quantum states, with specific band widths. No electrons exist in the gaps between the energy bands. The terms “band gap” or “energy gap” generally refer to the minimum energy required to cause valence electrons to hop from the top limit of the valence band to the bottom limit of the conduction band. Insulators have very large band gaps. Semiconductors have smaller band gaps. Conductors have very small or no band gaps, which cause valence electrons to easily move freely. The Fermi level is not an actual energy level, but would hypothetically lie within the band gap. The Fermi level describes the work required to add an electron to the material and has a 50% chance of being occupied if electrons could exist at that state (see Figure 4).

An increase in temperature decreases the band gap. If the temperature of a semiconductor is increased, the valence band and the conduction band will eventually overlap and the band gap will effectively disappear. Insulators will generally melt before the band gap disappears. In conductors, an increase in temperature leads to more free electrons and more severe vibrations in the crystal lattice, as a result of Coulomb forces and the interchange of a large amount of phonons (quanta of heat and sound).

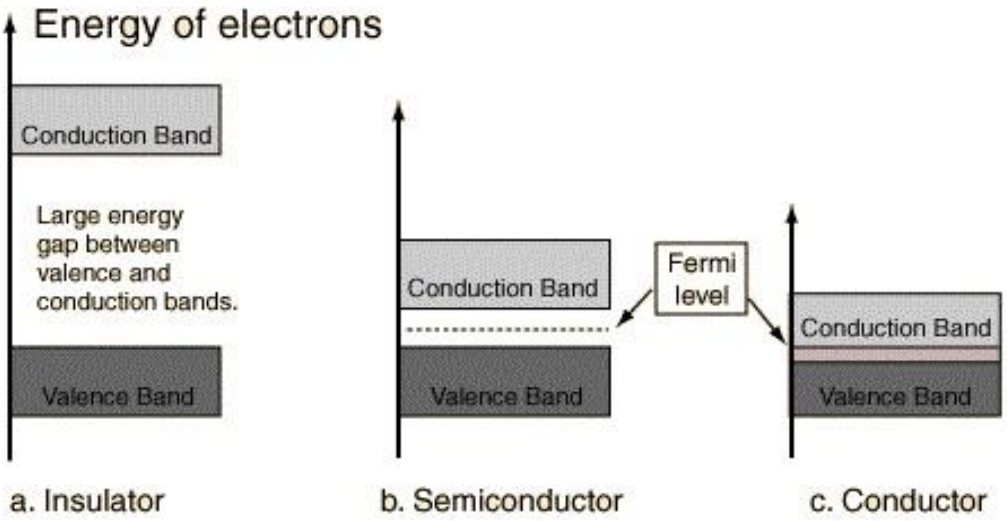

Figure 4: Band gaps of different materials.

In conductors, current flow occurs when an applied electric field is large enough to accelerate free electrons in a general direction. More free electrons and vibrations cause free electrons to scatter more or randomly diffuse throughout the crystal lattice. This behaviour causes electrical resistance. The fact that more free electrons lead to greater resistance sound counterintuitive, but makes sense when it is taken into account that electric current flows in the same energy level as the scattered free electrons. A more brief explanation is that stronger electron-phonon interactions lead to more diffusion through thermal vibrations, which causes a weaker conductivity [14]. Therefore, higher temperatures lead to greater resistance in conductors, but better conduction in semiconductors.

At lower temperatures, the valence electrons have less energy, which causes them to move closer to their nucleus and leads to a wider band gap and lower Fermi level. When material becomes superconductive below T_c, the condensed (increase in density) valence electrons now allow more free electrons to incur an interaction which is not normally perceptible due to scattering. This interaction is called Cooper pairing, where two electrons with opposite spin pair up. In 1957, Bardeen, Cooper and Schrieffer developed the BCS theory, explaining the origin of Cooper pairs in terms of electron-phonon interactions alone. The BCS theory is far from perfect and applies more to LTS, while HTS must take into account far more and greater interactions to explain how Cooper pairs originate (see Figure 5). The BCS theory nevertheless led to the discovery of certain behaviour of Cooper pairs, which serves as a sound basis for the understanding of superconductivity. For engineers the empirical behaviour of Cooper pairs is more important than the theory regarding interactions that lead to their existence. Therefore, only the empirical behaviour of Cooper pairs will be taken into account further.

Cooper pairs have double the electric component of a single electron. The magnetic moments of Cooper pairs are reduced as a result of the opposite spin moment of the paired electrons. As a result of their altered Coulomb forces, the Cooper pairs exist under the Fermi energy, the lowest Fermi level possible at absolute zero temperature (0 K). Normal free electrons have more energy and only exist at a higher energy level, in the conduction band. An important concept in superconductivity is that this energy gap

(2Δ) arises between Cooper pairs and normal free electrons. The energy gap is very small, but must nevertheless first be bridged before the Cooper pairing mechanism can be negated. The Cooper pairs can therefore move in an energy level below that of normal free electrons, without scattering, if the energy is kept low enough. Closer to T_c the energy gap will become smaller and fewer Cooper pairs will be capable of forming (see Figure 5). [14]

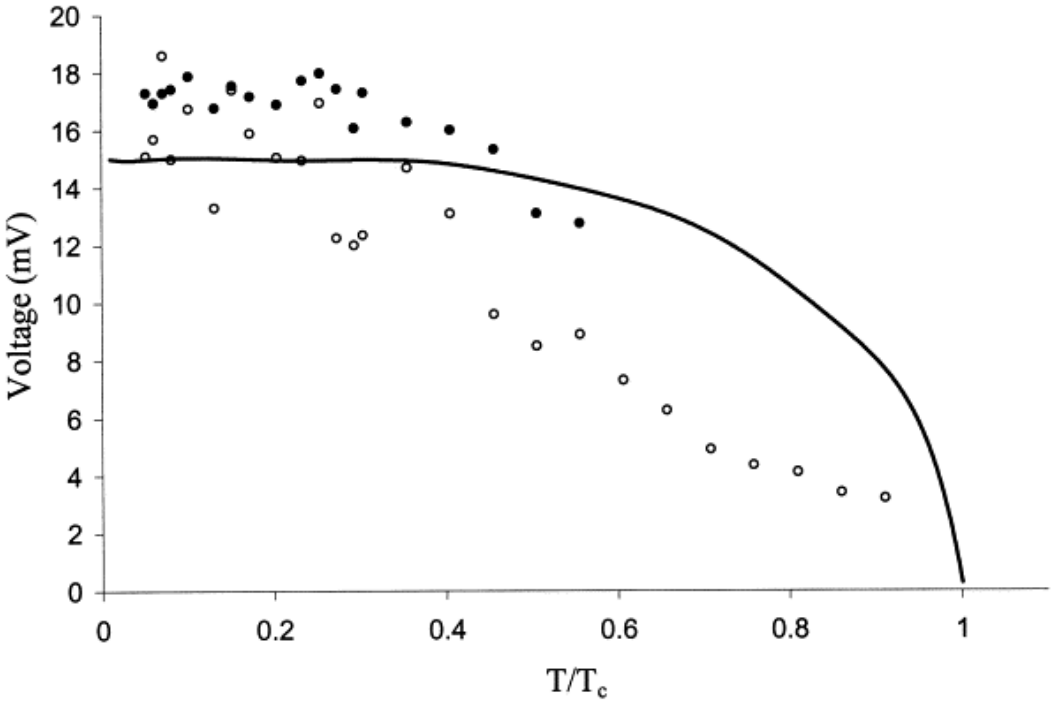

Figure 5: Energy gap 2Δ(T)/2 in mV against normalised temperature T/T_c. The solid line is the expected energy gap according to the BCS theory and the dots are the measured values for a HTS with T_c of 108K. [15]

Another important concept in superconductivity is that the freed electrons that are below the Fermi energy have a large coherence length. In other words, the difference in frequency (energy) of the electrons' wave functions is so small that a phase difference will only be perceptible after they have travelled a great distance. Higher energy levels lead to more scattering, which means shorter coherence lengths or greater phase

differences between wave functions over shorter distances or times. The coherence length of electrons below the Fermi energy is in the order of nano- to micrometres, while the distance between ions in the crystal lattice is typically in the order of hundred picometres. Therefore, there are many valence electrons within each other's coherence lengths, which can be used to form Cooper pairs. A Cooper pair is therefore not two specific electrons that remain paired, on the contrary the electrons exchange constantly between different Cooper pairs. Throughout the superconductor there will be great constant overlapping of electron coherence lengths. This overlapping causes the Cooper pair wave functions to remain coherent (in phase) over enormous distances. In short, all Cooper pairs in a superconductor have the same wave function, while normal free electrons have different wave functions. [14]

Less energy is required to create a current flow with electrons that incur less scattering (current follows the route with the least resistance). In superconductors, electrons can flow in a supercurrent of Cooper pairs in an energy level below the conduction band, short circuiting normal current. The supercurrent travels with a coherent wave function in the surface layer of the material. Therefore, there is no electric potential difference when supercurrent flows, because all the electrons are uniformly dispersed and the Cooper pairs travel in the same way and direction without scattering. Any current in excess of the critical current (I_c) will flow as normal current. More normal current will have more scattering, causing the material to build up an electrical potential which eventually forces it out of superconductivity when it bridges the energy gap. Alternating current gives more energy and will bridge the energy gap more easily. [14]

2.3.1.2 Magnetic behaviour

Diamagnetism is a very weak force, which occurs in all materials. It is the result of electrons temporarily changing their orbital velocity and orientation to balance Coulomb forces by opposing external magnetic fields. Diamagnetism is more prominent in atoms with more electrons and is mostly the predominant magnetic behaviour of atoms with more valence electrons. Free electrons in conductors also oppose changes in the external magnetic fields by generating eddy currents.

Superconductors display behaviour similar to ideal diamagnetism and eddy currents, which is called the Meissner-Ochsenfeld effect. Unlike ideal diamagnetism, the Meissner effect entails that all internal magnetic fields are completely forced out of the superconductor, except for a small surface layer known as the "London penetration depth" (λ_L). The Cooper pairs move to the surface, where it creates a shielding current that, unlike eddy currents, opposes all external fields, allowing the internal electrons to remain in their lower energy states. The amount of energy it can force out is equal to the energy gap. In Type 1 superconductors (which most LTS are), the magnetic field within the material will approach zero as it is cooled further below T_c. Larger external magnetic fields lead to more shielding current, leaving fewer Cooper pairs available to conduct supercurrent, decreasing I_c (see Figure 6). If the external field exceeds the critical magnetic field (H_c), all Cooper pairs will be spent on providing shielding current, allowing the excess magnetic energy to penetrate the superconductor, forcing it out of superconductivity. If the external magnetic field decreases over a LTS, the electrons will rearrange themselves to exist in the lowest energy level possible.

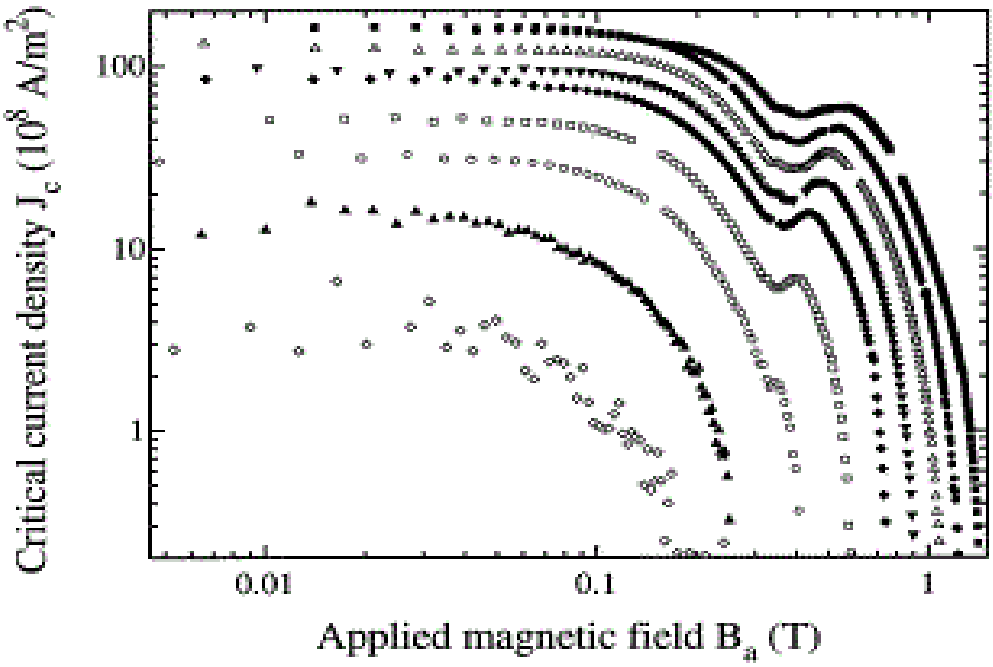

Figure 6: Critical current density (J_c) dependence on external magnetic field applied over a thin film of Nb, from temperatures 4.5K (top curve) to 8.5K (bottom curve). [16]

Changes in the magnetic field over a superconducting ring (loop) will induce a circulating supercurrent which opposes the change in flux quanta through the ring. Unlike electromagnetic induction in normal conductors, the rate of change is irrelevant towards the magnitude of the induced supercurrent, because supercurrent does not incur resistance and is induced in quantised amounts. Unless the magnetic field reverts to its original magnitude, the current will flow persistently, because there is no resistance which leads to its decay. The magnetic flux threading the ring cannot change as a result of the magnetic fields generated by the circulating supercurrent. The flux threading the loop as the material enters the superconducting phase therefore becomes trapped. This is known as flux trapping or flux freezing. The supercurrent wave function makes one complete phase oscillation for each trapped flux quantum (see Figure 7). A magnetic flux quantum has the value:

$$\Phi_0 = \frac{h}{2e} = 2.07 \times 10^{-15} \quad \text{(Wb)} \qquad \textbf{(2.3.1)}$$

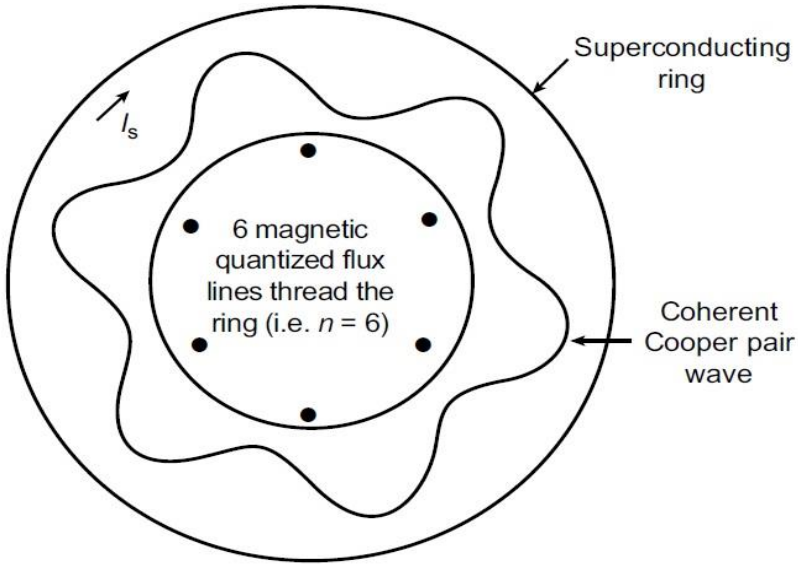

Figure 7: Magnetic flux quantisation in 'n superconducting ring. I_s is the circulating supercurrent, moving with a coherent wave function. [14]

The correlation between the phase change around the superconducting ring and the amount of flux quanta is what helped establish the large coherence lengths of Cooper pairs. The Cooper pair wave function would not be coherent if it did not have integer amounts of oscillations around the ring. This is why superconductivity is considered to have quantum effects on a macroscopic scale. [14]

It is however possible for flux quanta to slip in and out of a thin superconducting ring. The energy the ring can contain is proportional to its thickness, in that the flux is more securely confined (or pinned) within a longer cylinder. A flux slip results in a 2π phase increase or reduction in the wave function around the ring, hence it is also referred to as a phase slip. Flux slips also incur a transient increase in entropy and electrical potential in the superconductor. Flux slips are avoided in normal superconducting circuits, however it can also be utilised in coherent quantum phase-slip (CQPS) qubits as an alternative to Josephson Junctions. Some texts refer to flux slips as flux jumps or phase jumps. In this thesis, distinction will be made and flux jumps will refer to an error that occurs with SQUID modulation electronics (Section 2.3.3.2), which does not incur a change in flux threading the ring.

HTS consist of superconductive and normal material, which leads to magnetic flux being trapped within the normal material. As HTS becomes superconductive, the normal material will not display the Meissner effect. The superconductive material will circulate shielding current around the normal material as it attempts to force out the field. The magnetic field is then, to a certain degree, trapped within the normal material in quantised flux tubes. The shielding current trapped inside the superconductor is then known as an Abrikosov vortex. HTS is therefore classified as a type-2 superconductor, with an upper critical magnetic field (H_{c2}) and a lower critical magnetic field (H_{c1}). Above H_{c2} the material will be in the normal phase and will lose its superconductivity as more magnetic fields penetrate the superconductive material. If kept below H_{c1} the material will only display the Meissner phase, with no vortices or flux tubes present. At magnetic fields between the two critical fields, the superconductor exists in the Shubnikov phase, a mixture of the normal and Meissner phases. At larger fields within the Shubnikov phase, the field is quantised into more flux tubes (see Figure 8), which leads to larger magnetic fields in the superconductive material and a decrease in I_c.

Unlike LTS, flux trapping within the normal material of HTS, prevents it from returning to superconductivity after the field is decreased below H_{c2}. HTS therefore have a much larger upper critical field than LTS, because vortices allow some flux to move through the flux tubes without being opposed by shielding current.

When current flows through HTS and the Lorentz forces are greater than the pinning forces of vortices, it results in flux slipping of flux tubes. The flux tubes then migrate from pinning sites, which results in an electric potential difference in the material. Different defects in the superconductor can cause different types of vortices. Defects include normal material, grain boundaries, disruptions, difference in material characteristics, etc. The Kibble-Zurek theory explains that faster phase transition to superconductivity (faster rate of cooling) creates more defects and can trap flux even in zero fields, as seen in Figure 8. [17, 18]

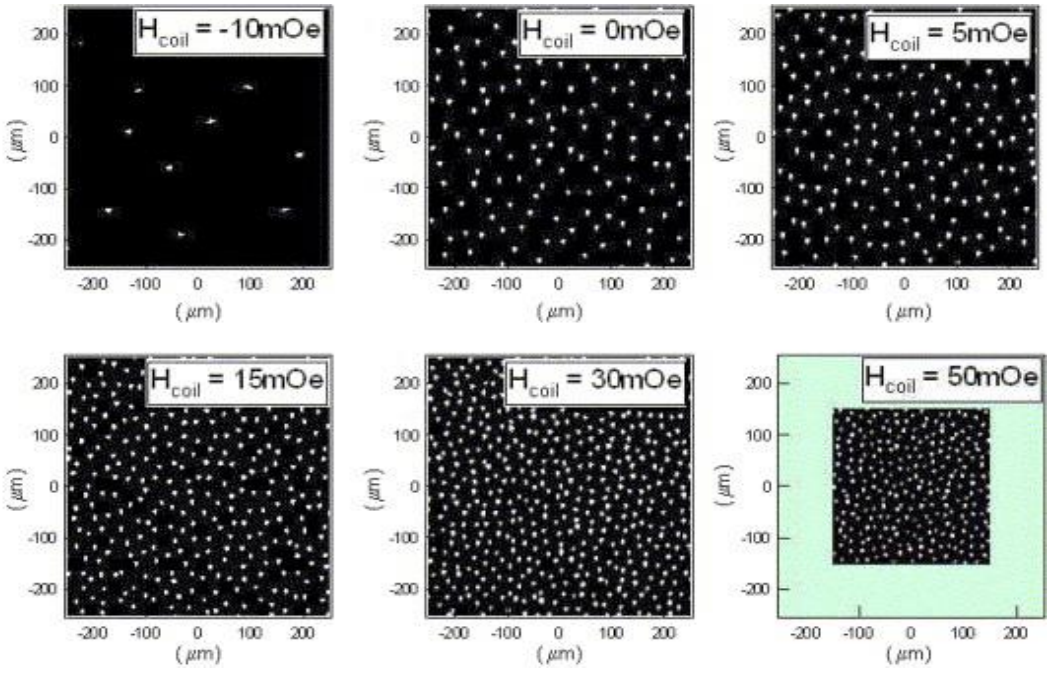

Figure 8: Vortex trapping in YBCO (HTS) film with different applied external magnetic fields. YBCO film is cooled down to 2K. 1mOe = 0.1μT [19]

2.3.2 Quantum Interference

Quantum interference is a sudden (without intermediate conditions) change in the wave function of coherent particles, without aid from external forces. It is not fully understood as to why it happens, but when particles with a coherent wave function encounter a barrier, they suddenly assume a new phase after moving through it. The amplitude and phase of the wave function are interdependent. In superconductors, quantum interference occurs when Cooper pairs tunnel through a Josephson Junction (JJ), situated within a superconducting loop. A SQUID makes use of the interdependence of amplitude and phase to convert magnetic flux into voltage oscillations.

2.3.2.1 Josephson Junctions

Tunnelling is a quantum mechanical process that is described with probability distributions. It occurs because electrons cannot abruptly change direction when they encounter a barrier or obstruction and therefore move a few nanometres outside the conductive material, as described by Schrodinger's wave function. Electrons follow the route that requires the least energy and in the case of a very thin barrier, probability dictates that a number of electrons will move all the way through the barrier (tunnel). It is also possible for Cooper pairs to tunnel in their low energy level.

A JJ is an insulator barrier in a superconductive film, thin enough for Cooper pairs to be capable of tunnelling. The amount of supercurrent that can tunnel will be dependent on the phase difference between the supercurrent on opposite sides of the JJ and can be described with the DC-Josephson equation (first Josephson equation) [20]:

$$I_J = I_c \sin(\theta_1 - \theta_2) = I_c \sin \delta \qquad \textbf{(2.3.2)}$$

Here I_J is the Josephson current (supercurrent) tunnelling through the JJ, θ_1 and θ_2 are the phases of the supercurrent on opposite sides of the JJ and δ is the phase difference. The phase difference is therefore dependent on the amount of supercurrent tunnelling through the JJ and vice versa. This is known as the DC-Josephson effect.

If the applied current is greater than I_c, normal current will flow and generate a voltage, while the amount of Josephson current is dependent on δ. The normal current flowing through the JJ is then calculated as:

$$i = I_{TOT} - I_J \tag{2.3.3}$$

Here I_{TOT} is the total current supplied to the JJ. The normal current (i) will therefore change in amplitude if δ changes. This effect is utilised by DC-SQUIDs. [20]

When a voltage (V) arises across a JJ, Cooper pairs will vibrate through the JJ at a very high and precise frequency, known as the Josephson frequency:

$$f_J = \frac{V}{\Phi_0} = V \times 483.6 \times 10^{12}\ \text{Hz} \tag{2.3.4}$$

The phase difference across the barrier now changes with time at the rate of the Josephson frequency, known as the second Josephson equation:

$$\frac{d\delta}{dt} = 2\pi f_J \tag{2.3.5}$$

The Josephson current then changes over time as follows:

$$I_J = I_c \sin\left(\frac{d\delta}{dt}t\right) \tag{2.3.6}$$

This is known as the AC-Josephson effect. The AC-Josephson effect can be utilised by high-precision oscillators, as a voltage standard and in RF-SQUIDs, which are actually incorrectly named, because quantum interference is not the basis of operation. A JJ will be designed with normal resistance, inductance and capacitance, to reduce hysteresis and to utilize only high or low-frequency current flow. AC-Josephson effects are virtually imperceptible when the JJ is designed to utilise the DC-Josephson effect. [21]

2.3.2.2 I_c Deterioration in Josephson Junctions

Magnetic fields regard JJs as large defects, where it can penetrate the superconductor. When multiples of flux quanta penetrate the JJ parallel to current flow, no supercurrent is capable of tunnelling (Figure 9). The surface area of a JJ determines the magnitude of the magnetic field needed to trap a magnetic flux quantum. JJ dimensions are therefore purposely designed extremely small, so that far greater magnetic fields are necessary before magnetic flux causes a reduction in I_c. However, smaller dimensions reduce I_c, which necessitates optimising dimensions for the magnitude of the external field. Dantsker et al. [22] found that bicrystal YBCO junction widths of 2 µm did not result in measurable reduction of I_c when cooled in static fields up to 60 µT. [21]

Gordeeva [18] shows that, apart from large magnetic fields penetrating the JJ, other vortices form as a result of dimensions which concentrate magnetic flux. The results of the experiment are shown in Figure 10. A cycle entails the heating of the JJ to above T_c and then cooling in a magnetic field. During the first 50 cycles the magnetic field is zero, thereafter it increases by 0.5 µT every 50 cycles. The experiment is carried out on a long JJ, with a surface area of 400 µm^2 (far larger than JJs formed through grain boundaries), where approximately 6.75 µT is equivalent to a magnetic flux quantum through the JJ. As seen in Figure 10, I_c decreases at a faster rate than the ideal Fraunhofer pattern suggests, with quantised steps in I_c as more flux quanta are trapped in other defects.

Gordeeva then applies the Kibble-Zurek theory to JJs. Faster cooling rates also lead to more dramatic quantised decreases in I_c, as a result of the increased amount of defects. Kibble-Zurek experiments are conducted on LTS JJs to eliminate defects such as normal material inclusions in HTS. The LTS JJ is heated above T_c by only a few Kelvin, after which the cooling rate is controlled by pulsing a laser. The probability that vortices are trapped decreases exponentially as the transition time to superconductivity increases and becomes negligible with transition times longer than a few hundred milliseconds. HTS will quite possibly need longer transition times before the probability of forming extra defects will be negligible.

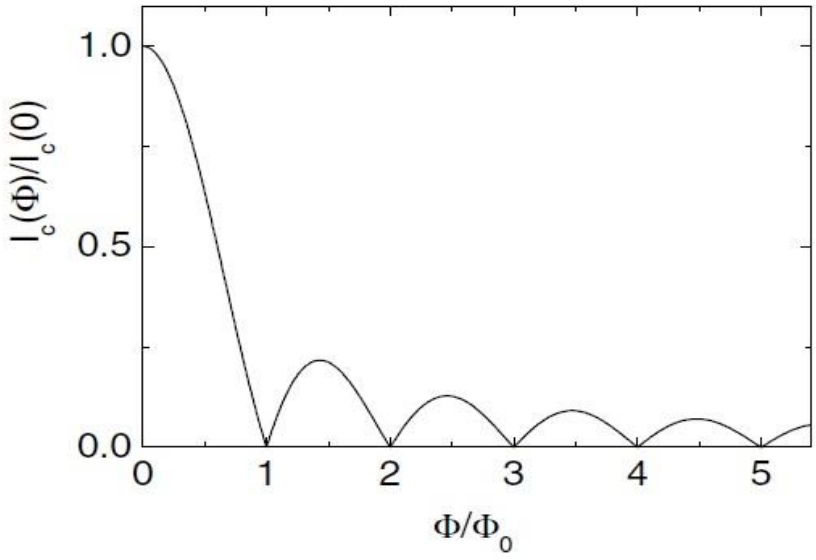

Figure 9: Fraunhofer pattern, showing the dependence of I_c on magnetic flux penetrating a JJ. [20]

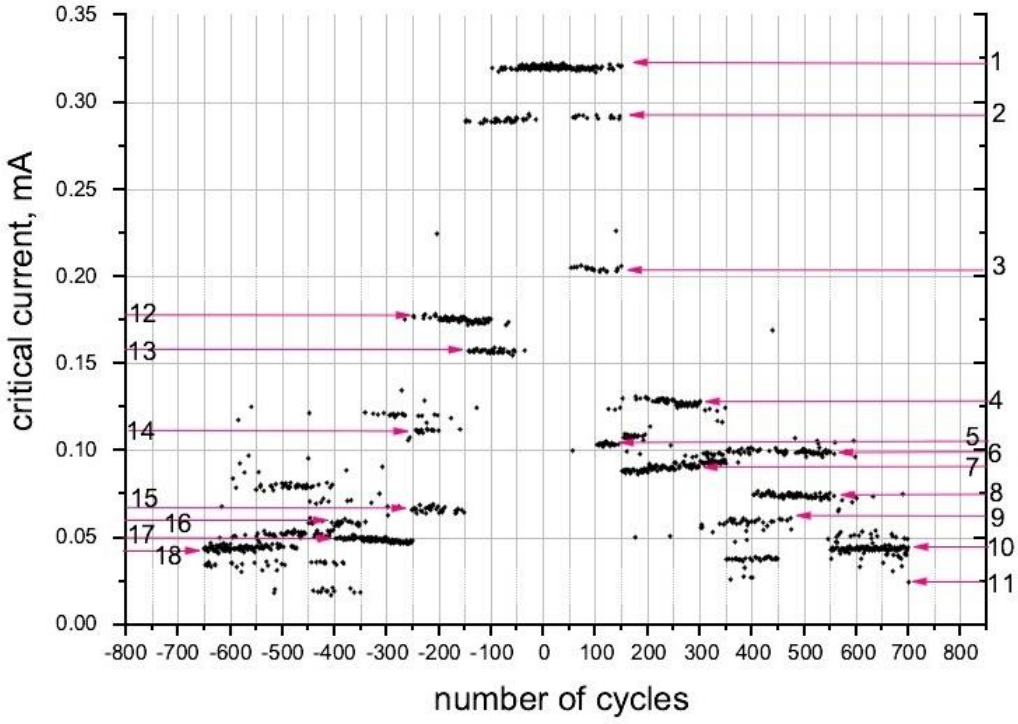

Figure 10: Dependence of I_c on magnetic fields perpendicular to a long LTS JJ. External magnetic field is enlarged by 0.5µT after every 50 cycles. 6.75µT $\approx 1\Phi_0$. [18]

2.3.3 SQUIDs

In this section, only DC-SQUIDs (further referred to only as SQUIDs) will be considered, because they can achieve better sensitivity and are used more regularly. A SQUID is a vector magnetometer that converts magnetic flux into voltage oscillations. LTS SQUIDs can reach sensitivities of 3 fT/$\sqrt{\text{Hz}}$ at 10 Hz in a shielded environment, while HTS SQUIDs will not easily reach lower than 50 fT/$\sqrt{\text{Hz}}$ as a result of vortices and higher temperatures.

A SQUID is a superconductive ring, with two JJs in parallel. The induced circulating supercurrent however, is not the principle of operation. In fact, SQUIDs operate on the basis of control electronics opposing the change in magnetic fields and hence, not allowing quantised amounts of circulating supercurrents to be induced. The basis of operation of SQUIDs are magnetic fields modulating the phase differences (δ) across the JJs with a period of $1\Phi_0$, which in turn determines how much supercurrent flows through the parallel JJs. The SQUID is supplied with a fixed amount of current, but the phase differences across the JJs determines how much of that current will flow as supercurrent and the direction in which the supercurrent may flow. The normal current flowing through the JJs then generates an oscillating voltage with a period of $1\Phi_0$. The electronics then measure the amount of current that is sent through a feedback coil to oppose the magnetic field and prevent the SQUID voltage from oscillating or changing phase. The amplitude of the oscillating SQUID modulation voltage ($V(\Phi_a)$) is called the modulation depth (V_{pp}) and the slope is called the transfer function ($\partial V/\partial\Phi$).

A larger ring area allows smaller fields to induce a change in flux quanta, however this also increases the inductance, allowing more noise from normal circulating currents in the SQUID loop. Sensitivity is therefore compromised when operating a SQUID in larger fields. For this reason, the SQUID loop is purposely designed with very small dimensions, to minimise the inductance. The SQUID loop is then attached to a larger pick-up loop, which is much more sensitive to magnetic field changes. Being connected to the pick-up loop, the same phase changes in supercurrent will be seen in the SQUID loop. The pick-up loop however does not run through the JJs, allowing less noise in the SQUID loop and voltage over the JJs.

The SQUID is supplied with a current more than twice as large as I_c (two parallel JJs), called the Bias current (I_b). I_b is chosen to purposely allow a biased voltage (V_b) output and to maximise V_{pp}, allowing for larger $\partial V/\partial \Phi$. In the case of negligibly small inductance, the phase differences of the JJs will be related through the equation [21]

$$\delta_1 - \delta_2 = \frac{2\pi\Phi_a}{\Phi_0} \, . \tag{2.3.7}$$

Here δ_1 and δ_2 are the phase differences of the different JJs and Φ_a is the applied magnetic flux. With identical JJ parameters and negligible inductance, the bias current through the SQUID becomes

$$I_b = 2I_c \cos\left(\frac{\pi\Phi_a}{\Phi_0}\right) \sin\gamma + \frac{\Phi_0}{\pi R}\dot{\gamma} + \frac{\Phi_0}{\pi} C\ddot{\gamma} \, , \tag{2.3.8}$$

where R is the JJ normal resistance and

$$\gamma = \delta_1 + \frac{\pi\Phi_a}{\Phi_0} . \tag{2.3.9}$$

The bias current is constant, while the maximum supercurrent in (2.3.8) is modulated with a period of $1\Phi_0$ as follows:

$$I_{C,max} = 2I_c \left|\cos\frac{\pi\Phi_a}{\Phi_0}\right| . \tag{2.3.10}$$

Neglecting capacitance, the modulation voltage can be equated from (2.3.8) as:

$$V(\Phi_a) = \frac{R}{2}\sqrt{{I_b}^2 - {I_{C,max}}^2} \, . \tag{2.3.11}$$

The modulation depth will then be dependent on I_b alone:

$$V_{pp}(I_b) = I_c R\left[\frac{I_b}{2I_c} - \sqrt{\left(\frac{I_b}{2I_c}\right)^2 - 1}\right]. \qquad \textbf{(2.3.12)}$$

The transfer function then becomes

$$\frac{\partial V}{\partial \Phi_a} = -2\pi \frac{I_c R}{\Phi_0} \frac{I_c \sin\frac{\pi\Phi_a}{\Phi_0}\cos\frac{\pi\Phi_a}{\Phi_0}}{\left({I_b}^2 - {I_{C,max}}^2\right)^{1/2}}. \qquad \textbf{(2.3.13)}$$

With negligible inductance and capacitance, the modulation depth and transfer function will be maximised if $I_b = 2I_c$ [21]. A larger SQUID loop inductance or screening parameter (β_L) reduces the modulation depth. The screening parameter is given by

$$\beta_L = \frac{2LI_c}{\Phi_0}. \qquad \textbf{(2.3.14)}$$

If $\beta_L = 1$, the modulation depth is reduced by 50%. However, taking thermal fluctuations into account, values near 1 is often the optimal screening parameter. A larger JJ capacitance increases hysteresis. The JJ resistance reduces hysteresis, provided

$$\frac{1}{2\pi RC} > f_J(I_c R) = \frac{I_c R}{\Phi_0}, \qquad \textbf{(2.3.15)}$$

where $f_J(I_c R)$ is the Josephson frequency (Equation (2.3.4)) at voltage $I_c R$. From this the Stewart-McCumber parameter is formulated as

$$\beta_c = \frac{2\pi}{\Phi_0} I_c R^2 C < 1\,. \qquad \textbf{(2.3.16)}$$

For $\beta_c \leq 0.7$ the SQUID output is non-hysteretic. A value just below the onset of hysteresis is often the optimal β_c. [21]

Thermal fluctuations play a role at any temperature above absolute zero and causes noise current around the SQUID loop and noise voltage over the JJs. The noise current induces a voltage noise at nonzero voltages, while the noise voltage rounds the I-V characteristics at low voltages and reduces the apparent critical current [21]. For thermal fluctuations to be negligible, the thermal energy ($k_B T$, where k_B is the Boltzmann's constant and T the temperature) has to be much smaller than the JJ coupling energy ($\Phi_0 I_c / 2\pi$). From this, the noise parameter is formulated as

$$\Gamma = \frac{2\pi k_B T}{\Phi_0 I_c} \ll 1 \,. \qquad \textbf{(2.3.17)}$$

Figure 11 shows SQUID modulation voltages normalised to $I_c R$ for different values of I_b normalised to I_c. Figures (a) and (c) are for strongly overdamped SQUIDs ($\beta_C \ll 1$), while (b) and (d) are intermediately damped. Figures (a) and (b) are noise free, while (c) and (d) include thermal fluctuations. In practise the best biased current would therefore have to be determined through tests, as the SQUID parameters design and manufacturing has a limited accuracy and predictability. The effect of asymmetry of the JJs can be removed by proper modulation electronics. [21]

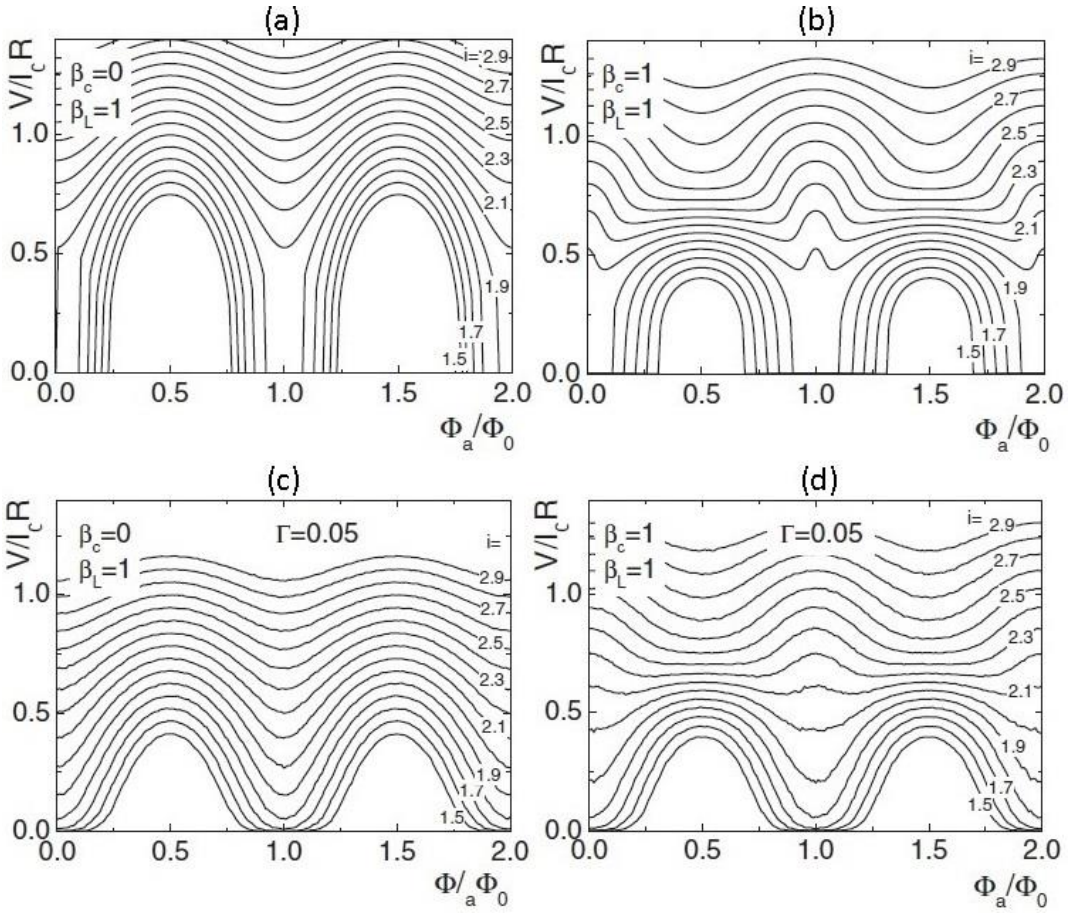

Figure 11: SQUID modulation voltage $V(\Phi_a)$ normalised to I_cR, for several values of normalised current $i = I_b/I_c$. (a) and (c) are strongly over-damped SQUIDs ($\beta_C \ll 1$), (b) and (d) are intermediately damped. (a) and (b) are without thermal fluctuations, while (c) and (d) include noise from thermal fluctuations ($\Gamma > 0$). [21]

2.3.3.1 SQUID Noise

$1/f$ noise at low frequencies can be caused by different JJs' critical current that alternates in or out of phase, noise in I_b, or the movement of vortices. $1/f$ noise as a result of out-of-phase I_c fluctuations can be reduced by alternating the direction of I_b, which is known as the "ac bias reversal" technique. Furthermore, $1/f$ noise can be reduced by the modulation electronics that make use of flux modulation. The movement of vortices plays a bigger role in $1/f$ noise with HTS SQUIDs and cannot be reduced through bias reversal or flux modulation. The only way of reducing this noise is to avoid the vortices or to prevent them from moving. Smaller JJ widths allow less vortices to form and smaller currents to flow, resulting in less moving vortices. Vortices can also be pinned down stronger in artificial pinning sites or flux dams. [21]

In [23], the noise of a SQUID is tested after repeated heating and cooling ("thermal cycling"). After thermal cycling the SQUID 20 times from room temperature, the noise at 1 Hz increased from 70 fT/$\sqrt{\text{Hz}}$ to 1540 fT/$\sqrt{\text{Hz}}$. Another SQUID that had been kept cooled for half a year experienced no perceptible noise deterioration. This is not the same as the Kibble-Zurek theory, in which more vortices are trapped due to faster cooling rates. The extensively high cooling rate when cooled from room temperature causes microcracks in the superconductor film, diminishing its quality. Thermal cycling with high temperature must therefore be avoided to maintain SQUID quality.

High frequency magnetic fields (EMR) distort $V(\Phi_a)$ and reduces V_{pp}. Distortion of the $V(\Phi_a)$ curve around the $\Phi_0/2$ point leads to an increase in the $1/f$ noise of the SQUID output, while a smaller V_{pp} leads to lower sensitivity with more prominent white noise. Flux modulation can use the average value of the output to reduce the $1/f$ noise due to distortion, but EMR must be shielded to reach the maximum amplitude for V_{pp} and reduce white noise. In Figure 11, a SQUID receives microwave radiation at 390 MHz. The radiation intensity is 0.04% (-28 dBm), 0.044% (-27 dBm) and 0.05% (-26 dBm) of the external field. The noise at a bandwidth of 6 kHz and $I_b = 50$ µA then increases from 240 fT/$\sqrt{\text{Hz}}$ to 1.7 pT/$\sqrt{\text{Hz}}$. In the bottom graph it can be seen that V_{pp} decreases by more than 30% as the radiation is increased to 0.05% of the external field. This shows the importance of shielding SQUIDs from EMR. [23]

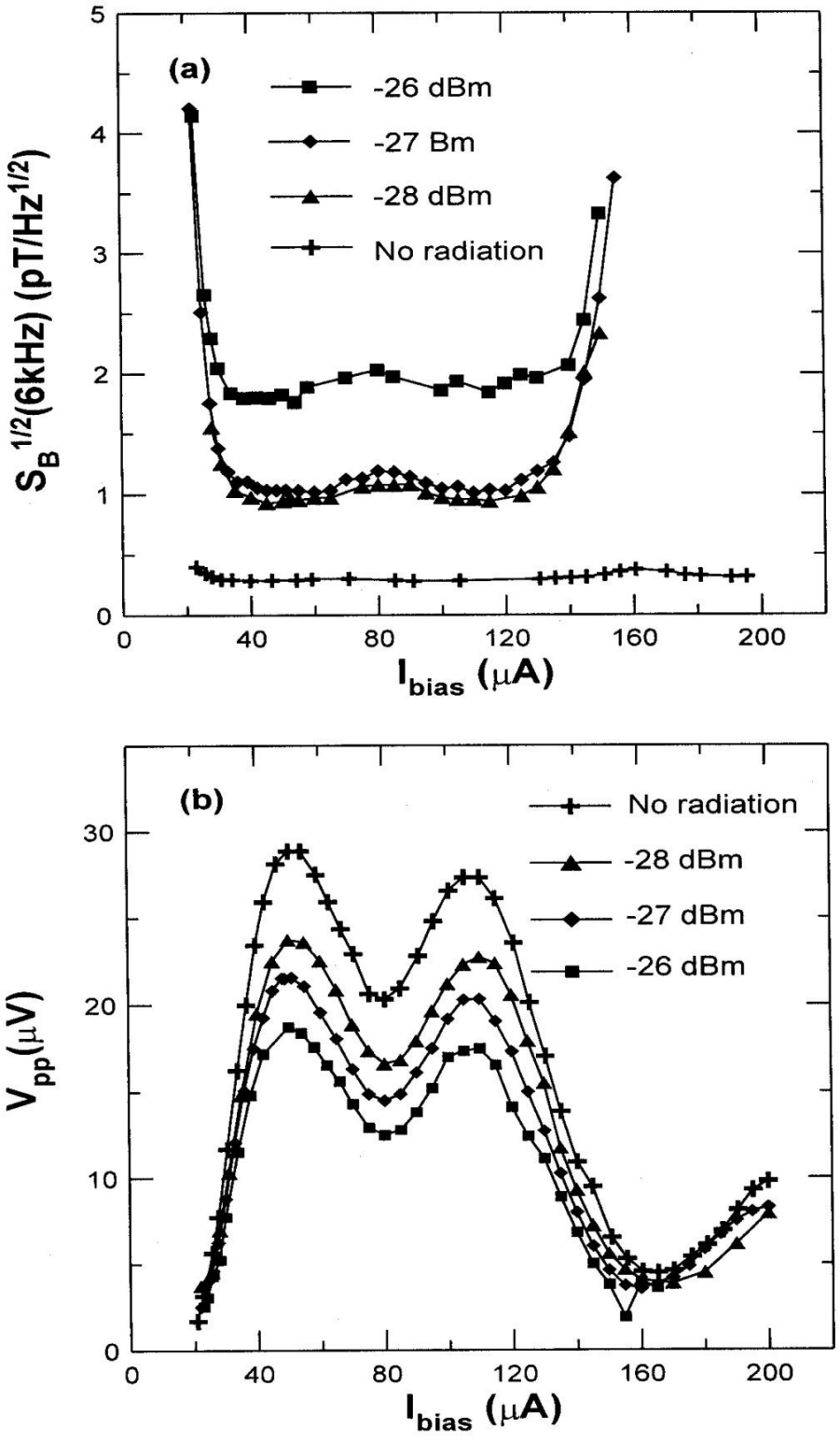

Figure 12: Microwave radiation (390 MHz) of a HTS DC SQUID. Noise at 6 kHz (a) and V_{pp} (b) is plotted against different values of I_b, for different amounts of radiation. [23]

2.3.3.2 SQUID Modulation Electronics

Small-signal readout of SQUIDs only allow a dynamic flux range within the linear region of $V(\Phi_a)$, where $\partial V/\partial\Phi$ is constant, typically resulting in a range less than Φ_0/π. Modulation electronics use a Flux-Locked-Loop (FLL, Figure 13 (b)) to linearize the SQUID voltage, which allows increasing the dynamic flux range by orders of magnitude. [21]

After an appropriate I_b is selected to maximize V_{pp}, the FLL locks in on a work point (W in Figure 13 (a)) at the steepest part of the modulation voltage $V(\Phi_a)$, where $\partial V/\partial\Phi$ is maximised. This allows a small change in flux to be translated into a large change in $V(\Phi_a)$. The voltage at W is known as the bias voltage V_b. V_b is used as a reference voltage in the preamplifier. The difference between $V(\Phi_a)$ and V_b due to a change in flux is then amplified and integrated, resulting in the feedback voltage V_f across the feedback resistor R_f. The current of the feedback loop drives a feedback coil, which is coupled to the SQUID with mutual inductance M_f, maintaining the SQUID at V_b by supplying negative feedback flux. The output sensitivity (V_f/Φ_a) can be increased by increasing R_f or decreasing M_f, which also results in decreased dynamic range and a lower slew rate. If the dynamic range is exceeded, the modulation electronics resets to allow the FLL to lock in on a new work point. By programming a data acquisition (DAQ) device to count flux quanta, the dynamic range of the modulation electronics can be negated. Before the modulation electronics range is exceeded, when the magnetic field has changed by an integer amount of flux quanta, purposely resetting the modulation electronics allows an almost unlimited dynamic range if the flux quanta is counted. [21]

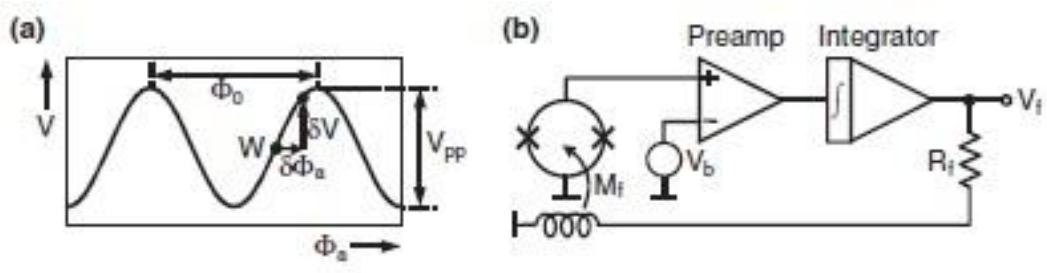

Figure 13: Flux Locked Loop: (a) Small-signal SQUID output $V(\Phi_a)$, with workpoint indicated (b) Circuit diagram of a basic FLL. [21]

As mentioned in the previous section, the modulation electronics uses bias reversal and flux modulation to reduce noise and hysteresis. Bias reversal entails changing the direction of the bias current, while flux modulation entails increasing and decreasing the feedback coil flux to jump between two work points with the same V_b.

Figure 14(a) shows how $V(\Phi_a)$ normally changes with a small change in magnetic flux, at four different working points with positive and negative I_b. Figure 14(b)-(d) shows the effects of different types of noise sources. Out-of-phase critical current fluctuations or magnetic flux fluctuations (Figure 14(b)) can be reduced by determining the difference in voltage change between working points 1 and 4 or 2 and 3 using bias reversal. In-phase critical current fluctuations (Figure 14(c)) due to voltage fluctuations can be reduced by determining the difference in voltage change between working points 1 and 2 or 3 and 4 with flux modulation. The preamplifier voltage fluctuation (Figure 14(d)) is reduced by both bias reversal and flux modulation, but is usually less than the internal SQUID noise. [21]

The flux modulation frequency must be selected as an integer multiple of the bias reversal frequency, which must be considerably higher than the $1/f$ corner frequency (typically 100 Hz) to reduce $1/f$ noise. The modulation flux must be carefully selected that the working points have the same V_b at adjacent sides of the curve. Different bias current values will also require different modulation flux. [21]

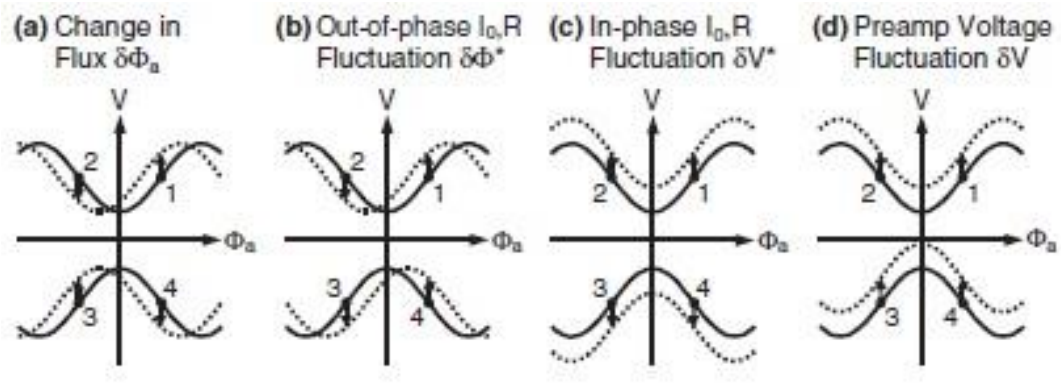

Figure 14: Sources of noise and modulation schemes. [21]

When V_f suddenly changes by an integer number of Φ_0, it is known as a flux jump. Flux jumps occur when the modulation electronics resets or the slew rate is exceeded, causing it to lock onto a new work point an integer number of flux quanta away from the original. The FLL detects changes in the modulation voltage $V(\Phi_a)$ and uses the constant valued transfer function $\partial V/\partial\Phi$ at the work point to generate feedback flux. When the slew rate is exceeded, the applied flux changes faster than the feedback coil can generate feedback flux, causing the modulation voltage to stray beyond the linear flux-to-voltage region of $V(\Phi_a)$. Less feedback flux will then be generated due to the non-linearity of $V(\Phi_a)$. When $V(\Phi_a)$ strays further than $\Phi_0/2$ from the work point, the FLL loses flux lock and a flux jump occurs. To maintain flux lock, the applied flux change $\partial\Phi_a$ must be smaller than $\pm\Phi_0/2$. Accuracy is only maintained if $\partial\Phi_a \ll \Phi_0$, well within the linear flux-to-voltage region of the modulation voltage. When the modulation electronics resets, the total flux change that the feedback coil was preventing is allowed to occur unopposed. When the FLL then continues normal operation, it will lock onto the work point where $V(\Phi_a)$ is closest to V_b. If the total amount of flux the feedback coil was opposing exceeded $\Phi_0/2$, the FLL will lock onto a new work point Φ_0 away from the original. This is represented by the grey area in Figure 15, if the output is more than $\Phi_0/2$ away from V_b and the FLL is reset, the output will drop back into the grey area, resulting in a flux jump. [21]

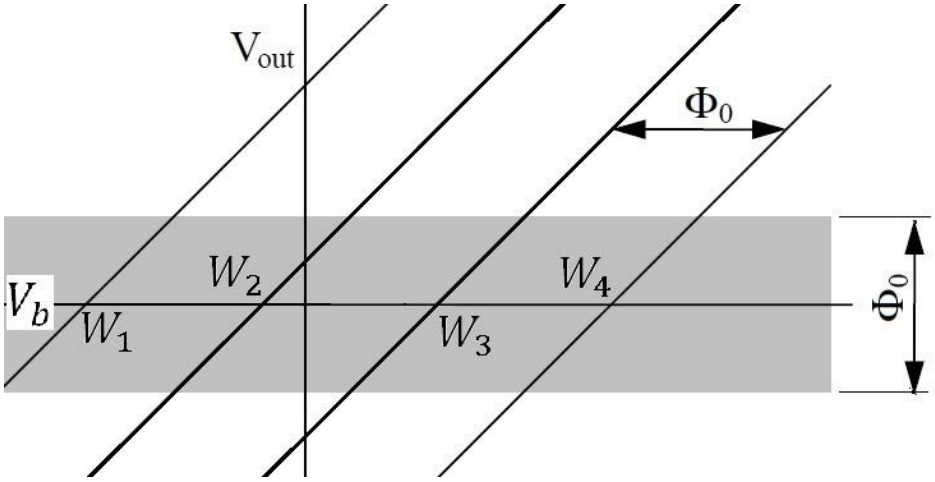

Figure 15: SQUID calibration curves locked to different working points.

2.4 Magnetic and EMR Shielding

EM interference (EMI) is EMFs that inhibit electrical components from achieving optimal performance. Magnetic and EMR shielding generally refers to the insertion of a conductive or high permeability metal, to prevent EMI from being transmitted between spaces. EMI can be reduced by reflecting or absorbing the EMF before it reaches the components. This is somewhat confusing, as shielding implies reflection of EM waves, while absorption is considerably more important when designing shields.

EM absorbers are generally elastomer foams or rigid plastics with conductive or high permeability filler material, used to absorb EM waves with minimal reflection. Absorbers are used to reduce EM wave reflection off surfaces, absorb standing waves in conductive cavities, or to absorb EM waves between two spaces (insertion loss absorbers). Shielding has the same function as insertion loss absorbers, with the distinction of usually being a solid metal and not specialising in minimising reflection. [24]

Magnetic shielding refers to redirecting DC magnetic fields, while EMR shielding refers to reflecting and attenuating higher frequency EMR. EMR shielding design has many engineering principles, but only the general frequency dependence will be discussed. Magnetic shield design is discussed in more detail to allow understanding the design decisions made in Section 3.3.

2.4.1 EMR Shielding

Generally EMR shielding involves selecting the appropriate thickness of high conductivity metal that would attenuate EMI above a specific frequency. Essentially EMR shields act like low-pass filters. Perforated EMR shields act like band-reject filters. Multi-layer EMR shields attenuate successive reflections between the layers, but is only necessary if the material thickness is limited. In the 1930's, S.A. Schelkunoff discovered that transmission line theory can be applied to plane-wave shielding equations, which allowed much simpler derivations from Maxwell's equations. [25]

Using plane-waves and treating the shield as a homogeneous transmission line of infinite size and thickness w (Figure 16), the shielding effectiveness (SE) is calculated as

$$SE = 20\log\frac{H_i}{H_t} = 20\log e^{\gamma w} + 20\log\frac{1}{p} + 20\log(1 - qe^{-2\gamma w}), \qquad \textbf{(2.4.1)}$$

where H_t is the transmitted magnetic field and H_i is the incident magnetic field. Using the electric field results in the same SE, because EMR field components are directly coupled. The term $e^{\gamma w}$ describes absorption losses (attenuation) due to the waves' propagation through the material, where γ is the propagation constant. p is the product of the transmission coefficients across the boundaries describing reflection losses. $(1 - qe^{-2\gamma w})$ is a correction factor accounting for successive internal reflections, where q is the reflection coefficient. Only a portion of EMFs are reflected depending on the incident angle, while attenuation can reduce EMFs by orders of magnitude depending on the thickness of the material. [26]

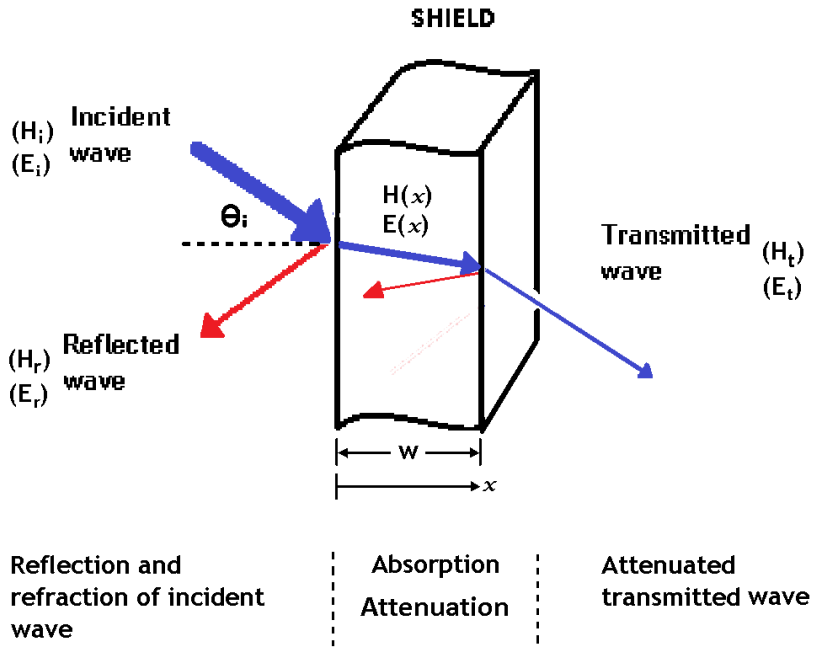

Figure 16: Plane-wave EMF propagation through a conductive medium.

The propagation constant γ (in units of m^{-1}) is the rate at which the field is attenuated while propagating through a medium, and is given by

$$\gamma = \sqrt{j\omega\mu(\sigma + j\omega\epsilon)} = \alpha + j\beta\,. \tag{2.4.2}$$

The real part of the propagation constant is the attenuation constant (α, in units of Np/m) which defines the rate at which the waves are attenuated. The imaginary part is the phase constant (β, in units of rad/m), which defines the rate of phase change as the wave propagates, given by the equations

$$\alpha = \omega\sqrt{\frac{\mu\epsilon}{2}\left[\sqrt{1+\left(\frac{\sigma}{\omega\epsilon}\right)^2}-1\right]} \tag{2.4.3}$$

$$\beta = \omega\sqrt{\frac{\mu\epsilon}{2}\left[\sqrt{1+\left(\frac{\sigma}{\omega\epsilon}\right)^2}+1\right]}. \tag{2.4.4}$$

The phase velocity (Equation (2.1.9)) and wavelength is therefore related to the phase constant through [6]

$$\beta = \frac{\omega}{v} = \frac{2\pi}{\lambda}. \tag{2.4.5}$$

As previously explained, when the loss tangent $\frac{\sigma}{\omega\epsilon} \ll 1$, the attenuation constant will be extremely small and the medium will not absorb EMFs. However the attenuation constant of good conductors only approach zero at frequencies much larger than normally encountered due to their large conductivity and negligible permittivity.

With negligible permittivity, the propagation constant becomes [6]

$$\gamma = \alpha + j\beta = \sqrt{\frac{\omega\mu\sigma}{2}}(1+j)\,. \tag{2.4.6}$$

Attenuation can be described with a distance called the skin depth. The skin depth is the distance over which the wave is attenuated by a factor of *e* in a good conductor and is therefore equated from the absorption loss term as [6]

$$\delta_s = \frac{1}{\alpha} = \sqrt{\frac{2}{\omega\mu\sigma}} = \frac{1}{\sqrt{\pi f\mu\sigma}}\,. \tag{2.4.7}$$

The absorption loss can then be calculated with [27]

$$\begin{aligned} 20\log e^{\gamma w} &= 20\log e^{(w/\delta_s)} && \text{(dB)} \\ &= \ln e^{(w/\delta_s)} && \text{(Np)} \\ &= 8.69\left(\frac{w}{\delta_s}\right) && \text{(dB)} \end{aligned} \tag{2.4.8}$$

Attenuation therefore increases with frequency in good conductors and with shield width. Absorption is the same in the near-field where the wave can be either predominantly E-Field or H-Field instead of plane-waves. Thus absorption is the same for real and virtual photons. For absorption losses greater than 10 dB, reflection becomes negligible [25].

For plane-waves (which are real photons and predominant in the far-field), reflection decreases with increasing frequency. In the near-field, with increasing frequency, reflection decreases if the wave is predominantly E-Field and increases if the wave is predominantly H-Field. Low frequency shielding should therefore be designed for reflection [25, 27].

2.4.2 Magnetic Shielding

Magnetic shielding, or flux shunting, entails reducing the magnetic flux density within an area, by creating a path with lower magnetic reluctance using high permeability metal (Mu-metal). Magnetic flux follows the path of least magnetic reluctance, resulting in the flux being concentrated within the Mu-metal shield layer, preventing the flux from entering the shielded area. The reluctance $\mathcal{R}$ (in units of H^{-1}) is calculated as

$$\mathcal{R} = \frac{l}{\mu A}, \tag{2.4.9}$$

where l is the length of the flux path and A is the cross-sectional area of the material normal to the flux path. From this equation, it would seem that when designing cylindrical magnetic shields, the diameter should be minimised and the shield layer thickness should be maximised to provide the lowest possible reluctance. However, as explained in Section 2.1.3, permeability is a function of the induced magnetic field, which in turn is dependent on the external field and the dimensions of the shield. Magnetic shield design therefore requires optimising the shield dimensions, based on the external field, to achieve the required shielding factor (SF).

The SF is the ratio of the external field (without any shielding) to the field in the centre of the shielded area. When the external field is so small that the Mu-metal remains at its initial permeability, then the thickness can simply be maximised and the diameter minimised to achieve the highest SF.

If the dimensions do not allow the required SF from a single layered design, multilayer shielding is required. Multilayer shields with correct spacing between layers have much larger SF than that of a single layer with the same total thickness. Multi-layer shielding therefore requires optimisation even if the material is at its initial permeability. Empirical engineering calculations can be used to calculate the SF with a low level of accuracy and roughly optimise the dimensions. Even FEM software can be inaccurate due to the unpredictability of the permeability. Shield dimensions obtained while adhering to engineering guidelines are usually adequate.

2.4.2.1 Magnetic shielding design calculations

This section provides empirical engineering calculations used for designing single and double, open end, thin layer cylindrical shields. It should be noted that the equations are only valid for the following conditions [28]

$$\frac{t}{r} \ll 1 \quad ; \quad 2 < \frac{l}{r} < 8 \quad ; \quad SF \gg 1 \tag{2.4.10}$$

where t is the thickness, r is the mean radius and l is the length of the shield layer. The equations are more accurate the more the dimensions adhere to the conditions.

The first step in designing cylindrical shields is to determine the field induced in the shield layer. Provided that the conditions of (2.4.10) are met, the magnetic field induced in the shield can be approximated without needing the permeability, as follows [28],

$$B_S = \frac{2.5 r B_0}{t} \tag{2.4.11}$$

where B_S is the induced magnetic field and B_0 is the external field. Using B_S, the permeability can be found by consulting the B-H curve of the specific Mu-Metal. At lower temperatures the permeability is reduced, but the saturation induction remains the same. The permeability of Mu-metal at cryogenic temperatures is typically reduced to less than 20% of the room temperature permeability.

The transverse shielding factor of a single layer can then be calculated with [29]

$$SF_t = \frac{\mu_r t}{2r} \tag{2.4.12}$$

where μ_r is the relative permeability.

The longitudinal shielding factor of a single layer can be calculated with

$$SF_l = \frac{2D\mu_r t}{r(1+\frac{r}{l})} \tag{2.4.13}$$

where D is the demagnetization factor, calculated as

$$D = \frac{\left(1+\frac{r}{l}\right)}{2f\left(1+\frac{l}{r}\right)}. \tag{2.4.14}$$

The geometrical factor f is fairly constant, with a value of 0.75 for $2 < l/r < 6$ and 0.9 at $l/r = 10$ [29]. The demagnetization factor accounts for longitudinal stray flux, leaking into the shielded area from the magnetized shields, due to the shield's length to radius ratio. Combining Equations (2.4.13) and (2.4.14) results in

$$SF_l = \frac{\mu_r t}{f(r+l)}. \tag{2.4.15}$$

However, some texts calculate the demagnetization factor as [30]

$$D = 0.38\left(\frac{l}{2r}\right)^{-1.3}. \tag{2.4.16}$$

For double layer shields, the transverse and longitudinal shielding factors become [29]

$$SF_t = (SF_{t1})(SF_{t2})d' + SF_{t1} + SF_{t2} \tag{2.4.17}$$

$$SF_l = 2(SF_{l1})(SF_{l2})fd' + SF_{l1} + SF_{l2} \tag{2.4.18}$$

where

$$d' = \frac{1}{2}\left[1 - \left(\frac{r_1}{r_2}\right)^2\right]. \tag{2.4.19}$$

Subscript 1 denotes the inside shield layer and subscript 2 the larger outside layer. The field inside the shielded area can be calculated as

$$B_i = \frac{B_0}{SF}. \tag{2.4.20}$$

Using numerical computing software, Equations (2.4.10) to (2.4.19) can be used to determine the optimal shield dimensions. If the permeability is larger than the initial permeability (typically when $B_S > 1$ mT), the B-H curve data can be used to curve-fit the permeability as a function of B_S.

2.4.2.2 Magnetic shielding design guidelines

The optimal cylindrical shield design is a solid cylinder with no holes where flux can leak. If the design cannot be a solid cylinder and requires material to overlap, the overlap should be at least 10 mm with no spacing between the Mu-metal surfaces [31]. If contact between the surfaces cannot be ensured, the overlap needs to be increased. The design and manufacturing of the shields should take into consideration that shock impact and strain may reduce the Mu-metal's permeability, while cutting and cold working results in localised reduction of the permeability.

A cylindrical shield design should start off by minimising the radius and thickness, to minimise material costs and weight. According to Equations (2.4.12) to (2.4.18), the $SF_l = SF_t$ if $l = 3r$, but will result in transverse flux leaking in from the open ends of the cylinder. Unless the ends of the cylinder are closed with Mu-metal caps, the minimum length should be $4r$ plus the length of the object being shielded. The $2r$ distance between the opening and the shielded object is a compromise between longitudinal and transverse flux leakage. The length should only be decreased if transverse shielding is

not required. If longitudinal shielding is not required, the length can be increased to $l \geq 6r$ to minimise transverse flux leakage.

If the calculated B_S is below the initial permeability, the thickness can be increased as much as possible to increase the SF. If the required SF cannot be achieved before the minimum thickness is doubled or by selecting a material with higher initial permeability, then double layer shields should be used. The optimal spacing of the outside shield layer at the initial permeability is $r_2 = \sqrt{3}r_1$ according to Equations (2.4.12) to (2.4.19).

If the calculated B_S is larger than the value at which the maximum permeability is achieved on the B-H curve (close to or above the saturation induction), the thickness should be increased to decrease B_S to just below the maximum permeability. A material with a larger saturation induction can be chosen if it can provide the required SF. If the required SF cannot be achieved or if the material remains saturated before the minimum thickness is doubled, then double layer shields should be used. The outside layer should have a high saturation induction, while the inside layer should have a large initial permeability. By equating the outside layer SF, the field that the inside layer will experience can be estimated using Equation (2.4.20) and multiplying it by two. Depending on the level of saturation in the outside layer, it can either be spaced to achieve its own maximum permeability, or to allow the inside layer to achieve its maximum permeability. Further optimisation is therefore dependent on the required SF and the specific Mu-metals B-H curves.

2.5 Literature Review Conclusion

This chapter starts by explaining the constituents and propagation parameters of EMFs. This provides the base knowledge required to understand how EMFs propagate depending on their energy and distance from the source, from static fields (dipoles) to high frequency EMR. Permeability and permittivity relates to dipole reorientation and migration, which is dependent on how many weakly bound electrons can respond to EM energy without being freed from their orbitals. Conductivity relates to the mobility of free charge, which is dependent on how many electrons are free, or can be freed for a specific intensity of EM energy. This explains why higher frequency EMFs are not conducted through polarization of the medium and leads to attenuation though free charge.

The geomagnetic field spectrum is briefly explained to allow understanding the SQUID operating conditions and what to expect from measurements. With the basic theoretical background of the SQUID understood, it should be clear how to achieve better sensitivity. A smaller critical current is due to less Cooper pairs being available to conduct supercurrent. A smaller critical current also means the modulation depth and hence the transfer function will be reduced, resulting in a less sensitive SQUID. The critical current is reduced when the Cooper pairs are broken up by EMR or heat, or when the Cooper pairs are used as shielding current for static fields. Defects in the superconducting film allow flux to penetrate the film in quantised flux tubes, causing shielding current to flow around the defects as vortices. More shielding current and vortices are created when the superconductor is exposed to larger static fields. The Kibble-Zurek theory explains that more defects are created if the superconductor is cooled down too fast. Therefore sensitivity is improved if SQUIDs are exposed to smaller static fields, less EMR and cooled down to lower temperatures at a slower rate.

Knowing the SQUIDs shielding requirements, the relevant EMF shielding is briefly explained and better understood with knowledge from the first section of this chapter. Static fields are redirected with Mu-metal and EMR is attenuated with high conductivity metal. Lower frequency EMFs, which do not necessarily diminish SQUID sensitivity but might require shielding, should be reflected with multilayer EMR shielding.

Chapter 3

Design and Installation of the Geomagnetometer SQUID System

This chapter describes the initial design and installation of the GSS installed at SANSA, as well as the magnetic shielding designed for noise analysis. Design decisions exceeded the requirements to incorporate some contingency for unknown variables that would diminish the performance. The GSS is divided into two parts, the data acquisition system (DAQ-system) and the SQUID operating platform (3-axis SQUID system).

The first step was to select HTS SQUIDs with sufficient sensitivity, together with their probes and electronics. It was decided to choose Star Cryoelectronics SQUIDs and equipment. A DAQ-unit (analog to digital converter with extra DAQ capabilities) was then tested to determine the DAQ-unit timing specifications necessary to achieve the DAQ-system timing requirements.

After confidence in the necessary DAQ-unit specifications was gained, an appropriate DAQ-unit could be purchased and DAQ-system development could commence. Developing the DAQ-system entailed programming the DAQ-unit and writing software that uploads time-stamped data to the real-time webserver. DAQ-system development became another engineering student's responsibility and therefore does not form part of this thesis. This allowed DAQ-system development and the design, manufacturing and installation of the 3-axis SQUID system to take place in parallel.

After the GSS was installed based on the initial design decisions, the SANSA engineers became more familiar with the equipment and eventually the data was uploaded to the webserver. This chapter therefore concludes the first 4 project goals of the design and installation phase.

3.1 Data Acquisition System Requirements

The M2700 model HTS SQUIDs (Appendix B.1) were chosen for having noise lower than 300 fT/$\sqrt{\text{Hz}}$ above 10 Hz in zero field. Operated in the geomagnetic field, the noise will increase, with added $1/f$ noise. With 2-3 µm JJ widths, the M2700 model SQUIDs will have negligible reduction in its critical current due to external magnetic fields (explained in Section 2.3.2.2).

The three SQUIDs are each connected to their own modulation electronics, called programmable feedback loops (PFL, PFL100) The modulation parameters are programmed into the PFLs through serial control code (SCC) generated in the PC interface unit (PCI, PCI-1000). Each PFL is connected to the PCI via their own DB-9 connection cable, which is used to output their ±10V analog signals and receive SCC from the PCI. The PCI is connected to a PC through a RS232 connection. The PCI can be programmed to perform simultaneous signal conditioning of the analog signals received from the PFLs, which are all again output to single ended pins on a DB-25 female connector on the rear of the PCI. This DB-25 female connector can then be attached to a DAQ-unit. The DAQ-unit is also connected to a GPS receiver to allow synchronization with Universal Time Coordinated (UTC). The SQUID electronics operation, functions and software are thoroughly explained in the pcSQUID User's Manual [32]. Only the information relevant towards design decisions is further discussed.

The minimum DAQ requirements were chosen as follows:

- 1 pT field resolution: The resolution should exceed the 1pT sensitivity goal.
- 1 µs timing resolution and accuracy: To allow accurate time-stamping and temporal analysis of SQUID signals, with sample rates between 125 and 1000 Hz.
- ±30 nT dynamic range: To allow sufficient range for analysis of solar quiet-day variations. The dynamic range can be negated with DAQ programming, but was factored into the initial design requirements.

3.1.1 Field Resolution and Dynamic Range

The M2700 model has a typical feedback coil coupling of 17 µA/Φ_0 (this value has high variability between M2700 SQUIDs), which is simply the inverse of the feedback coil mutual inductance M_f of 0.1218 nH ($1\ \Phi_0/\mathrm{A} = 2.07 \times 10^{-15}$ H). Selecting PFL high sensitivity mode, with 1 MΩ feedback resistor (R_f), results in a SQUID calibration of 17 V/Φ_0. The SQUID calibration is calculated as follows

$$\frac{V}{\Phi_0} = \left(\frac{1}{M_f}\right) R_f \tag{3.1}$$

where $(1/M_f)$ is the feedback coil coupling in µA/Φ_0. With a typical pickup loop field calibration of 33 nT/ Φ_0 (which remains relatively similar within the M2700 models), a 515 µV output over the 1 MΩ feedback resistor then induces a 1 pT field over the pickup loop. Smaller mutual inductances (larger feedback coil coupling), leads to larger currents required to generate flux and hence larger output voltages across R_f (larger SQUID calibration). Choosing a SQUID with larger feedback coil coupling, however, reduces the dynamic range, due to the PFLs only having a ±10 V range. Typical M2700 model parameters result in a dynamic range of ±19.417 nT from the start up value, which is below the typical solar quiet-day dynamic range.

A higher resolution DAQ-unit allows more sensitive measurements, which means it is possible to choose SQUIDs with lower feedback coil coupling and larger dynamic range. A ±30 nT dynamic range requires an output of 333 µV to induce a 1 pT field and is achieved with a maximum of 11 µA/Φ_0 feedback coil coupling while using a 1 MΩ feedback resistor for the model M2700 SQUIDs. A 16-bit DAQ-unit has a 305.2 µV/bit resolution for a ±10 V signal range, which would allow a minimum feedback coil coupling of 10.1 µA/Φ_0 to achieve 1 pT/bit field resolution, with a maximum dynamic range of ±32.67 nT. An 18-bit DAQ-unit has a 76.3 µV/bit resolution, allowing a minimum feedback coil coupling of 2.53 µA/Φ_0 to achieve 1 pT/bit field resolution with a maximum dynamic range of ±130.7 nT.

Even though 1 pT field resolution is required, DAQ-units have random noise which may render the first least significant bit (1 LSB) useless. Other errors also diminish the accuracy of the measurements, but can be reduced by keeping the operating conditions constant after calibration. 18-bit DAQ was therefore specified, allowing a higher DAQ resolution, less stringent operating conditions and headspace to increase the dynamic range if necessary. With 18-bits and ±10 V DAQ range, the field resolution (FR) and dynamic range (DR) can be calculated as

$$FR = \frac{10-(-10)}{\sum_{n=1}^{18} 2^{n-1}} \left(\frac{V}{\Phi_0}\right)^{-1} \left(\frac{B}{\Phi_0}\right) \qquad DR = \pm 10 \left(\frac{\partial V}{\partial B}\right)^{-1} \left(\frac{B}{\Phi_0}\right), \tag{3.2}$$

where (B/Φ_0) is the pickup loop field calibration. Figure 17 shows 18-bit DAQ FR and DR for the M2700 model SQUID ((B/Φ_0) is assumed to be 33 nT/Φ_0) as a function of the SQUID calibration. 16-bit FR would simply be four times larger, while DR remains the same. For compatibility with other SQUID models, Figure 18 shows B/Φ_0 and V/Φ_0 required to achieve different field resolutions with 18-bit DAQ.

If the DAQ-unit is programmed to reset the PFLs when the PFL output comes close to ±10 V, the DAQ dynamic range will be infinite. Modulation electronics lock onto new workpoints when reset, if the measured flux is more than $\pm\Phi_0/2$ from the original locked-on workpoint. The resulting flux jump can be detected by the DAQ-unit and added to the proceeding data. With an output range of ±10 V, a maximum of 20 V/Φ_0 would allow a flux jump to occur when the PFL is reset when the range is exceeded. With 33 nT/Φ_0 pickup loop field calibration and 18-bit DAQ, the maximum field resolution that would allow flux jumps when reset is then 0.126 pT/bit with the model M2700 SQUIDs. Other SQUID models with smaller B/Φ_0 can be used to achieve higher field resolutions while still having 20 V/Φ_0 SQUID calibration (as seen in Figure 18), to allow infinite range through flux jumps.

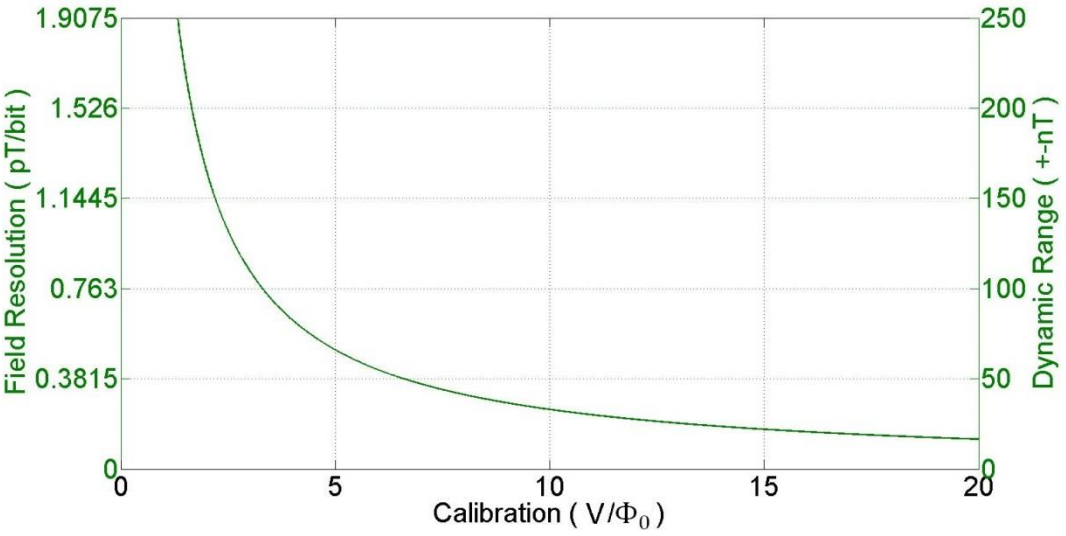

Figure 17: 18-bit field resolution and dynamic range for the model M2700 SQUIDs.

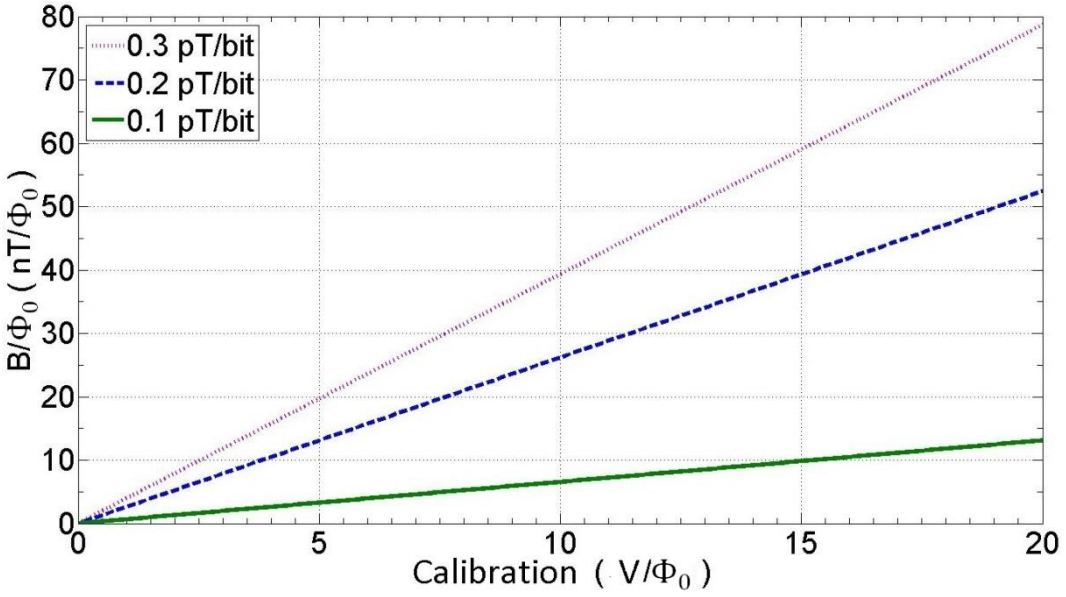

Figure 18: SQUID specification requirements with ±10 V 18-bit DAQ, plotted for three different field resolutions.

3.1.2 Timing Resolution and Accuracy

To allow accurate time-stamping, the DAQ-unit would have to be synchronised to UTC by means of a GPS receiver. A 14-bit DAQ-unit from National Instruments (NI USB-6009) was available to test different sampling methods and gain a better understanding of the timing specifications. The USB-6009 does not conform to the requirements and only has the most basic functions of a typical DAQ-unit. The EVK-6T GPS timing receiver from u-blox was tested and easily achieved location accuracy within 10m, corresponding to timing accuracy of a few nanoseconds. The EVK-6T has a one pulse per second (1PPS) time pulse output and a second configurable time pulse (Time-Pulse-2) which can be set to a maximum of 10.5 MHz. The receiver's clock is continually being disciplined by the navigational data received, which means the nanosecond instantaneous accuracy cannot build up and cause the absolute timing accuracy of the receiver to drift.

The USB-6009 specifies a 100 ppm accuracy of the sample rate, which translates into a 100 µs/s timing accuracy. This means the absolute accuracy will drift 100 µs further each second from the start of DAQ. Using the 1PPS to trigger DAQ at the start of each second would only allow an absolute timing accuracy of 100 µs. To demonstrate the drift in absolute accuracy, the GPS 1PPS was connected to the USB-6009 analog input with a sample rate of 1 kHz. After 228 seconds, the 228th 1PPS was detected at the 228,009th sample, which meant the actual sample rate was 1.0000395 kHz (40 ppm accuracy). The absolute accuracy therefore drifted 40 µs per second, resulting in a 9 ms time shift after 228 seconds. The DAQ-unit would therefore have to have 1 ppm timing accuracy to allow only using the 1PPS to achieve the required 1 µs timing accuracy. However, 1 ppm timing accuracy is impossible using regular crystal oscillators found in DAQ-units. The Time-Pulse-2 from the EVK-6T should therefore be used as an external frequency source, having a disciplined TCXO with 60 ns accuracy.

When using the Time-Pulse-2 to phase lock with the DAQ-unit's internal clock, the EVK-6T specifies that Time-Pulse-2 should be chosen as an integer multiple of the 48 MHz internal clock period, 8 MHz being the largest possible frequency. The reason for this is that the receiver uses its internal clock as a time base and counts the number of clock periods that would allow a lower frequency to be output to Time-Pulse-2. Only

frequencies with periods being multiples of 20.833 ns can be accurately divided down from the 48 MHz time base. Phase locking is made for synchronisation of clocks, hence it only negates drifting of the internal clock. Phase locking the USB-6009 with the 8 MHz Time-Pulse-2 allows synchronising the clocks every 125 ns. With 100 ppm accuracy, the DAQ-unit would be synchronised to within 12.5 ps of the GPS receiver's accuracy. Many DAQ-units have phase lock abilities, however using Time-Pulse-2 as an external clock source is a more efficient way to improve the timing accuracy, because it requires less processing. The timing resolution and accuracy specifications were therefore chosen to have at least a 100 ppm timing accuracy, external digital triggering at 1 Hz (1PPS) and external clock source of at least 1 kHz (Time-Pulse-2).

Unfortunately the USB-6009 did not have external clock functions, therefore using the 1PPS as a trigger was the only test that could be performed. A finite sampling method was required for retriggering the DAQ at the start of each second. The 1PPS was connected to an analog input channel and a trigger input channel, while two other analog input channels were also read at 1 kHz to simulate the processing that would be required from the DAQ-system. The test showed that the 1PPS was measured at the correct times, however only every 2nd second DAQ was carried out, which meant DAQ could not be completed within one second. The USB-6009 only has one analog to digital converter. Therefore it chooses its convert rate as the sample rate multiplied by the number of channels being converted. The conversion of the channels is then evenly spread out over the 1 ms sampling period, to allow the maximum possible settling time for each measurement. After a channel is converted, the data is first buffered while the other channels are being converted. The data is then only read after all channels are converted and the data bus is not busy. This causes the final sample to be read at the beginning of the next second. The solution to this would be to maximize the conversion rate of the DAQ, without exceeding the slew rate, to allow all channels to be converted at the beginning of the sample period. The remaining sample period time should then be sufficient to allow all data to be read before the next sampling period begins. Unfortunately the USB-6009 does not have the ability to change the conversion rate. Configurable conversion rate (convert clock) would therefore be another specification, however most new high resolution National Instruments DAQ-units have this ability.

3.1.3 Data Acquisition System Conclusion

The chosen 18-bit DAQ-unit main specifications are provided in Table 3.1. To negate random noise of the DAQ-unit, 1 pT field resolution should be acquired from the third LSB. This results in 305.2 µV/pT or 0.25 pT/bit field resolution. From Figure 17 it is seen that 0.25 pT/bit resolution is achieved with a SQUID calibration larger than 10 V/Φ_0.

The absolute accuracy is a function of the internal noise, stability of operating conditions and the conversion rate between channels. The maximum accuracy for the ±10 V range is 500 µV if the temperature is kept perfectly constant from calibration. Residual gain and offset errors causing the 500 µV inaccuracy can only be reduced if the DAQ range is reduced. Using the DAQ-unit's low-pass filter with 40 kHz cut-off frequency can provide slightly better accuracy, but requires much slower conversion rates. The maximum sampling rate for ±1 LSB accuracy is 41.66 kHz for unfiltered measurements (8 µs conversion period for 3 channels) and 6.66 kHz for filtered measurements (50 µs conversion period for 3 channels). Time-stamping the data should take the conversion period into account. As mentioned before, the conversion rate should be maximised to allow sufficient time at the end of each sampling period for processing.

The 50 ppm timing accuracy allows 50 µs absolute accuracy when using only the 1PPS as a trigger, but is negated when using Time-Pulse-2 as an external clock source. The different trigger functions, configurable clock rates and external base clock function provide many different ways of achieving accurate synchronisation with UTC.

To allow infinite range, the DAQ-unit should be programmed to reset the PFLs when close to its maximum range of ±10 V, to allow the PFL to flux jump to a new workpoint. The flux jump value should then be added to proceeding measurement data. This is possible up to a maximum SQUID calibration of 20 V/Φ_0. For 18-bit DAQ this allows a maximum possible sensitivity of 0.126 pT/bit for the model M2700 SQUIDs. Smaller B/Φ_0 is required for higher resolutions with infinite range.

NI USB-6281 Specifications							
Analog input channels	8 differential or 16 single ended						
Analog input resolution	18-bit						
Measurement ranges (V)	±10	±5	±2	±1	±0.5	±0.2	±0.1
Random noise (µVrms)	70	35	15	12	10	9	9
Unfiltered absolute accuracy (µV)	1050	550	230	130	80	43	31
Settling time, unfiltered measurements	8 µs for ±1 LSB accuracy						
Settling time, filtered measurements	50 µs for ±1 LSB accuracy						
Timing accuracy	50 ppm						
Triggering	Digital and analog						
Trigger functions	Start Trigger, Sample Clock, Convert Clock, Sample Clock Timebase						
Counter/Timer external base clock	0 – 20 MHz						

Table 3.1: DAQ-unit Specifications

3.2 3-Axis SQUID System

Only after the SQUIDs and their probe dimensions were known, an appropriate liquid nitrogen (LN2) dewar could be chosen and thereafter designing the 3-axis SQUID system would commence. Choosing a dewar required compromise between its volume, neck diameter and evaporation rate. The minimum possible neck diameter that would circumvent all three SQUIDs while attached to the probes (which are in contact with each other) is 56mm. The Bio34 (Appendix B.2) was chosen for its excellent evaporation rate relative to its large volume and large neck diameter of 89mm, allowing enough clearance to implement shielding around the SQUIDs when required.

Two dewars were purchased from Mac's Cryogenic Services, to allow refilling one while the other is in operation. Initially not having a method of transferring LN2 from one dewar to another, replenishing the LN2 would entail transferring the SQUIDs to the refilled dewar. This causes measurement downtime and high cool down rates, which results in SQUID quality degradation (explained in Section 2.3.2.4). However in the design and installation phase, testing the DAQ and overall system stability required removing the SQUIDs many times more than transferring the SQUIDs between dewars occurred. Luckily not all the SQUIDs would be exposed to this unavoidable thermal cycling. A refilling method will be available by the time system stability is established, allowing all three SQUIDs to be properly utilised with minimal thermal cycling.

A 2x2x2.5m SQUID hut (Figure 19 left) was built to house the 3-axis SQUID system (Figure 19 right), away from sources of EMI and magnetic materials which could alter the local magnetic field vectors. The 3-axis SQUID system consists of the three SQUIDs and their PFLs attached to three probes, which are positioned and lowered into the dewar by means of the SQUID-lift. The PFLs are mounted above the probes which are themselves mounted on the SQUID-lift, securing the probes in position while operational and assisting in handling the probes. The SQUID-lift is mounted on a wood block, which is secured to a concrete pillar. The dewar is also placed on a pillar level with the floor. Both pillars are built on-top of compressed sand and isolated from the rest of the floor to allow fewer vibrations from activity in and around the SQUID hut. The

PCI-1000 together with the rest of the DAQ equipment is situated in the control room, 20 m away from the SQUID hut.

To safeguard against asphyxiation from nitrogen build-up, two oxygen gas detectors (GasAlert Extreme from BW Technologies Ltd) were purchased from Invuyani Safety, one for transportation and another for use on-site. Inexpensive ventilation systems were also constructed for the dewars, using PVC pipes and other low thermal conductivity materials, for use during transportation and during system operation in the SQUID hut.

During the design and installation phase, a manoeuvrable SQUID-lift is required rather than a fixed mounting station for the following reasons:

- To enable removing the SQUIDs from the dewar without having to dismount the probes and disconnect the PFLs.
- Steady and secure manoeuvring of the SQUIDS, probes and PFLs to reduce the probability of human handling error.
- Steady insertion of the SQUIDs into the LN2, alleviating some of the stress due to the high cool down rate when cooled from room temperature.

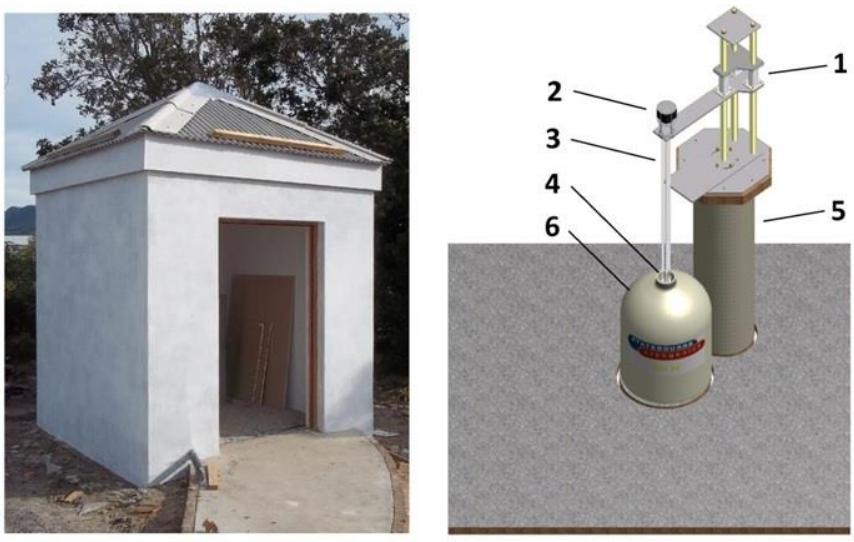

Figure 19: SQUID-hut and 3-axis SQUID system. (1) SQUID-lift; (2) PFLs; (3) Probes; (4) SQUIDs; (5) SQUID-lift pillar; (6) Dewar.

3.2.1 SQUID-lift Design Considerations

The design requirements (functions) of the SQUID-lift were as follows:

1. Mounting: Secure the probes and PFLs to the SQUID-lift, allowing safe manoeuvring of the equipment.
2. Vertical movement: Enable up and down movement of SQUID-lift, for SQUID insertion and removal from the dewar.
3. Horizontal displacement: Enable the SQUID-lift to be moved away from dewar, where probes can be mounted and SQUIDs can be attached safely.
4. Reorientation: Enable redirecting the already mounted probes, allowing SQUIDs to face specified orthogonal directions.
5. Regulated movement: All the SQUID-lift movements should be slow and smooth to avoid handling errors.
6. Lockdown: Preventing movement by clamping/bolting down functional parts.
7. Adaptable design: Easily allowing interchangeable parts and modifications to be made to the 3-axis SQUID system.

The design specifications (limitations) of the requirements are listed below. The requirements that are affected by the specifications are given in brackets.

- Non-magnetic: Only use materials that would not alter the magnetic field vectors. Material permeability should be well within $\mu_0 \pm 0.1\%$, as permeability may vary greatly for different material production processes and after manufacturing of parts. Materials for use in magnetically clean environments are listed in Table 3.2, with air and water as reference. (REQ. 1, 2, 5, 6, 7)
- Probe location: Distance between dewar and SQUID-lift pillar centres is 430mm. With 30 mm clearance between dewar and SQUID-lift pillars, 30 mm tolerance is allowed due to the rounded edges of the dewar bottom not touching the floor, allowing the dewar to be moved off-centre from its pillar. (REQ. 1, 2, 3, 5, 7)
- Dewar neck diameter to SQUID distance: Dewar neck diameter is 89mm. Minimum of 10mm clearance between SQUIDs and neck diameter to allow implementing shielding. (REQ. 1, 2, 4, 6, 7)

- Dewar neck height to SQUID distance: Dewar neck height is 710mm. Minimum of 150 mm clearance between SQUIDs (after probes are removed from dewar) and dewar neck height is required, to allow sufficient space to implement a nitrogen ventilation system or a LN2 refilling system. (REQ. 2, 7)
- Dewar width to SQUID distance: Horizontal displacement should completely clear dewar width of 490mm. Minimum clearance of 200mm. (REQ. 3, 6, 7)
- Dewar bottom to SQUID distance: Dewar bottom is 100mm thick, with an aluminium ring welded on the inside, approximately 30mm thick. 10mm clearance between the SQUIDs and aluminium ring is required for safety and a maximum of 50mm clearance to allow the LN2 to last longer (REQ. 2, 7)
- Ceiling to SQUID-lift distance: The ceiling height is 2,5m. At least 100mm clearance is required between the ceiling and overall SQUID-lift height to allow installation and as contingency if height needs to be increased. (REQ. 1, 2, 7)
- Probe to PFL placement: 225mm connection cable between PFL and probe, with a minimum bend radius of 30mm (REQ. 1, 4, 7)
- Unassisted movement: Gravity should not allow vertical movement speed to exceed 20mm/s. Horizontal movement should require a minimum force of 5 kg. (REQ. 2, 3, 6)

The SQUID-lift design steps were:

1. Conceptual design: Used as visual representation of the SQUID-lift requirements and specifications.
2. Functionality optimisation: The conceptual design was used to seek advice from experienced engineers, resulting in a design with optimised functionality based on the specifications.
3. Manufacturability optimisation: The functional design's manufacturing necessities were reduced to allow faster and complete in-house manufacturing.
4. Cost optimisation: Material cost was reduced from roughly R3500 to R2200 by using smaller parts and less expensive sections (material extrusions).
5. Aesthetics: The design was made to look more appealing.

6. Specification and requirement alterations: The SQUID-lift to dewar centre distance was changed and the SQUID reorientation function added after the SQUID-lift was manufactured. Due to the adaptability of the design, the modifications were easily incorporated into the existing SQUID-lift.

Material	Relative Permeability (μ_r)	For use?
Air	1.00000037	-
Water	0.999992	-
Wood	1.0000043	Yes
** Concrete/Cement	1	Yes
P.V.C and Perspex	>0.999989	Yes
Silicon	>0.99999	Yes
Copper	0.999994	Yes
** Non-ferrous brass / bronze	1	Yes
Aluminium	1.000022	Yes
Austenitic stainless steel	>1.003	No
Stainless steel	>1.02	No
High tensile brass	1.05	No

Table 3.2: Materials for use in magnetically clean environments. Materials marked with ** require testing with fluxgates. [7, 33, 34]

3.2.2 3-Axis SQUID System Conclusion

To achieve the permeability specification, the materials used were Aluminium, wood, engineering polymers and low-tensile Brass bolts, nuts and washers. Stainless steel grade 316 altered the magnetic field vectors with a relative permeability of 1.02. Most aluminium parts were anodised to provide a hardened, non-conductive, corrosion resistant surface layer, while the three long guide shafts were simply alodised to provide corrosion resistance. All bolts used to secure interfaces to each other were provided with surplus hole clearance, to allow interchangeable parts, negating manufacturing errors and for ease of installation.

The final dimensions of the SQUID-lift can be seen in Figure 20. It is possible that minor dimension alterations were made during manufacturing. The pillar height was slightly increased during installation to level the SQUID-lift. With a 30 mm thick wood block between the SQUID-lift and pillar, the SQUID to floor distance will be more than 153 mm. Anti-static, anti-slip, 9mm thick rubber flooring was purchased from Truco and placed underneath the dewar. The rubber flooring prevents abrasion between the dewar bottom and concrete floor and also prevents slipping and damaging the equipment. The clearance between the SQUIDs and aluminium ring at the bottom of the dewar is then more than 14 mm. The 287 mm clearance between the top of the SQUID-lift and roof, allows the SQUID to floor distance to be increased by replacing the 30 mm wood block with thicker material.

The PFLs are mounted above the probes, which are mounted as close together as possible on a rotating mounting disc. The three SQUIDs fit within a 56 mm diameter circumference. The extended plate of the probe lift, where the probes are situated, is clasped between the mounting disc and another disc on the bottom. Clamping down on the extended plate prohibits the mounting disc from rotating for lock down. The rotating mounting disc provides the reorientation function of the SQUIDs, which are mounted 90˚ relative to one another. The SQUIDs are kept parallel with each other by inserting the probes through the holes of the nitrogen ventilation system lid. Rubber grommets are inserted into the holes to provide the lid with a snug fit around the probes.

The centre of the mounting disc is 420 mm away from the SQUID-lift pillar centre. The dewar is moved 10 mm off centre from its own pillar, closer to the SQUID-lift pillar, to align the centre of the probes with the centre of the dewar. This was caused by a measurement error when the specification alteration was made.

Vertical movement is stabilised by using three long Aluminium guide shafts. The guide shaft situated in the centre of the pillar is fixed in position while the other guide shafts can rotate around it. By providing the functional interfaces with tight fitting self-lubricated plain bearings, vertical movement speed is reduced to a crawl. The lift centre of gravity was initially designed to be situated just behind the fixed centre guide shaft. This would allow smooth vertical movement by minimising clenching of the plain bearings on the guide shafts. After alterations the centre of gravity however shifted forward. The plain bearings are made from self-lubricated Vesconite.

Horizontal displacement is achieved by rotating the SQUID-lift around the fixed centre guide shaft. The SQUID-lift can rotate 360˚ if the bolts for lockdown are completely removed, but with the bolts in place, the SQUID-lift can only rotate 90˚. The 360˚ movement is incorporated as contingency for alterations made to dewar position or horizontal movement requirements. Metal surfaces rotating relative to each other are separated with 5mm thick Teflon spacers to ensure smooth operation and avoid galling. The SQUID-lift weight provides sufficient friction between surfaces to allow regulating the rotation speed and avoid unaided movement.

The SQUID-lift was designed as a prototype, because all variables could not be known before the GSS was installed. As the project progresses, the SQUID-lift requirements and specifications will be adapted as design problems are found and the system's requirements become more refined. The prototype was therefore designed with minimal costs, precision and excess clearance, allowing contingency for modifications through its adaptability. When system stability has been reached and a LN2 refilling method has been implemented, the SQUID-lift's functionality will no longer be required. This prototype only served to aid in handling the SQUID equipment during the design and installation phase, to allow testing the GSS and determine the requirements of the specialised SQUID equipment.

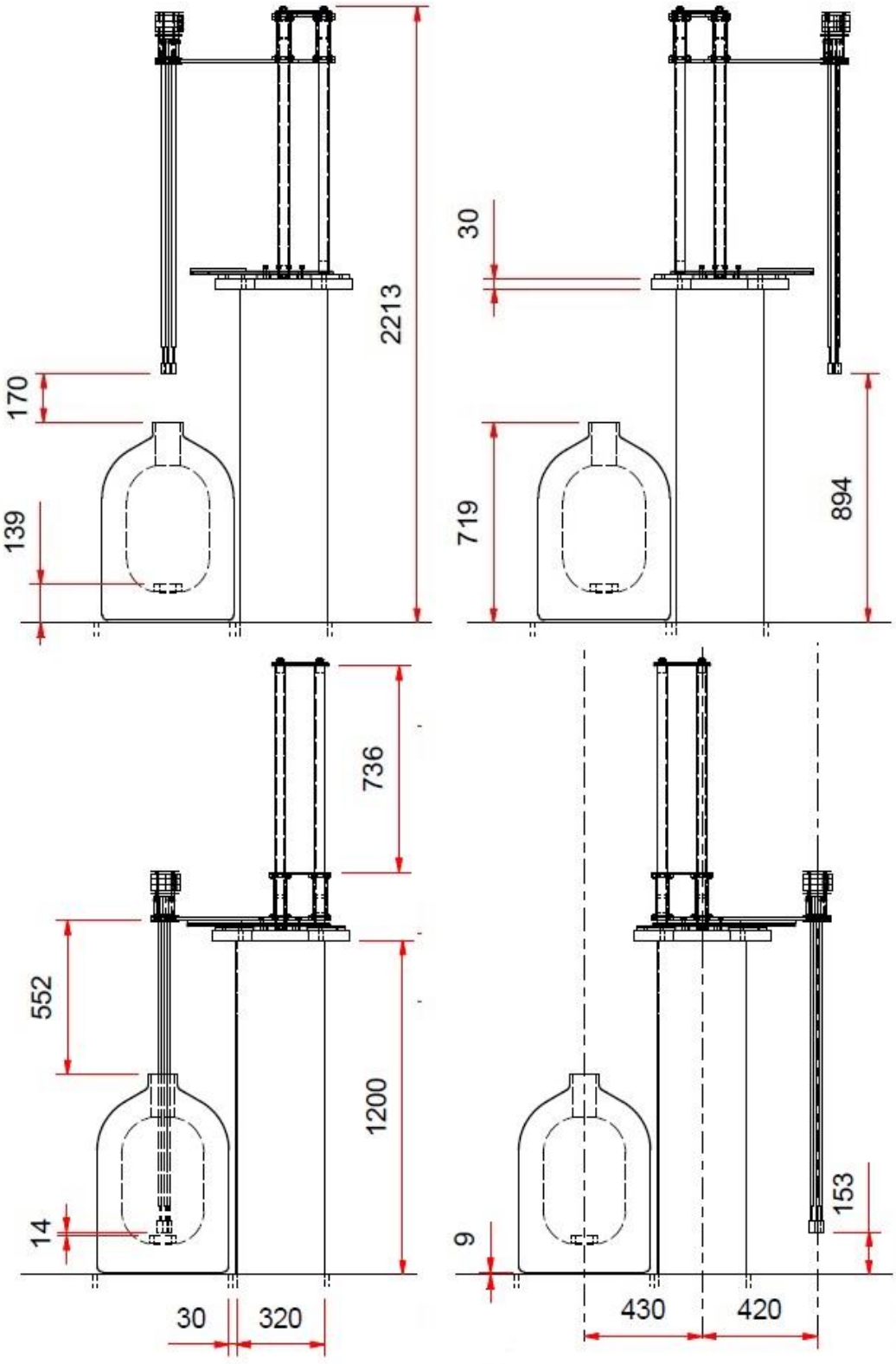

Figure 20: SQUID-lift dimensions. 9 mm rubber flooring included. 30 mm wood block.

3.3 Magnetic Shield Design

Magnetic shields were designed in case the SQUIDs did not function in the geomagnetic field ($B_0 < 27\ \mu\mathrm{T}$) or to allow testing DAQ sensitivity without geomagnetic field variations. Shielded measurements will also have less internal SQUID noise due to less vortices having formed. This will allow determining how much noise is external to the SQUIDs and its measurement of the geomagnetic field, such as noise from the SQUID electronics, DAQ-unit and EMI on the data cables.

Switching between shielded and unshielded measurements would require first shutting down the modulation electronics, to prevent it from trying to oppose the change in flux, which is far outside of the dynamic range ($\partial\Phi_a$ >700Φ_0 for $\partial B_0 > 23\ \mu\mathrm{T}$ of Z-Axis geomagnetic field). The change in flux will then induce a large amount of circulating supercurrent, which will drastically reduce the critical current density of the SQUIDs. The SQUIDs will then require thermal cycling to allow it to flux lock onto the new external field, with no circulating supercurrent. The thermal cycling cool down rate can however be minimised using the SQUID's built-in heater, minimising defect formation and quality degradation.

3.3.1 Design Considerations

The first limitation placed on the design, was that unshielded measurements would not be carried out while the shield was present in the SQUID hut, as it would alter the magnetic field vectors. The shield would have to be removed from the probes and taken away from the hut after shielded measurements were completed. If the shield was a solid cylinder, it would require removing the SQUIDs from the LN2 dewar to allow attaching or removing the shield. Therefore, the design required the shield to be assembled and disassembled while the SQUIDs remain submerged in the LN2, to avoid uncontrolled thermal cycling.

Considering that the shield would have to be half cylinders, that when assembled, should have overlapping surfaces that are in contact with each other, the half cylinders would have to slide into each other longitudinally to allow contact between all surfaces.

The soft Mu-metal would then be exposed to abrasion and strain due to shrinkage at cryogenic temperatures. The minimum thickness of the shield was therefore compromised and it was decided to use Mu-metal sheets rather than foil, regardless of the dimension optimisation results. Co-Netic AA perfection annealed Mu-metal (Appendix B.5) from Magnetic Shield Corp was chosen for its high permeability.

The design specifications were as follows:

- Minimum inside radius of 29mm: The SQUID probe assembly radius is 28 mm, allowing a minimum of 1 mm clearance between the SQUIDs and shield.
- Maximum outside radius of 41 mm: Dewar neck radius of 44.5 mm, allowing a 3.5 mm minimum clearance.
- Minimum shielded volume length of 40 mm: The SQUID sensor package length.
- Minimum thickness of 0.36 mm: Minimum sheet thickness available.
- Maximum length of 260 mm: Allowing less than 0.7 mm shrinkage.

The geomagnetic field that requires shielding is below 27 μT. With $t = 0.36$ mm and $r = 44$ mm, using Equation (2.4.11) the maximum induced field is calculated as:

$$B_s = \frac{2.5(44)(27 \times 10^{-6})}{(0.36)} = 8.25 \text{ mT or } 82.5 \text{ Gauss}$$

This is very close to most Mu-metal's initial permeability, which allows the inside radius to be minimised and the thickness maximised to increase the SF (Section 2.4.2.2). With 15 mm clearance between the inside radius and dewar neck, a double layer shield design could be used to increase the SF. However, the outside layer radius (r_2) would be less than $\sqrt{3}r_1$ and should simply be maximised. The minimum length is calculated as:

$$l = 4 \times (29 + 44) + 40 = 186 \text{ mm}$$

Simulations were first run to confirm the design guidelines and find acceptable dimensions that would allow contingency for clearance requirements and flux leakage.

3.3.2 Dimension Optimisation Simulation

With the small external field being shielded, the inside shield layer would be at its initial permeability regardless of the dimensions. Increasing the inside layer radius or reducing its thickness would only result in a reduction of the shielding factor. The inside layer radius and permeability was therefore kept constant in the calculations, while varying the thickness, length and outside layer radius. The outside layer would not be at the constant initial permeability. Therefore, polynomial interpolation of the B-H curve data was carried out using the polyfit function in Matlab. The induced field is lower than 83 Gauss and the B-H curve data is not given for induced fields lower than 30 Gauss (Appendix B.5) A twelfth order polynomial (Figure 21) was used to allow the permeability to gradually strive towards the initial permeability (3×10^4).

The simulation results can be seen in Figure 22. The calculations were carried out keeping in mind that the permeability of Co-Netic Mu-metal at 77 K would be 15% of the room temperature permeability [35]. Simulations confirmed that the SF increases when increasing r_2 and t while minimising r_1. The dimensions are shown in Figure 23. The simulation code is provided in Appendix A.1.

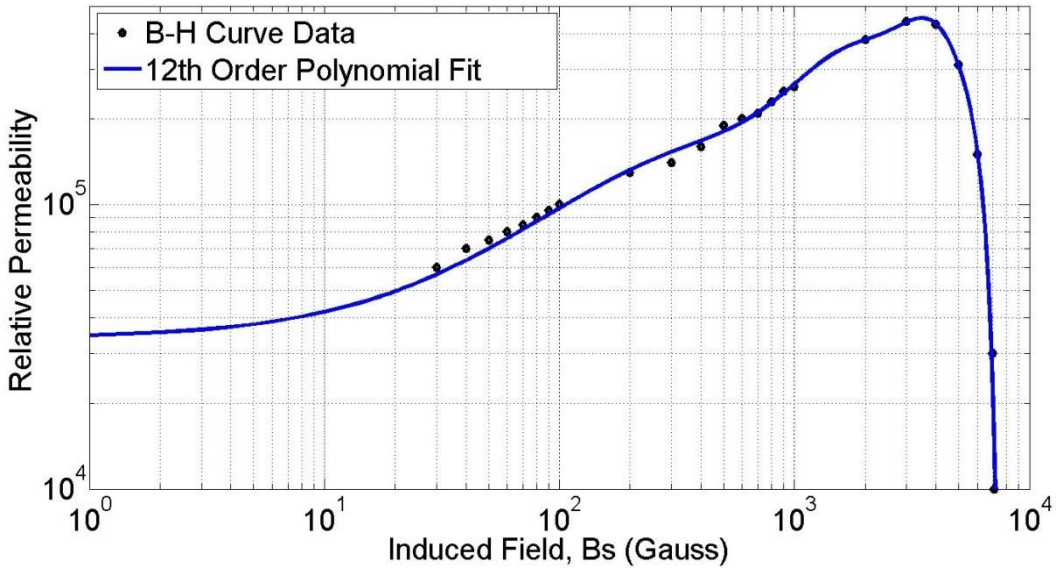

Figure 21: Permeability curve-fit for Co-Netic AA perfection annealed Mu-metal.

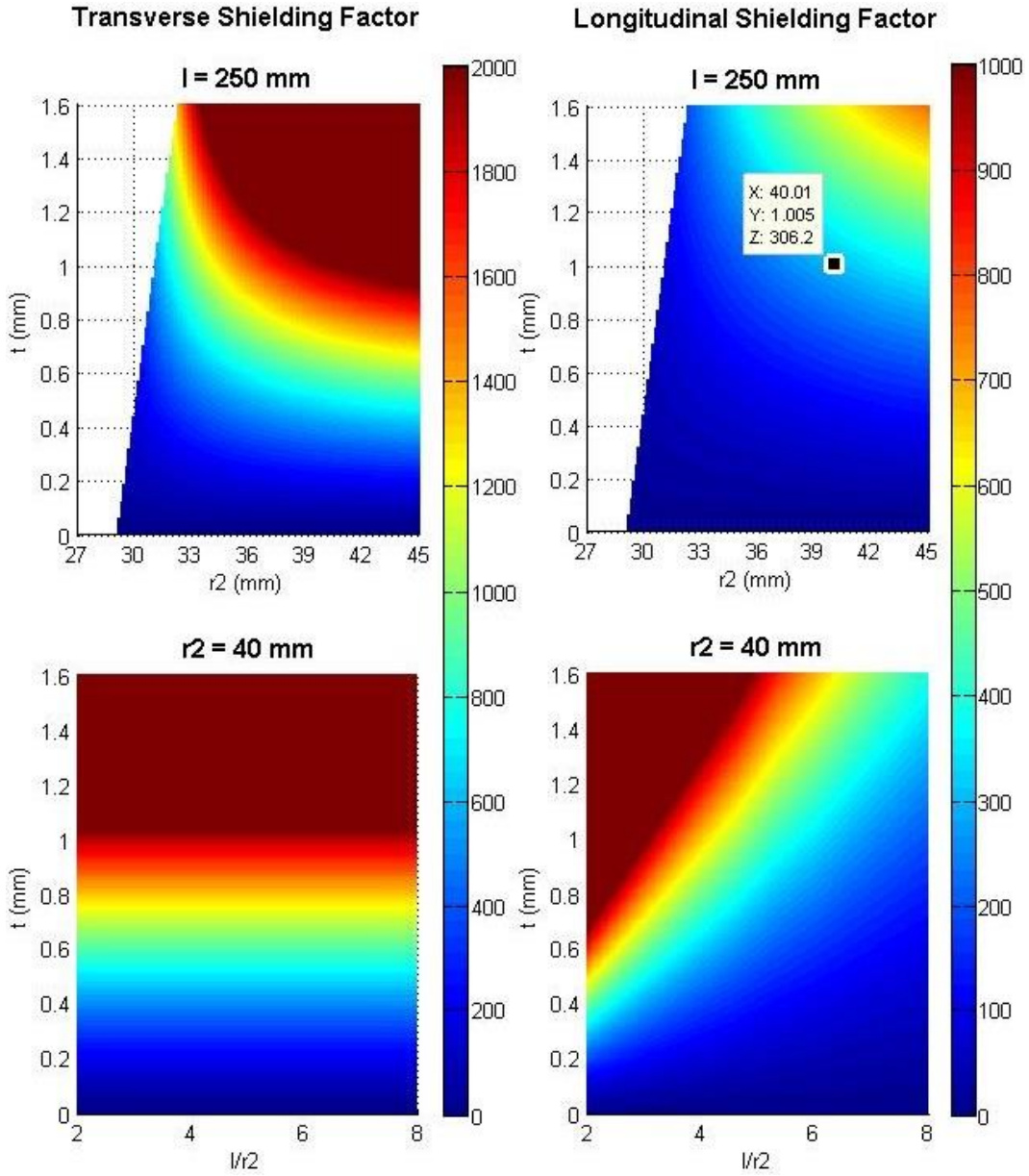

Figure 22: Dimension optimisation of double layer shield. r_1 is 29 mm. Thickness (t) is varied, while the outside radius (r_2) is varied in the top graphs and length (l) is varied in the bottom graphs. Bottom graphs x-axis are the length to outside radius (40 mm) ratio. The transverse Shielding Factor does not account for flux leakage at shorter shield lengths. Shielding Factors are calculated at 77 K, with permeability reduced to 15% of room temperature permeability. The calculated room temperature shielding factors are roughly 37 times larger.

3.3.3 Magnetic Shield Design Conclusion

The shield design comprised of a smaller inner half-cylinder sliding in-between the 10 mm overlapping layers of a larger outside half-cylinder (Figure 23). The outside half-cylinder had the minimum allowable inner radius (29 mm) and maximum outside radius. The maximum outside radius was chosen as 41 mm to allow 3 mm clearance between the shields and dewar neck. With 1 mm thickness chosen, the inner half-cylinder had a 40 mm outside radius and 30 mm inside radius.

The longitudinal SF (SF_l) would be much less than the transverse SF (SF_t) and the shields would therefore be used for transverse shielding. The length was chosen as 250 mm (suggested by magnetic shielding companies) as contingency for transverse flux leakage. The layers of the half-cylinders are separated with 10 mm long aluminium spacers at the ends of the shields, with four 6 mm diameter aluminium rods connecting the spacers with each other. The spacers overlap the ends of the shield layers, clamping down the layers as the rods are tightened. Tests confirmed that epoxy would not hold when exposed to LN2, therefore holes were drilled though the layers and spacers to bolt them together.

The half-cylinder lids were made from aluminium and designed to centre the shields around the SQUIDs, with holes placed off-centre to allow an equal 1.3 mm clearance between the SQUIDs and shield's inner layer. A thin aluminium sheet is connected to the lids and used as a handle during operation. The Mu-metal layers were custom ordered, allowing them to be annealed after bending. The ordered dimensions accounted for the inaccuracy of the bending process and deformation due to annealing.

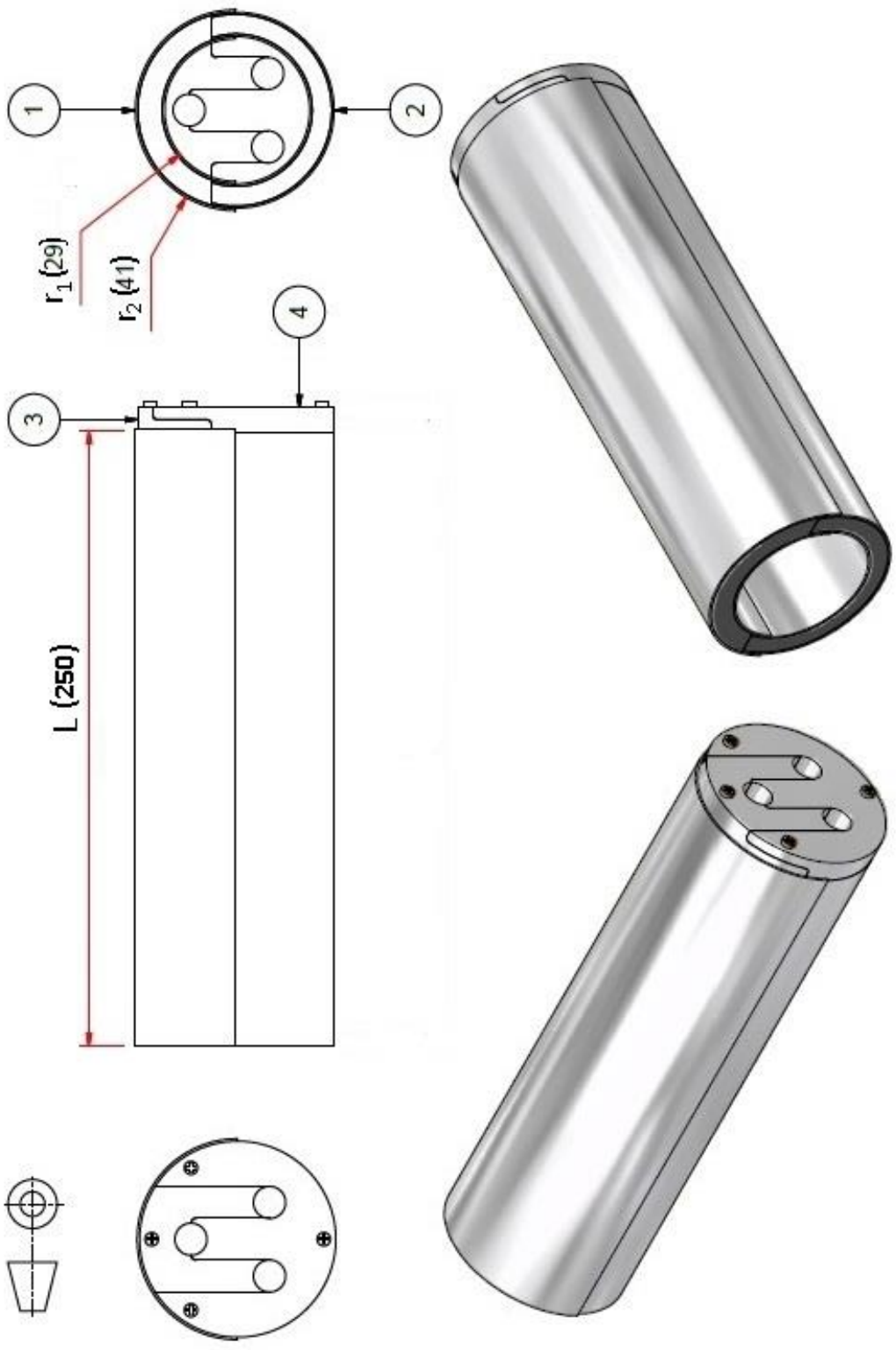

Figure 23: Magnetic Shield design. (1) Outer half-cylinder (2) Inner half-cylinder (3) Outer half cylinder lid (4) Inner half-cylinder lid. Layer thickness is 1 mm.

Chapter 4

Performance Analysis and Recommendations

This chapter analyses the GSS performance after initial design and installation. The recommendations are to allow improving system stability. Improvements for SQUID equipment and operation as geomagnetometers are also suggested. The explanations justify why tests are required, to avoid damaging the SQUIDs with unnecessary tests.

4.1 Magnetic Shield Performance

To determine the SF, measurements were carried out using a handheld 3-axis fluxgate with 1 nT resolution. The shield was orientated so that the geomagnetic field was transverse incident. The shield reduced 25.7 µT transverse fields to below 60 nT in the shield centre, with SF_t larger than 400. According to calculations the room temperature SF_t is 77,000, which should have reduced the field to 0.33 nT. The shield was then placed within another shield to test for residual magnetic fields. With external fields lower than 200 nT, tests showed that the shield had a 60 nT remnant field in the shield centre, which required degaussing. Degaussing could not be performed at the time.

During shield removal from the LN2, ice formed in the holes of the lid, which meant the probes had to be removed from the dewar to remove the shields. After about 30 minutes, the shields could be removed from the probes after warming up to a manageable temperature. Dismantling of the shields while the probes remain submerged therefore did not work, however after thermal cycling from room temperature several times, the SQUIDs have yet to show any sign of quality degradation. The dismantling function could therefore be unnecessary. It is thought that the SQUID package thermal properties are such that cooling does not happen rapidly enough to damage the superconducting film circuits.

4.2 3-axis SQUID System Performance

The 3-axis SQUID system provided all the functions required for initial measurements and tests to be conducted safely, without putting the SQUIDs in harm's way. For practical reasons only the X (geographic North) and Z (vertical) axes SQUIDs were purchased while the Y axis was replaced with a dummy probe for the time being. The SQUID-lift fulfilled its requirements with some functionality problems, but could easily be solved with simple adjustments. The root of all the problems that the system prototype exposed was due to interfacing with the probes. The biggest problems encountered were as follows:

1. The probes are not made exactly the same, making it difficult to orientate the SQUIDs perpendicular to each other.
2. The dewar to probe alignment could not be done accurately and the probes were not straight. This caused the probes to slightly bend when interfacing with the nitrogen ventilation attachment at the dewar's neck, further complicating orientation.
3. The dewar's evaporation rate was four times larger than rated. The most likely sources contributing to the higher evaporation rate is thermal conduction through the probes and black-body radiation into the dewar neck. [36]

Proper orientation is necessary to allow easily comparing the SQUID measurements with fluxgate measurements taken only 50 m away, which is normally used for calibration of the SQUID measurements. The orientation function of the SQUID-lift prototype was reliant on the dimensions and interfacing of all three probes and SQUIDs being more similar. A higher degree of manufacturing accuracy is required from the SQUID equipment to allow sufficient orientation accuracy with the SQUID-lift prototype. The nitrogen ventilation attachment can be removed, but also provides vibration damping and probe alignment with its rubber seals and grommets. The aluminium dewar can be replaced with a fiberglass dewar with a smaller evaporation rate, however the aluminium does provide some EMR shielding. It is recommended that thermal shields be developed for the current Bio34 dewar.

The best solution to all the problems is having Star Cryoelectronics design a single 3-axis SQUID package, in which all three SQUID chips are mounted perpendicular to one another. A single probe, to which the 3-axis SQUID package is connected, would then also have to be designed. This configuration ensures the SQUIDs are perpendicular, allows the direction that the SQUIDs are facing to be known and reduces heat transfer into the dewar. Alternatively, a single probe could be designed that provides three connections for three SQUIDs. However, the perpendicularity of the SQUID orientation would be limited by the manufacturing accuracy of the probe. It would be much easier to achieve perpendicularity with a single 3-axis SQUID package. In either case, the SQUIDs should be provided with sufficient spacing, so that their feedback does not interfere with each other's measurements.

Modifications to the SQUID-lift could provide the required orientation accuracy with a new probe. As mentioned before most of the SQUID-lift functions will not be necessary after system stability has been reached, however it is still recommended that modifications to the SQUID-lift first be made with the new probe. It is not necessary to completely remove the SQUID-lift, as its rotation function allows it to be moved out of the way if a fixed mounting station is to be implemented. Having the SQUID-lift functions available is convenient in case more tests are required at a later stage, which cannot be accomplished with a fixed mounting station without any manoeuvring capabilities.

4.3 Calibration and Slew Rate

The SQUID calibration is done by comparing SQUID data to fluxgate data. According to the SQUID specifications, the vertical (Z-axis) and the horizontal (X-axis) SQUIDs have feedback coil coupling of 13.2 μA/Φ_0 and 10.5 μA/Φ_0 respectively. Having 33.5 nT/Φ_0 feedback coil calibration, results in 0.39403 μA/nT (2.5379 nT/μA) and 0.31343 μA/nT (3.1905 nT/μA) feedback for the Z-axis and X-axis. The voltage calibration changes for different feedback resistors. In Figure 24 the 1 MΩ feedback resistors are used to compare the SQUID and fluxgate spectra. The 1 Hz fluxgate data is filtered from 0.1 Hz, therefore 20 Hz SQUID measurements were digitally filtered above 1 Hz to reduce aliasing. The calibration is chosen to align the spectra at lower frequencies. It was found that the X-axis SQUID's voltage calibration was approximately $\sqrt{2}$ times larger than calculated with the specifications and 1.1 times larger for the Z-axis.

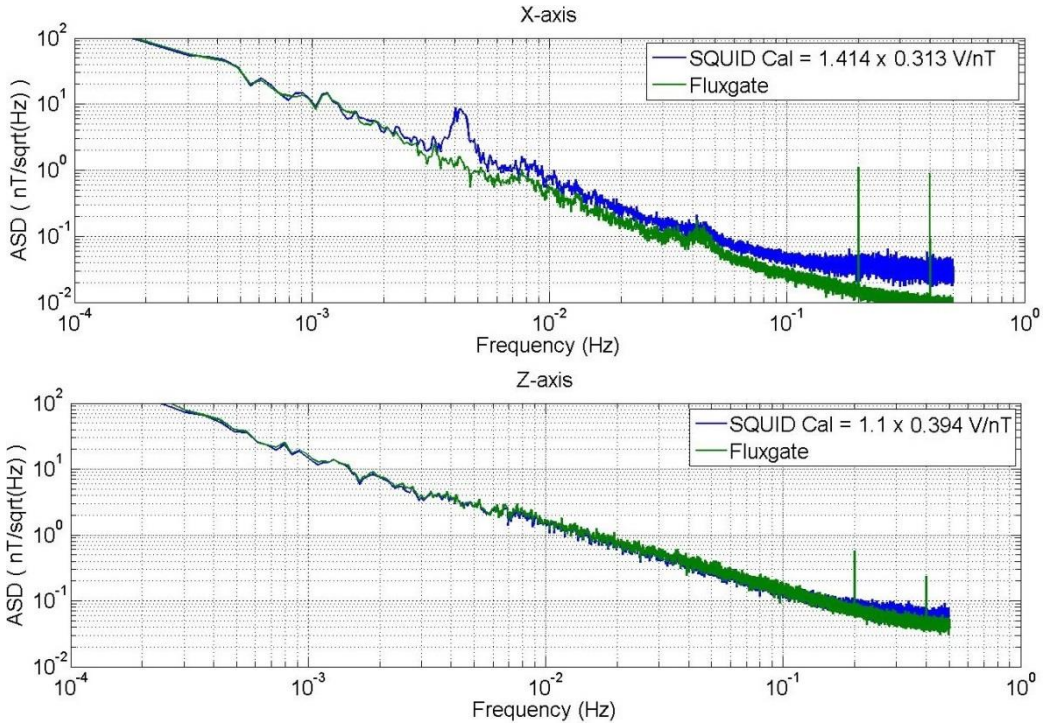

Figure 24: SQUID amplitude spectral density (ASD) using the 1 MΩ feedback resistors compared to the fluxgate spectrum.

The feedback is 0.443 µA/nT and 0.433 µA/nT for the X-axis and Z-axis respectively. Manually resetting the PFLs to force flux jumps resulted in measuring 12.2 $\mu A/\Phi_0$ feedback coil coupling for the X-axis (1.16 times larger) and 14.7 $\mu A/\Phi_0$ (1.11 times larger) for the Z-axis. Larger calibration values allow higher resolution, but the exact reason for the larger calibration has not been determined. The measurements also contained a signal of unknown origin around 4 mHz, with amplitude of roughly 1.5 nT.

The measurements are plotted in Figure 25 using the new calibration values. The Z-axis magnetic field exceeded the PFL's dynamic range due to using the high sensitivity 1 MΩ feedback resistor. This will be overcome after implementing an automatic PFL reset before the range is exceeded. Between 21:00 and 05:00 UTC the X-axis SQUID follows the fluxgate measurements well, however before and after this time, the measurement accuracy slowly drifts. To rule out orientation errors, simulations were run to see if the measurements correlate better at different angles (Appendix A.3). Higher correlation factors were found at different angles, however after plotting it was found that the X-axis SQUID did not follow the fluxgates exactly at any angle. It is thought that environmental noise sensed by the SQUID exceeds the PFL slew rate, forcing the SQUID to be operated in the non-linear flux-to-voltage region, where accuracy and sensitivity is reduced. The slew rate could also be contributing to the larger calibration values.

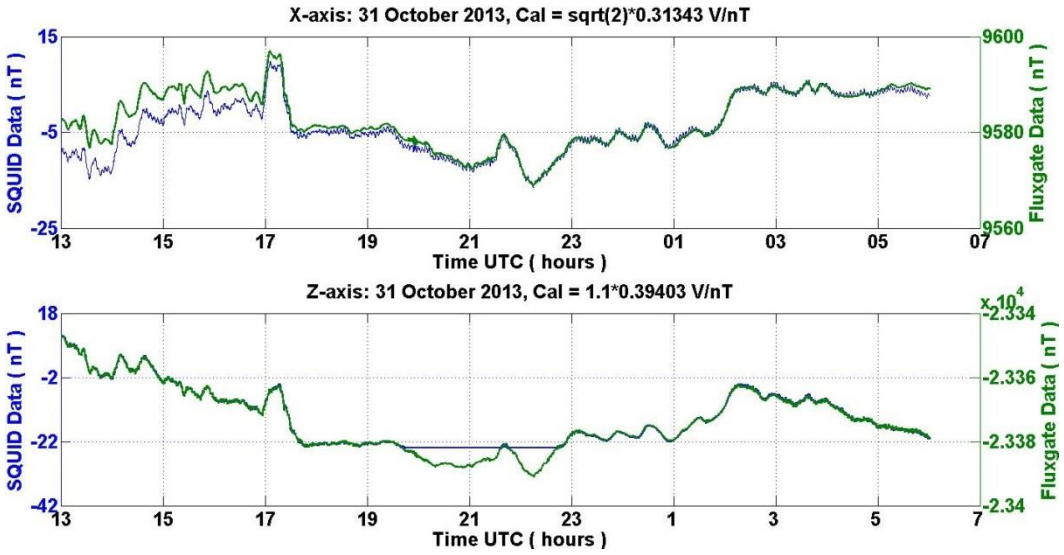

Figure 25: SQUID and fluxgate comparison using 1 MΩ feedback resistor.

The Z-axis SQUID has a 30% larger modulation depth (V_{pp} or "Output" voltage in Appendix B.2 and B.3), which could explain why the Z-axis slewrate is not exceeded, as the slewrate is proportional to the SQUID's V_{pp}. However in Figure 26, using the 1 kΩ feedback resistor to allow a ±250 nT dynamic range, the Z-axis experienced a flux jump due to a transient magnetic field change. As mentioned in Section 3.1.1, flux jumps are not a problem for DAQ. The DAQ should be programmed to detect sudden voltage changes equivalent to integer multiples of $1\Phi_0$ and simply add the value to the proceeding measurement data, completely negating flux jumps. Flux jumps due to transient magnetic field changes however indicate that there is too much EMI present in the measurement environment. If EMI can result in flux jumps, it is very likely that the SQUIDs are regularly operated beyond the linear voltage-to-flux region with reduced accuracy and sensitivity.

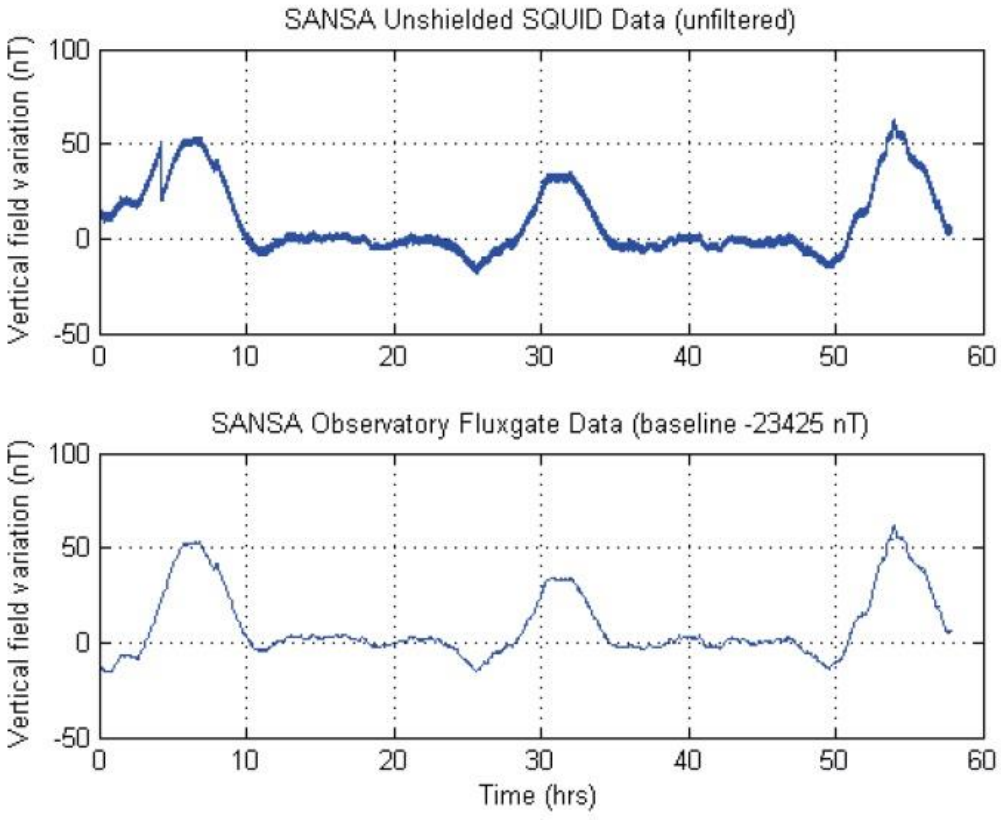

Figure 26: Z-axis SQUID and fluxgate data comparison. 5-7 February 2013. [37]

Proper EMR shielding will reduce the number of flux jumps and also increase the measurement accuracy by increasing V_{pp}. A larger V_{pp} will reduce SQUID internal $1/f$ noise and the impact of white noise (explained in Section 2.3.3.1). The minimum EMR shielding required should therefore attenuate fields to below the PFL slew rate for system stability. More shielding will be required to maximise V_{pp}, minimise internal $1/f$ noise and white noise. The PFL-100 slew rate is not defined in the user-manual. Using the worst case scenario bandwidth, the worst possible slew rate will be estimated.

The -3 dB cut-off frequency is the frequency at which the feedback coil only opposes $1/\sqrt{2}$ of a sinusoidal applied flux at full scale range. The rate of the flux change exceeds the slew rate, causing the SQUID modulation voltage to stray beyond $\partial\Phi_a = \Phi_0/8$ from the work point, where the slope of the modulation voltage is $1/\sqrt{2}$ times the transfer function (for a perfectly sinusoidal modulation voltage). The modulation voltage then generates less feedback flux than required. For clarity, Figure 27 illustrates where the -3 dB flux error occurs.

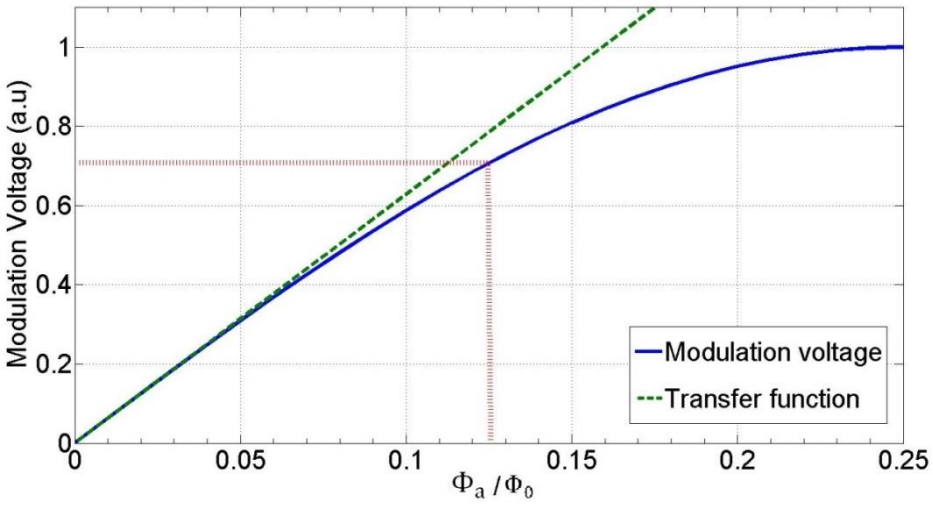

Figure 27: Illustration of -3 dB flux error. The slope of the modulation voltage at $\Phi_a = 0.125\Phi_0$ is 3 dB less than that of the transfer function.

The -3 dB cut-off frequency is calculated as [32]:

$$f_{3\mathrm{dB}} = \frac{(\partial V/\partial \Phi_0)(G_A V_{ref}/14)}{(R_f/M_f)2\pi\tau} \tag{4.1}$$

where $(\partial V/\partial \Phi_0)$ is the SQUID transfer function, (R_f/M_f) is the SQUID calibration (Equation (3.1)), $G_A = 160{,}000$ is the total amplifier gain, $V_{ref} = 5$ V is the multiplier reference signal amplitude and τ is the integrator time constant. The factor of 14 is the voltage scale factor of the multiplier. Unless the integrator time constant is remotely configured in custom mode, the PCI automatically switches the time constant for different feedback resistors, to purposely change the slew rate, allowing the same bandwidth for all sensitivity ranges. [32]

Figure 28 shows the worst possible -3 dB cut-off frequencies as a function of the SQUID calibration in maximum sensitivity mode ($R_f = 1$ MΩ, maximum feedback resistor), $\tau = 1$ ms (maximum integrator time constant) and $\partial V/\partial \Phi_0$ =50 and 100 μV/Φ_0. When the time constants are automatically switched, the cut-off frequency is 10^3 larger.

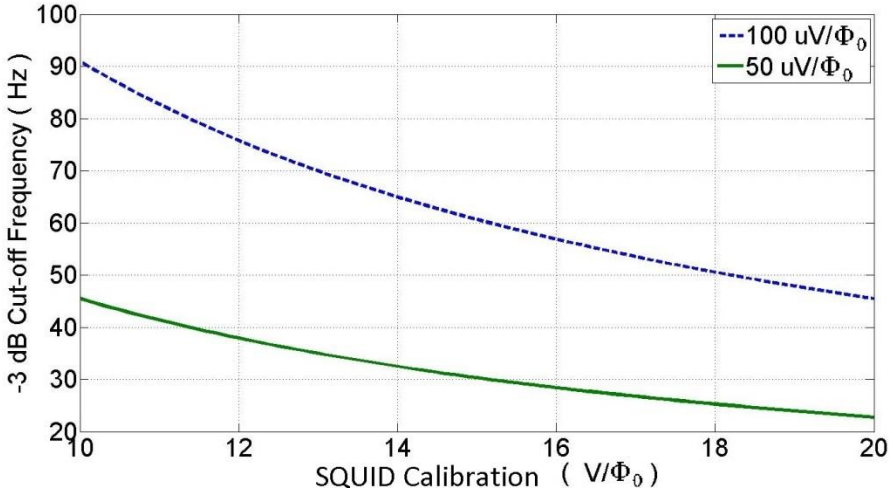

Figure 28: Worst $f_{3\mathrm{dB}}$ when selecting maximum R_f and τ for two $\partial V/\partial \Phi_0$ values.

The full scale flux (Φ_{FS}) is simply the voltage range divided by the SQUID calibration. If the applied flux causing the -3 dB error is $\Phi_{FS}\sin(2\pi f_{3\mathrm{dB}}t)$, the slew rate can be approximated as the maximum slope of the measured flux $\Phi_m = \frac{\Phi_{FS}}{\sqrt{2}}\sin(2\pi f_{3\mathrm{dB}}t)$. The slew rate is therefore estimated as:

$$\left(\frac{\partial \Phi_m}{\partial t}\right)_{max} = \frac{\Phi_{FS}}{\sqrt{2}} 2\pi f_{3\mathrm{dB}} \tag{4.2}$$

The magnetic field amplitude that exceeds the slew rate can be estimated as:

$$B_{max} = \left(\frac{\partial \Phi_m}{\partial t}\right)_{max}\left(\frac{B}{\Phi_0}\right)\frac{1}{2\pi f} \tag{4.3}$$

where $2\pi f$ is the maximum rate at which the magnetic field changes. In Figure 29 B_{max} is plotted for 2 values of SQUID calibration, using the worst case scenario parameters and assuming a minimum transfer coefficient of 50 $\mu V/\Phi_0$ with pickup loop field calibration (B/Φ_0) of 33 nT/Φ_0. The minimum shielding required should attenuate the fields below the values seen in Figure 29 to ensure system stability through repeated measurement accuracy and increased sensitivity.

EMR shields should be designed and placed around the dewar to shield from RF upwards. The penetration depth of Aluminium for 3 kHz is 1.5 mm. It is recommended that multilayer EMR shields be designed for reflection to shield low frequency EMR, as explained in Section 2.4.1. If the surfaces are made reflective enough, multilayer EMR shields could then double as thermal shields by reflecting black-body radiation. The outside layer will then reflect and attenuate the most EMR. The layers should be separated with low thermal conductivity material. More layers would allow the greatest temperature gradient over the shield's overall thickness. Thermal insulation layered with aluminium foil could serve as a makeshift thermal and EMR reflection shield.

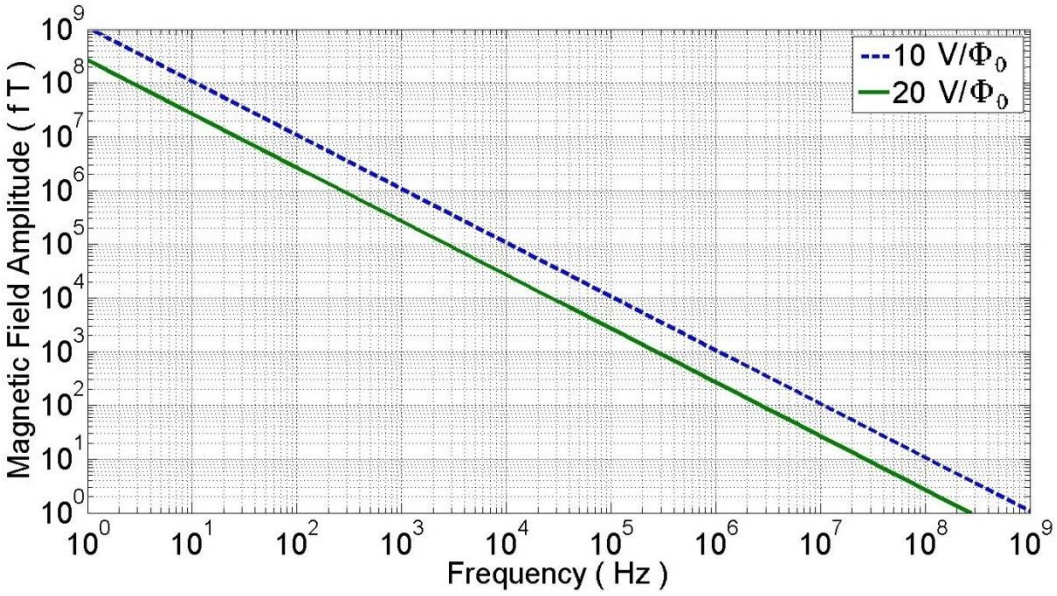

Figure 29: Magnetic field variations that exceed the slew rate, plotted for two values of SQUID calibration while assuming the worst possible slew rate.

4.4 DAQ-system Noise

To test the DAQ-system white noise, measurements were first taken at a sample rate of 2 kHz. Using different feedback resistors (10, 100, and 1000 kΩ) for different voltage calibrations allowed distinguishing between noise sources. The different voltage calibrations results in internal voltage noise (from the DAQ-unit, PCI or noise in the data cables) scaling with the calibration, while external fields and internal SQUID noise remain at the same amplitude. The measurements had to be taken directly after one another to negate changes in field variations at different times of the day. As seen in Figure 2, geomagnetic field variations drop below 1 pT between 1-100 Hz, and then drastically diminish in amplitude beyond 100 Hz. With 70 µVrms random noise in the DAQ-unit and SQUID noise below 300 fT/$\sqrt{\text{Hz}}$, the spectrum will purely consist of noise above 100Hz.

The results of the test can be seen in Figure 30. The mean amplitude spectral density is calculated over 2 minutes, with a 50% overlap 8 second Hamming window (Appendix A.2). The X-axis geomagnetic field variations and 50 Hz powerline noise is approximately an order smaller than that of the Z-axis. As seen with the 50 Hz powerline noise and low frequency Z-axis geomagnetic field variations, external field amplitudes remain fairly constant. With the 10 and 100 kΩ feedback resistors, above 100 Hz the spectrum scales along with the calibration, which means the spectrum consists of internal voltage noise. From Figure 30, the voltage noise floor is roughly 90 μV/$\sqrt{\text{Hz}}$.

Measurements done with the 1 MΩ feedback resistor have a noise floor of roughly 180 μV/$\sqrt{\text{Hz}}$ (400 fT/$\sqrt{\text{Hz}}$). The larger noise floor is due to the addition of internal SQUID noise of 186-272 fT/$\sqrt{\text{Hz}}$ for the X-axis and 168-149 fT/$\sqrt{\text{Hz}}$ for the Z-axis from 10-1000 Hz (Appendix B.2 and B.3). Below 10 Hz the X-axis geomagnetic field variations are not completely distinguishable from voltage noise, which means that the variations could still be smaller than the noise.

Shielded measurements were taken to confirm the source of the additional noise in the 1 MΩ measurements. Measurements were very noisy after submerging the shields in the LN2. The noise was most likely mechanical, due to bubbling of the LN2, air escaping from the shields or shrinking of the shields. The shields were left on overnight with measurements taken at a sample rate of 20 Hz. The measurements started at 12:30PM UTC on 4 November 2013 and continued for 18 hours. In Figure 31 the measurements are compared to fluxgate measurements. The shielded SQUID spectrogram still followed the same trend as the fluxgate spectrogram, which means the fields are not completely shielded. The shields still required degaussing to analyse $1/f$ noise, however above 1 Hz the shielded magnetic field variations were smaller than DAQ-system noise. After approximately 15 hours of settling time, most mechanical noise had subsided and shielded measurements were taken approximately 19 hours after submerging the shields in the LN2.

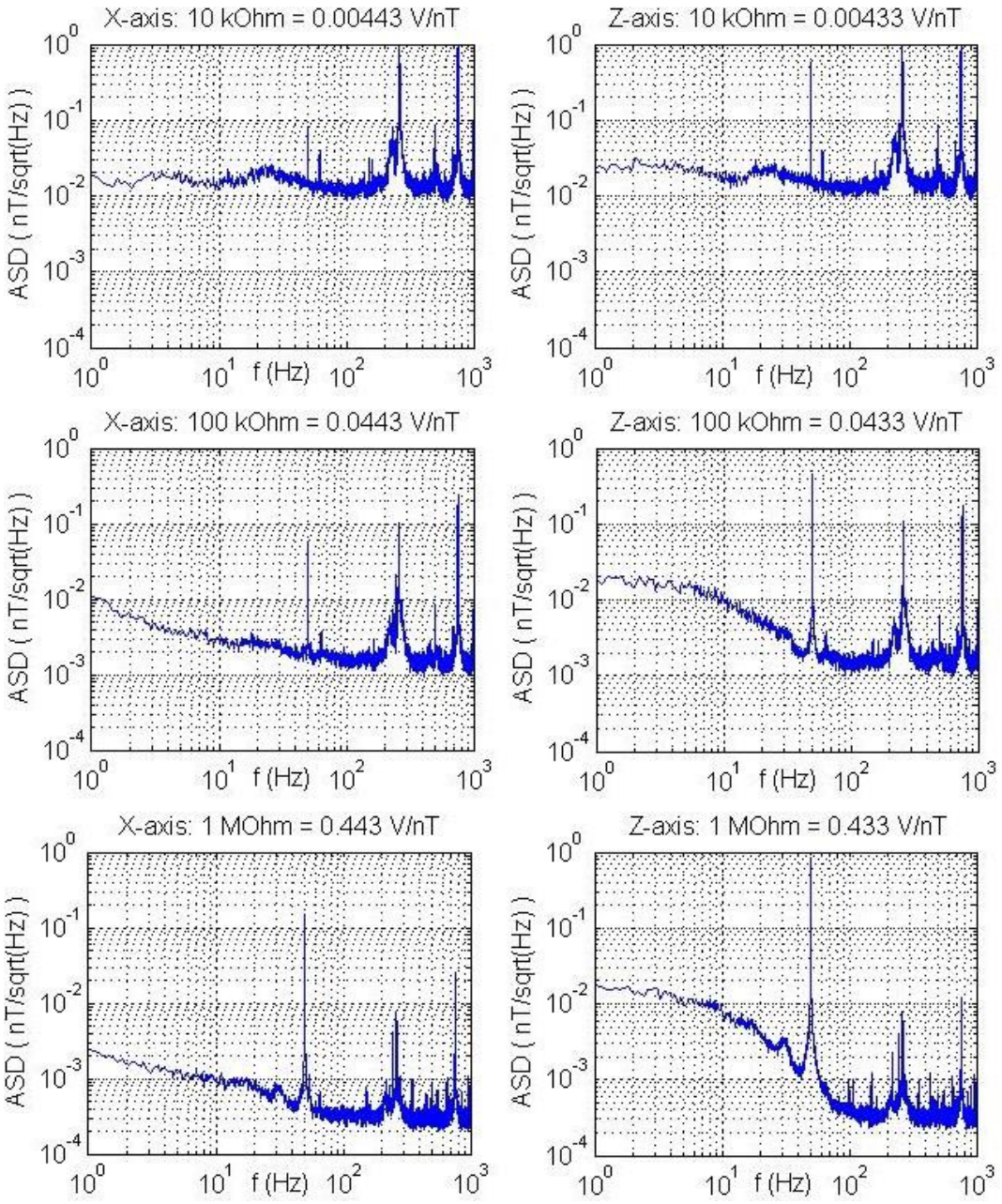

Figure 30: DAQ-system noise spectrum (Amplitude Spectral Density) of unfiltered SQUID measurements for different feedback resistors.

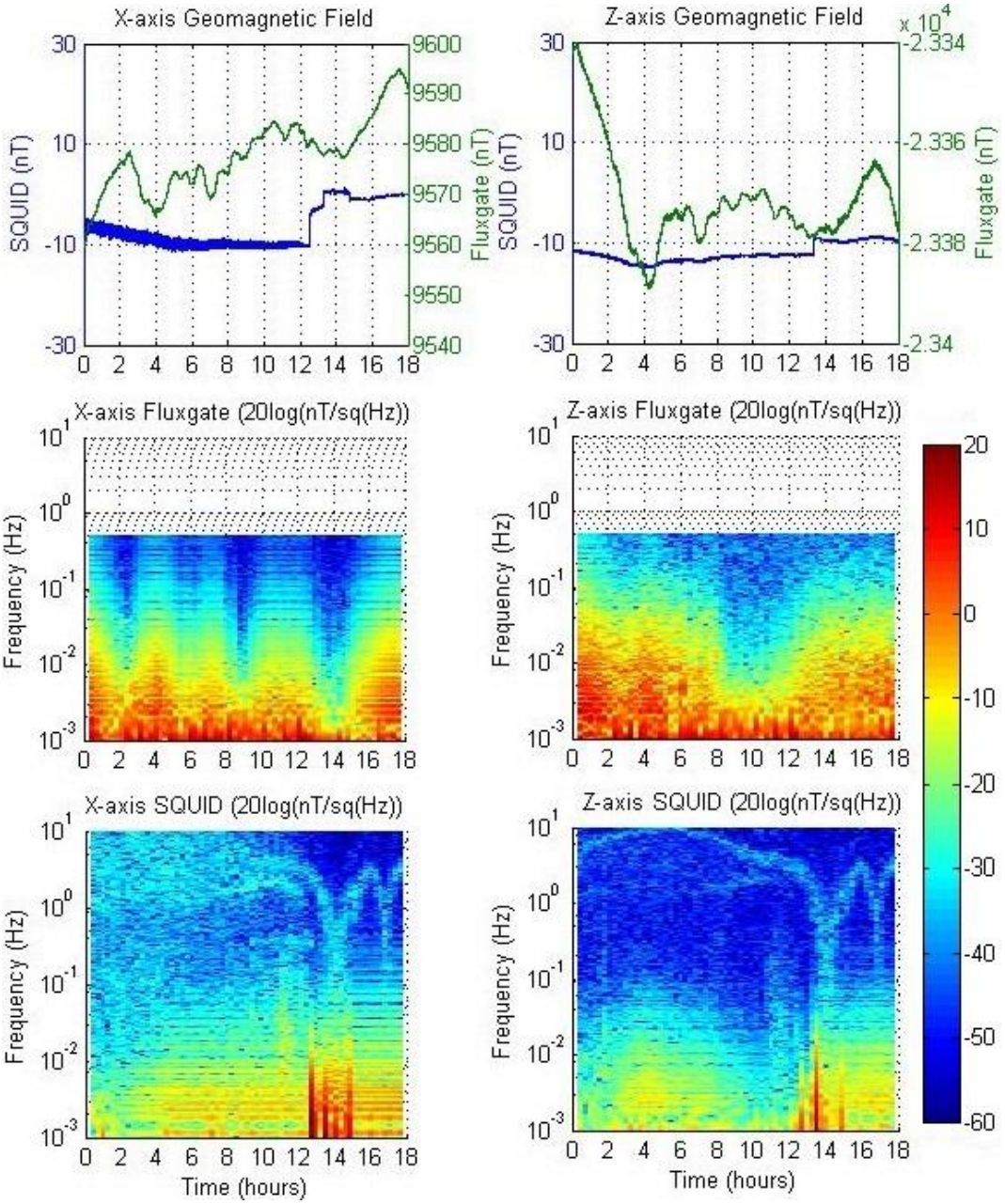

Figure 31: Shielded SQUID measurements after immersion in LN2. Measurements started at 12:30 UTC on 4 November 2013. The amplitude spectral density given in dB.

The shielded results after the shield had settled can be seen in Figure 32. The 50 Hz powerline noise is shielded by a factor larger than 50, which means it is possible that lower frequencies could have had an even larger shielding factor given enough settling time. Unfortunately the shields had already been removed by the time the data was analysed and time did not allow the process to be repeated. The spectrum is therefore purely noise above 1 Hz. The noise floor is reduced to 90 µV/$\sqrt{\text{Hz}}$ as with the 10 and 100 kΩ measurements in Figure 30, which is due to the internal SQUID noise and external fields being reduced by the shields. The measurements also indicate that the SQUIDs have $1/f$ noise when shielded.

Measurements are also filtered before being measured by the DAQ-unit, using a 4-pole, active low-pass analogue Bessel-Thompson filter, with 50 Hz cut-off frequency. Filtered measurements reduced the voltage noise, which confirmed that the 90 µV/$\sqrt{\text{Hz}}$ DAQ-system noise is from the SQUID electronics. The voltage spikes of the unfiltered measurements are summarised in Table 4.1 and are most likely aliasing from the PFL's 128 kHz modulation. After 200 Hz, the filtered measurements reach a noise floor below 9 µV/$\sqrt{\text{Hz}}$. This noise is from the DAQ-unit.

With less than 300 fT/$\sqrt{\text{Hz}}$ SQUID noise and 90 µV/$\sqrt{\text{Hz}}$ SQUID electronics voltage noise, the calibration is required to be larger than 0.3 V/nT to fully utilise the SQUIDs sensitivity potential. This is only achieved using the 1 MΩ feedback resistor. The mean filtered SQUID noise and SQUID electronics noise will then both be less than 1 pTrms. With the normal 125 Hz sampling rate, the DAQ-unit noise will then contribute to 100 µVrms noise, or less than 0.33 pTrms for a calibration larger than 0.3 V/nT. For a calibration larger than 0.3 V/nT, the total mean noise will be smaller than 2.33 pTrms.

The measurements therefore conclusively show that the 1 MΩ feedback resistor should be used to maximise the sensitivity and reduce the quantisation error of voltage noise. The SQUID's internal $1/f$ noise when unshielded however remain undetermined. It is recommended that the manufacturer determine the SQUID's internal $1/f$ noise while exposed to completely static fields, before SQUIDs are purchased.

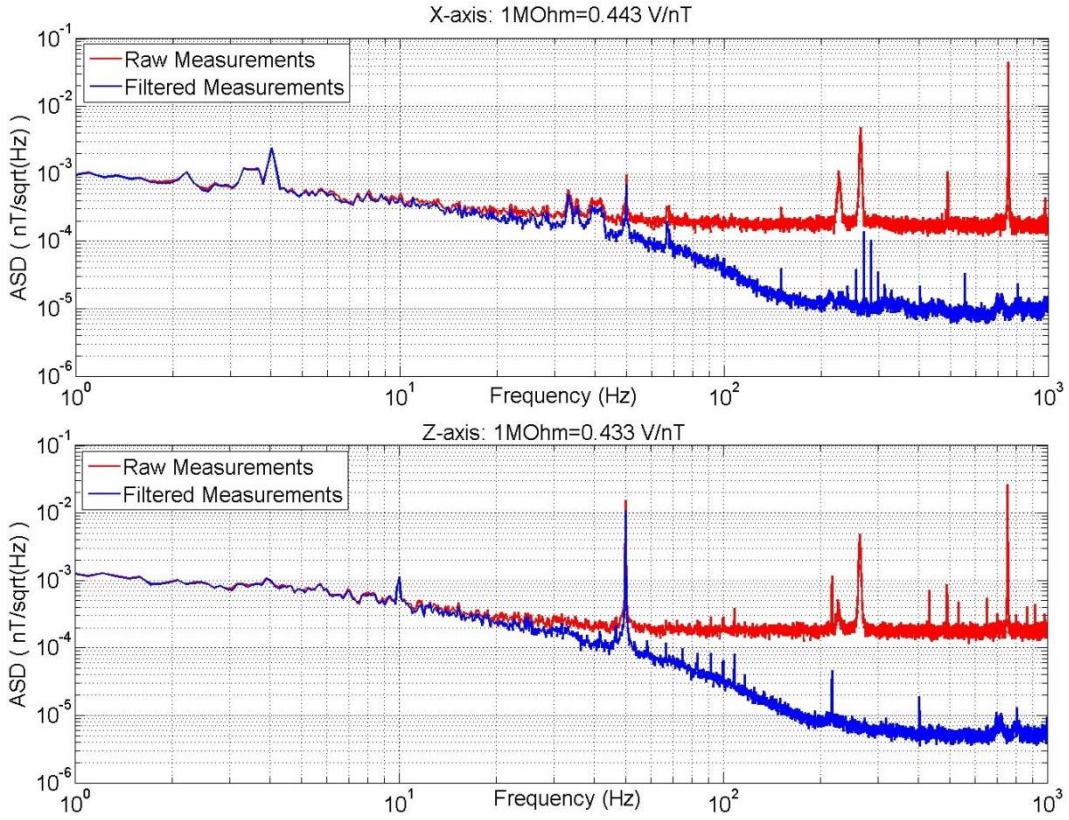

Figure 32: DAQ-system shielded noise spectrum after shield settling time. Geomagnetic field variations are reduced by a factor larger than 50.

Frequency (Hz)	Average Amplitude (mV)
164	0.2
220	0.3
261	2.7
490	0.27
753	8.3

Table 4.1: SQUID electronics internal voltage noise spikes.

4.5 SQUID Thermal Cycling

The Z-axis SQUID was used for thermal cycling with different heater on times to determine the effects of different quench rates when de-fluxing the SQUID. The LN2 needed to be refilled, which allowed the first test to be done for thermal cycling from room temperature. Thereafter the SQUID's 1.1 W heater was used while the SQUID was in tune mode. This allowed seeing the modulation voltage slowly becoming smaller as the SQUID's temperature rose. 8 s of heating was required to raise the SQUID's temperature above its critical temperature. No notable difference was seen in the noise after increasing the heating time up to 30 s. Figure 33 shows the improvement in noise after de-fluxing the SQUID.

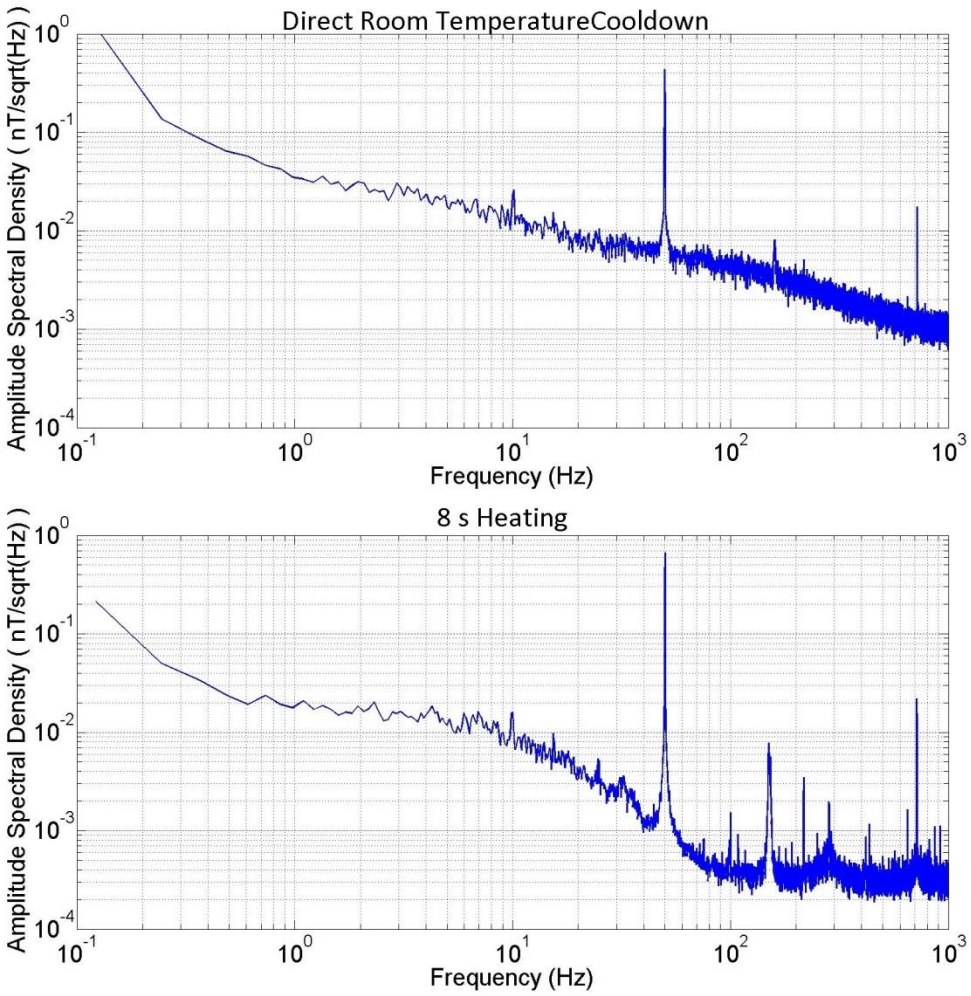

Figure 33: Internal SQUID noise before and after defluxing.

De-fluxing is explained with the Kibble-Zurek theory. As Gordeeva [18] explains, flux trapping is generally "…considered as a mere disturbing factor accompanying the quenching of superconductors". However, the Kibble-Zurek theory explains flux trapping "…is the interplay between the finite speed of the transition and the divergence of the relaxation time during the quench that leads to production of topological defects … (Abrikosov vortices and fluxoids)". Gordeeva also explains that the Kibble-Zurek theory "…appears to be very challenging both for theoreticians and experimentalists. Therefore every new achievement in the field is regarded as significant". The probability of trapping flux increases with smaller quench times. The quench time is inversely proportional to the cooling rate (dT/dt). The quench time at $T = T_c$ is calculated as follows [18]:

$$\tau_Q = T_c \left(\frac{dT}{dt}\right)^{-1} \tag{4.4}$$

The minimum quench time required to negate the probability (probability $< 0.1\%$) of trapping extra flux in HTS SQUIDs can be assumed to be larger than 20 s (approximation from [18], pp. 50). This allows a maximum cooling rate of 4.5 K/s at $T_c = 90$ K.

The excessive noise in the top graph of Figure 33 is due to the high cooling rate of thermal cycling from room temperature, resulting in more flux trapping. Heating the SQUIDs to a lower temperature allows a smaller cooling rate to trap less flux, hence de-fluxing the SQUID. The test suggests that heating times less than 30 s results in the same cooling rate at 90 K for the model M2700 SQUID. It is however possible that the SQUID's noise could be improved further by providing it with an even slower cooling rate. This could be done by controlling the heater's power. Having configurable heater power would allow many different tests, for different heating rates and cooling rates. Star Cryoelectronics could provide a firmware update for minimal costs, which allows the heater power to ramp down rather than immediately shut off. However it would be much better having configurable heater power. The M2700 SQUIDs have been thermal cycled from room temperature several times, without any notable quality degradation.

4.6 Recommendations Summary

The improvements required to allow system stability are:

1. Improving SQUID orientation accuracy
2. Improving LN2 evaporation rate
3. Resetting the PFLs for infinite range and maximum sensitivity
4. Minimising the SQUID cool down rate
5. EMR shielding from 1 kHz for improved accuracy.

Possible developments for SQUID based geomagnetometers are:

1. New probe design with minimal heat transfer, allowing continuous use over long periods with reduced evaporation rates.
2. 3-axis SQUID package for perpendicularity accuracy.
3. SQUID electronics with configurable heater power to control cooling rate.

Further tests and experiments:

1. Measurements with completely static fields need to be done to determine the SQUID's internal $1/f$ noise.
2. Controlled cooling rate with heater, to test the Kibble-Zurek theory. The heater could possibly increase noise if the SQUID cools below the critical temperature while the heater is on.
3. Test the modulation depth and the internal SQUID noise after implementing EMR shields.

Chapter 5

Conclusion

This thesis provided information on the design of a 3-axis geomagnetic magnetometer SQUID system installed at SANSA. Every chapter starts by providing clear motivation for reading the chapter. Conclusions and summaries within the chapters highlight the most important information to be taken from the work. In the first chapter the project's motivation and goals are discussed. The second chapter provides the basic knowledge required when designing a GSS. In the third chapter, the design of the GSS is discussed, providing an easy to follow model on which GSS design can be based. The fourth chapter then analyses the GSS performance and provides information on developments required to improve the performance.

The GSS, only being in the design and installation phase, still requires much improving. Even so, the noise of the unshielded SQUIDs above 10 Hz was shown to be close to the shielded noise of less than 300 fT/$\sqrt{\text{Hz}}$, with $1/f$ noise lower than geomagnetic field variations. This is achieved with commercial HTS SQUIDs, before implementing any developments to improve sensitivity. This justifies the project's research validity. The $1/f$ noise therefore remain to be determined, but following the suggestions provided in chapter 4 should provide promising results. The white noise of the Geomagnetometer SQUID system was determined to contribute less than 3 pTrms noise when operated at maximum sensitivity, with a sampling rate of 125 Hz and filtered above 50 Hz.

List of References

[1] R. L. McPherron, “Magnetic Pulsations: Their Sources and Relation to Solar Wind and Geomagnetic Activity,” *Surveys in Geophysics,* vol. 26, no. 5, pp. 545-592, September 2005.

[2] F. Masci, “On the seismogenic increase of the ratio of the ULF geomagnetic field components,” *Physics of the Earth and Planetary Interiors,* vol. 187, pp. 19-32, 2011.

[3] G. Prattes, K. Schwingenschuh, H. U. Eichelberger, W. Magnes, M. Boudjada, M. Stachel, M. Vellante, U. Villante, V. Wesztergom and P. Nenovski, “Ultra Low Frequency (ULF) European multi station magnetic field analysis before and during the 2009 earthquake at L'Aquila reagrding regional geotechnical information,” *Natural Hazards and Earth System Science,* vol. 11, pp. 1959-1968, 2011.

[4] J. D. Norton, Einstein's Special Theory of Relativity and the Problems in the electrodynamics of moving bodies that led him to it, M. Janssen and C. Lehner, Eds., Cambridge University press, 2004.

[5] W. D. Callister Jr, Materials Science and Engineering: An Introduction, 7 ed., New York: John Wiley & Sons Inc., 2000.

[6] F. T. Ulaby, Fundamentals of Applied Electromagnetics, 5th Edition, Prentice Hall, 2010.

[7] “Tables of Physical & Chemical Constants (16th Edition 1995). 2.6.6 Magnetic properties of materials,” Kaye & Laby Online, Version 1.0 (2005). [Online]. Available: www.kayelaby.npl.co.uk.

[8] R. G. Martín, “Electromagnetic field theory for physicists and engineers: Fundamentals and Applications”.

[9] "Tables of Physical & Chemical Constants (16th Edition 1995). 2.6.5 Dielectric properties of materials," Kaye & Laby Online, Version 1.0 (2005). [Online]. Available: www.kayelaby.npl.co.uk.

[10] H. G. Schantz, "Near Field Phase Behaviour," *Antennas and Propagation Society International Symposium, 2005 IEEE,* vol. 3B, pp. 134-137, 2005.

[11] C. G. Constable and S. C. Constable, "Satellite Magnetic Field Measurements: Applications in Studying the Deep Earth," in *The State of the Planet: Frontiers and Challenges in Geophysics (eds R.S.J. Sparks and C.J. Hawkesworth)*, Washington, D. C., American Geophysical Union, 2013.

[12] D. Regimbald, "Intermagnet Technical Reference Manual," 4.5 ed., B. St-Louis, D. F. Trigg and R. L. Coles, Eds., Edinburgh, UK, Intermagnet, 2011, p. 5.

[13] K. Schlegel and M. Füllekrug, "50 Years of Schumann Resonance," in *Physik in unserer Zeit, Vol. 33*, Wiley-VCH Verlag, 2002, pp. 256-26.

[14] G. A. Saunders and P. J. Ford, The Rise of the Superconductors, CRC PressINC, 2005.

[15] O. S. Chanaa, D. M. C. Hylandb, R. J. Kinseyc, W. E. Boojic, M. G. Blamirec, C. R. Mgrovenord, D. Dew-Hughesb and P. A. Warburton, "Josephson effects in misaligned TI-2212 films," *Physica C: Superconductivity,* Vols. 326-327, pp. 104-110, 1999.

[16] A. Pan, M. Ziese, R. Höhne, P. Esquinazi, S. Knappe and H. Koch, "Surface superconductivity and matching effect in a niobium thin film," *Physica C: Superconductivity,* vol. 301, no. 1-2, pp. 72-84, 1998.

[17] L. F. Cohen and H. J. Hensen, "Open questions in the magnetic behaviour of high-temperature superconductors," *Reports on Progress in Physics,* vol. 60, pp. 1581-1672, 1997.

[18] A. Gordeeva, "Creation of Magnetic Flux in Quenched Superconducting Rings and Josephson Junctions," DTU Physics, 2005.

[19] K. Kadowaki, “Vortex states in high-Tc superconductors and superconductivity in modern nano-science and engineering,” *Science and Technology of Advanced Materials,* vol. 6, no. 6, pp. 589-603, 2005.

[20] W. Buckel and R. Kleiner, Superconductivity: Fundamentals and Applications, 2 ed., WILEY-VCH Verlag GmbH & Co. KGaA, 2004.

[21] J. Clarke and A. L. Braginski, The SQUID Handbook, Vol.1, WILEY-VCH Verlag GmbH & Co. KGaA, 2004.

[22] E. Dantsker, S. Tanaka, P. A. Nilsson, R. Klainer and J. Clarke, “Reduction of 1/f noise in high-Tc dc superconducting quantum interference devices cooled in an ambient magnetic field,” *Applied Physics Letter,* vol. 69, no. 26, pp. 4099-4101, 23 December 1996.

[23] H. C. Yang, S. Y. Yang, H. E. Horng, H. W. Yu, J. H. Chen, J. T. Jeng and H. W. Lin, “Studies of High-Tc YBCO SQUIDs,” *Chinese Journal of Physics,* vol. 38, no. 2, pp. 322-329, 2000.

[24] P. Dixon, *Theory and Applications of RF/Microwave Absorbers, Tech Notes,* Emerson & Cuming Microwave Products.

[25] *EMI Shielding Design Guide,* Tecknit.

[26] P. V. Y. Jayasree, V. S. S. N. Srinivasa, B. Prabhakara Rao and P. Laksman, “Analysis of shielding effectiveness of single, double and laminated shields for oblique incidence of EM waves,” *Progress in Electromagnetic Research B,* vol. 22, pp. 187-202, 2010.

[27] S. Radu, “Engineering Aspects of Electromagnetic Shielding,” Sun Microsystems Inc.

[28] S. A. Wolf, D. U. Gubser and J. E. Cox, “Shielding Of Longitudinal Magnetic Fields With Thin, Closely, Spaced, Concentric Cylindrical Shells With Applications To Atomic Clocks,” *Review of Scientific Instruments,* vol. 50, no. 6, pp. 751-756, 1979.

[29] S. S. Raghuwanshi and G. M. Saxena, “A Generalised Approach To Determination Of Magnetic Shielding Factor For Physics Package Of Rb Atomic Clocks,” arXiv:0910.4031 [physics.gen-ph], 2009.

[30] *Magnetic Shielding: Principles, Delivery Programme, Measurements,* Sekels GmbH Magnetic Shielding.

[31] “MuShield Magnetic Shielding That Works,” MuShield, [Online]. Available: www.mushield.com/design-guide.shtml. [Accessed 12 August 2013].

[32] Star CryoElectronics, “pcSQUID User's Manual,” [Online]. Available: www.starcryo.com/pcSQm21.pdf.

[33] J. R. Davis, Copper and Copper Alloys, ASM International, 2001.

[34] “Permeability (electromagnetism),” Wikipedia, [Online]. Available: http://en.wikipedia.org/wiki/Permeability_(electromagnetism). [Accessed 10 11 2013].

[35] Magnetic Shield Corp, “Magnetic Shield Corporation FAQs,” 2012. [Online]. Available: http://www.magnetic-shield.com/pdf/what_effects_does_cryogencially_cooling_the_magnetic_material_hav.pdf. [Accessed 10 Nov 2013].

[36] R. L. Fagaly, “SQUID Instruments and Applications,” *Review of Scientific Instruments,* 2005.

[37] L. J. Janse van Vuuren, A. Kilian, T.-J. Phiri, C. J. Fourie, E. Pozzo di Borgo, P. Febvre, E. F. Saunderson, E. T. Lochner and D. J. Gouws, “Implementation of an unshielded SQUID as a geomagnetic sensor,” in *IEEE AFRICON 2013*, Mauritius, 2013.

[38] “Tables of Physical & Chemical Constants (16th Edition 1995). 2.3.6 Specific heat capacities,” Kaye & Laby Online, Version 1.0 (2005). [Online]. Available: www.kayelaby.npl.co.uk.

[39] J. E. Jankowski, Convective Heat Transfer Model for Determing Quench Recovery of High Temperature Superconducting YBCO in Liquid Nitrogen, Massachusetts Institute of Technology, Sep 2004.

Appendices

A.1. Matlab Code: Magnetic Shielding

```
function [] = doubleSHIELD_EngCalcs_Mod(u1, p, CRYO, H, IDmin,
ODmax,tmax,L_spec, w_spec)

%   p = polynomial coefficients of Mu-metal permeability curve-fit
%   using function=CoNetic.
%   u1 = initial permeability of inside shield layer
%   CRYO = ratio of reduced permeability at cryogenic temperture
%   H = external field
%   IDmin = minimum inner diameter
%   ODmax = maximum outer diamter
%   tmax = maximum thickness
%   L_spec = specified length
%   w_spec = specified shield width (OD-ID)/2

r1=IDmin/2;
inc = 250;

switch nargin
    case 7
        Lc=((ODmax+IDmin)/2)*3;
        wc = (ODmax-IDmin)/2/2;
    case 8
        Lc=L_spec;
        wc = (ODmax-IDmin)/2/2;
    case 9
        Lc=L_spec;
        wc = w_spec;
end

%%%%%%%%%%%%%%%%%%%%%%%%%%%%%%%%%%%%%%%%%%%%%%%%%%%%%%%%%%%%%%%%%%%
%%%Keeping length constant, varying width and thickness
 w=(ODmax-IDmin)/inc:(ODmax-IDmin)/inc:(ODmax-IDmin)/2;
t=(tmax/inc:tmax/inc:tmax);
r2=zeros(length(t),length(w));
SF_l_dtdw=zeros(length(t),length(w));
SF_t_dtdw=zeros(length(t),length(w));
u2=zeros(length(t),length(w));
for y = 1 : length(t)
    for x = 1 : length(w)

        if w(x) >= 2*t(y)
            r2(y,x) = r1 + w(x) - t(y);
        end

        if w(x) < 2*t(y)
            r2(y,x)=0;
        end

        LR2 = Lc/r2(y,x);

        B2=2.5*H*r2(y,x)/t(y);
```

```
        u2(y,x)=mu_curve(B2,p);

        SF_t_dtdw(y,x)= SF_t(u1*CRYO, u2(y,x)*CRYO, t(y), r1,
r2(y,x));
        SF_l_dtdw(y,x)= SF_l(u1*CRYO, u2(y,x)*CRYO, t(y), r1,
r2(y,x), LR2);

    end
end


%%plot figures for varying width and thickness
subplot(2,2,1)
surf(w(:)+r1, t(:), SF_t_dtdw);

subplot(2,2,2)
surf(w(:)+r1, t(:), SF_l_dtdw);

%%%%%%%%%%%%%%%%%%%%%%%%%%%%%%%%%%%%%%%%%%%%%%%%%%%%%%%%%%%%%%%%
%%%Keeping width constant, varying length and thickness
LR2 = 2:6/inc:8-6/inc;      % LR2 is x-axis
t=(tmax/inc:tmax/inc:tmax);   % t is y-axis
r2=zeros(length(t),1);      % r2 only changes as thickness changes
SF_t_dtdL=zeros(length(t),length(LR2));
SF_l_dtdL=zeros(length(t),length(LR2));
for y = 1 : length(t)
    for x = 1 : length(LR2)

        if wc >= 2*t(y)
            r2(y) = r1 + wc - t(y);
        end
        if wc < 2*t(y)
            r2(y)=0;
        end

        B2=H*2.5*r2(y)/t(y);
        u2=mu_curve(B2,p);


        SF_t_dtdL(y,x)=SF_t(u1*CRYO, u2*CRYO, t(y), r1, r2(y));
        SF_l_dtdL(y,x)= SF_l(u1*CRYO, u2*CRYO, t(y), r1, r2(y),
LR2(x));

    end
end

%%plot figures for varying length and thickness
subplot(2,2,3)
surf(LR2(:), t(:), SF_t_dtdL);
subplot(2,2,4)
surf(LR2(:), t(:), SF_l_dtdL);

end
```

```
%%%%%%%%%%%%%%%%%%%%%%%%%%%%%%%%%%%%%%%%%%%%%%%%%%%%%%%%%%%%%%%%%%%%%%%%%%%%
%%% Transverse shielding factor
function [SFt]= SF_t(u1, u2, t, r1, r2)

        d = 0.5*(1-(r1/r2)^2);
        SF_t2 = 0.5*u2*t/r2;
        SF_t1 = 0.5*u1*t/r1;
        SFt = SF_t1*SF_t2*d + SF_t1 + SF_t2;
end

%%%%%%%%%%%%%%%%%%%%%%%%%%%%%%%%%%%%%%%%%%%%%%%%%%%%%%%%%%%%%%%%%%%%%%%%%%%%
%%% Longitudinal shielding factor
function [SFl] = SF_l(u1, u2, t, r1, r2, LR2)

        if LR2 <= 6
            f = 0.75;
        end
        if LR2 > 6
            f = 0.75 + (LR2-6)/4*(0.9-0.75);
        end
        if LR2 > 10
            f = 0.9+(LR2-10)/LR2*(1-0.9);
        end
        D = (1+1/LR2)/(2*f*(1+LR2));
        SF_l2 = 2*D*u2*(t/r2)/(1+1/LR2);

        dL= LR2*r2;
        LR1 = dL/r1;
        if LR1 <= 6
            f = 0.75;
        end
        if LR1 > 6
            f = 0.75 + (LR1-6)/4*(0.9-0.75);
        end
        if LR1 > 10
            f = 0.9+(LR1-10)/LR1*(1-0.9);
        end
        D = (1+1/LR1)/(2*f*(1+LR1));
        SF_l1 = 2*D*u1*(t/r1)/(1+1/LR1);


        LR = dL/((r1+r2)/2);
        if LR <= 6
            f = 0.75;
        end
        if LR > 6
            f = 0.75 + (LR-6)/4*(0.9-0.75);
        end
        if LR > 10
            f = 0.9+(LR-10)/LR*(1-0.9);
        end
        d = 0.5*(1-(r1/r2)^2);
        SFl = 2*SF_l1*SF_l2*f*d + SF_l1 + SF_l2;

end
```

```
%%%%%%%%%%%%%%%%%%%%%%%%%%%%%%%%%%%%%%%%%%%%%%%%%%%%%%%%%%%%%%%%%%%%%%%%
%%% Calculate permeability with induced field (B) for Mu-metal
curve fit polynomials (p)
function u = mu_curve(B,p)

%   u = relative permeability
%   B = Induced field (Gauss)
%   p = polynomial coefficients of Mu-metal permeability curve-fit

u = 0;
      for i = 1:length(p)
            u = u + p(i)*B^(length(p)-i);
      end
      if u < 1
            u = 1;
      end

end

%%%%%%%%%%%%%%%%%%%%%%%%%%%%%%%%%%%%%%%%%%%%%%%%%%%%%%%%%%%%%%%%%%%%%%%%
%%% Polynomials of Mu-metal curve-fit, using B-H curve data
function p=CoNetic(n)

%   Co-Netic AA prefection annealed B-H curve data
%   B = Induced field (Gauss)
%   u = relative permeability/1000
%   p = polynomial coefficients of CoNetic used in function
mu_curve

B=[0.001 0.01 0.1 1 10 20 30 40 50 60 70 80 90 100 200 300 400 500
600 700 800 900 1000 2000 3000 4000 5000 6000 7000 7100 7200 7300
7400 7500 8000 9000 10000];

u=[30 30 30 30 35 50 60 70 75 80 85 90 95 100 130 140 160 190 200
210 230 250 260 380 440 430 310 150 30 10 1 0.1 0.01 0.001 0.001
0.001 0.001];

u=u*1000;
p=polyfit(B,u,n);

end
```

A.2. Matlab Code: Amplitude Spectral Density

```
function  []=ASD(y,Fs)

%=====================================================================
%
%  Computes the Amplitude spectral density Y(f) of 1D signal y(t)
%  with known sample rate Fs.
%
%=====================================================================

if nargin<2
    error(' Sampling frequency is required!');
end

%Shift data
y=y-mean(y);

%Create Sample window. Fs/Samples = frequency resolution
Samples= 16384;
win = hamming(Samples,'periodic');
y1 = buffer(y, Samples, Samples/2);
y1 = (  y1' * diag(win)  )';

%Windowed Amplitude Spectral Density
Y=abs(fft(y1,Samples)/sum(win))/(sqrt(Fs/Samples));

%Mean ASD
Y=mean(Y,2);

%Frequency axis
f=(Fs/Samples)*(0:Samples/2-1);

%Plot
loglog(f,Y(1:length(f)),'b','linewidth',2); %ASD mean
xlabel('Frequency (Hz)','Fontsize',30);
ylabel('Amplitude Spectral Density ( nT/sqrt(Hz))','Fontsize',30);
grid on;
axis([1*10^-4 1000 1*10^-6 1000]);
title('Title','Fontsize',30)
fig = gcf;
style = hgexport('factorystyle');
style.Bounds = 'tight';
hgexport(fig,'-clipboard',style,'applystyle', true);
drawnow;
set(gcf, 'Position', get(0,'Screensize')); % Maximize figure.
set(gca, 'fontsize',30);
end
```

A.3. SQUID vs. Fluxgate Correlation

```
%%%%% Angle Correlation factors %%%%%
b=-10/180*pi:0.1/180*pi:10/180*pi;
a=-15/180*pi:0.1/180*pi:15/180*pi;
cor=zeros(length(b),length(a));

for j=1:length(b)    %%% Z-XY plane
for i=1:length(a)   %%% X-Y plane

FL=(Xfluxgate*cos(a(i))+Yfluxgate*sin(a(i)))*cos(b(j))+Zfluxgate*
sin(b(j))-
mean((Xfluxgate*cos(a(i))+Yfluxgate*sin(a(i)))*cos(b(j))+Zfluxgate
*sin(b(j)));

cor(j,i)=corr(FL,SQD(1:20:length(SQD))); %%% FL @ 1Hz, SQD @ 20Hz

end
end

surf(a/pi*180,b/pi*180,cor)
%%%%%%%%%%%%%%%%%%%%%%%%%%%%%%%%%%%%%%%%
```

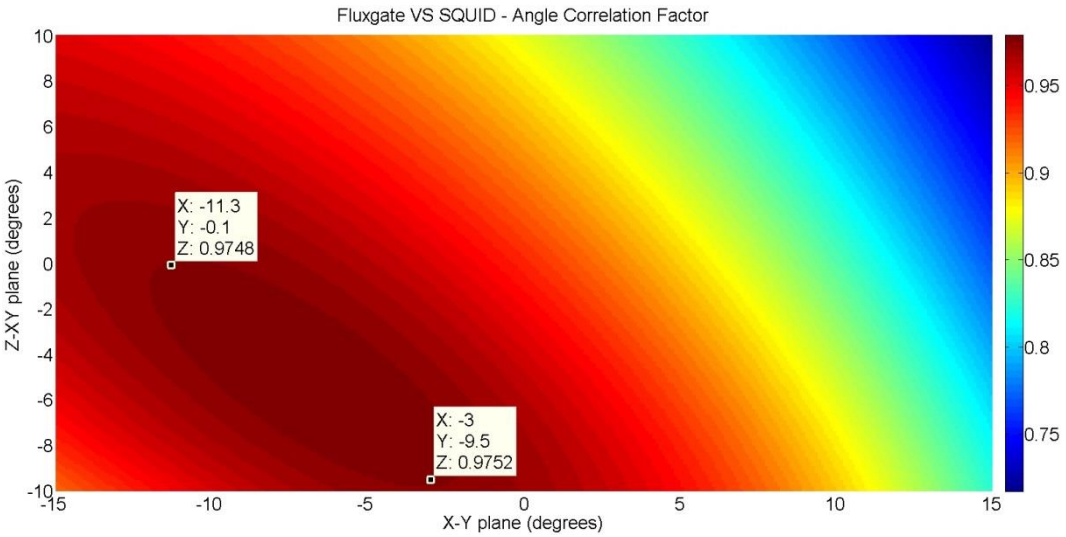

Figure A.3.1: Correlation Factors. X-axis tilts the Fluxgate XY plane from -15˚ to 15˚. Y-axis tilts the Fluxgate vertical plane from -10˚ to 10˚.

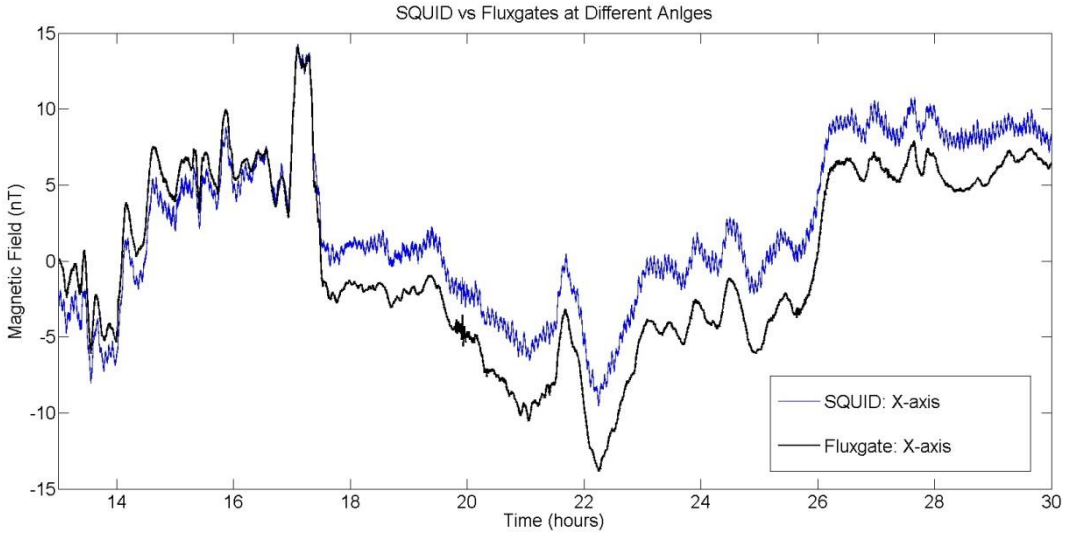

Figure A.3.2: Raw SQUID vs Fluxgate measurements.

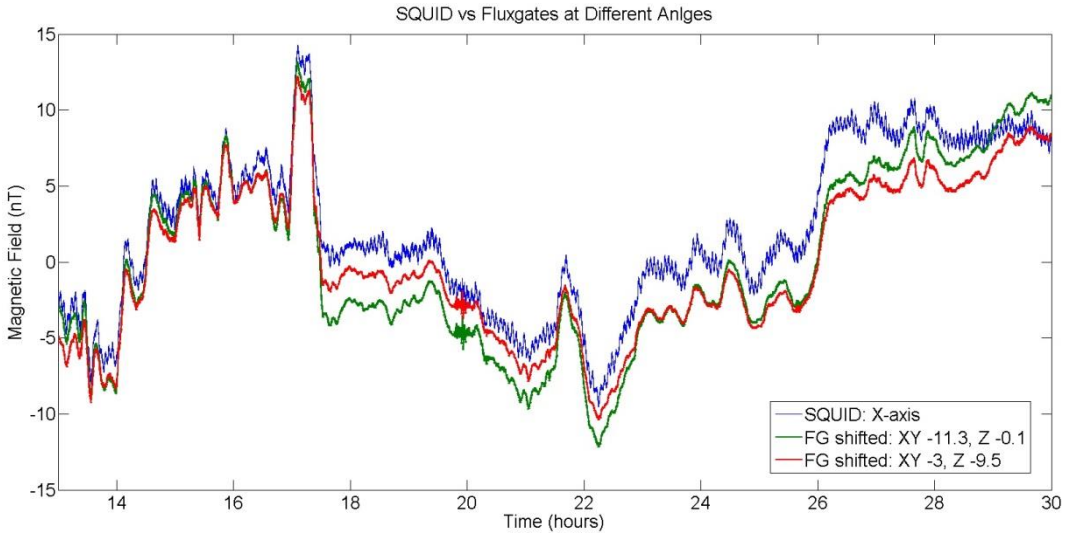

Figure A.3.3: SQUID vs Fluxgates with planes shifted to different angles.

B.1. Datasheet: M2700 SQUID

STAR Cryoelectronics

HTS Magnetometer
M2700

1 DESCRIPTION

The Model M2700 High-T_c dc SQUID magnetometer is dual-SQUID magnetometer fabricated from a single layer of $YBa_2Cu_3O_{7-x}$ (YBCO) using a step-edge grain-boundary Josephson junction process. The magnetometer design consists of a large-area pickup loop connected in parallel with two SQUID inductances. Either SQUID may be biased individually, or the pair may be biased in serial mode to increase the output voltage swing by up to a factor of two. An external magnetic field sensed by the pickup loop is coupled to the SQUID by direct injection. Excellent low-noise performance is achieved with this single-layer design, even at low frequencies (<1 Hz) using AC current bias.

The magnetometer die are mounted on a standard FR-4 button-shaped printed circuit board. Current and voltage connections to the chip are made using gold ribbon ultrasonic wire-bonds. Two 51 Ω resistors connected in series (110 Ω at 77 K) mounted on the button-shaped pc board allow the magnetometer to be heated above T_c to deflux the SQUID if necessary. Embedded in the pc board button of the Model M1000 magnetometer is a wire-wound copper feedback coil for closed-loop operation using standard feedback electronics. The magnetometer button is encapsulated and hermetically sealed using a glass-epoxy (G-10) cover and attached to a G-10 sensor package that houses an impedance matching circuit for conventional room temperature readout electronics. The package also includes a mounting flange that is fitted with a 10-pin LEMO connector to simplify electrical connections to the magnetometer. Optional mating cryogenic cables are available from STAR Cryoelectronics. For applications requiring a small form factor, two different magnetometer button-only configurations are available. The standard button described above is available with two tapped screw holes for rear mounting or an optional button design is available with clearance holes through the button to simplify installation from the front.

The M2700 dc SQUID magnetometer is simple to operate using pcSQUID™, STAR Cryoelectronics' advanced PC-based closed-loop feedback and readout electronics. For button-only installations, the single-transformer option in the feedback loop electronics may be used, eliminating the need for any cooled matching circuitry.

FEATURES

- Low rms field noise of better than 300 fT/Hz^{½}
- Miniature pickup loop (2.7 mm × 2.7 mm OD) for applications requiring moderate spatial resolution.
- Compact, hermetically-sealed magnetometer package design.
- Standard sensor assembly includes cooled matching circuitry and LEMO connector interface; optional right-angle mounting is available for transverse field measurements.
- Optional magnetometer button-only package may be installed without any cooled matching circuit for applications requiring small foot print.

25-A Bisbee Court, Santa Fe, NM 87508
Phone: 505.424.6454 • FAX: 505.424.8225 • Email: info@starcryo.com

2 SPECIFICATIONS

Table 2.1 Specifications, M2700 dual-SQUID magnetometer chip.

Parameter	Value			
Pickup loop size	2.7 mm × 2.7 mm OD, 0.9 mm × 0.9 mm ID			
Feedback coil inductance L_f	Embedded in package, see Figure 3.2			
Operating temperature	76 to 78 K (77 K typical)			
	Min.	Typ.	Max.	Unit
SQUID critical current $2I_C$	10	50	100	μA
SQUID resistance $R/2$	-	3	-	Ω
Feedback mutual inductance[1] $1/M_f$	-	17	-	$\mu A/\Phi_0$
Voltage swing ΔV	-	30	-	μV
Field calibration	-	33	-	nT/Φ_0
Field noise $S_B^{1/2}(f)$, f > 10 Hz	-	-	300	$fT/Hz^{1/2}$
Temp. coefficient at 77K	-	2.5	-	nT/K
Heater power (Watts at 77 K)	-	1.1	-	W
Heat time to normalize	-	20	-	Sec
Storage temperature (dry)	0	20	40	°C

[1]M1000 packaged in LEMO package assembly.

3 ROOM-TEMPERATURE RESISTANCES

(See Safe Handling Procedures before making any resistance measurements on the SQUID)

Table 3.1 M2700 packaged in LEMO package assembly (see Figure 3.1).

Contacts	Pins[1] (+/-)	Resistance [Ω]
Bias	8,9	210
Voltage	2,3	5
Heater	1,4	105
Modulation	7,10	6
Feedback[2]	6,5	6

[1]See mechanical specifications, magnetometer sensor assembly, Figure 3.1.
[2]Modulation and Feedback are summed inside sensor assembly.

Table 3.2 M2700 packaged in button package assembly (see Figure 3.2).

Pads	Resistance [Ω]
±I1, ±V1, ±I2, ±V2	<500
+I1/+V1, +I2/+V2, -I/-V	<10
±M	<10
±H	105

Table 3.3 M2700 packaged in M19 package assembly (see Figure 3.3).

Pads	Resistance [Ω]
±I1, ±V1, ±I2, ±V2	<500
+I1/+V1, +I2/+V2, -I/-V	<10
±H	100

B.2. Datasheet: Z-axis SQUID Calibration Certificate

STAR Cryoelectronics
25-A Bisbee Court • Santa Fe, NM 87508
Tel.: 505.424.6454 • FAX: 505.424.8225 • Email: info@starcryo.com
Internet: http://www.starcryo.com

SQUID Type:	M2780j12v1	**Process No.:**	JD304	**ID:**	F
SQUID:	2	**Customer:**	Stellenbosch Univ.		
S/N:	H225				
Feedback Coil Coupling:	13.2 μA/Φo	Mutual Inductance:	0.16 nH	Coil Inductance:	32 μH
Field Calibration B/Φ_0	33.5 nT/Φo				

Field noise (measured in closed-loop mode)

Mode:	2-XFMR				
Feedback Loop Cal.:	1.318 V/Φo	SQUID Type:	Custom	Sensitivity:	-
	25.39 nT/V	Feedback Resistor:	100 kΩ	Integrator Cap.:	10 nF
		Heater ON time:	10 sec	Heater OFF time:	30 sec

Cooled in zero field:		**Cooled in 80 μT field:**		
Bias (128 Hz AC):	26.81 μA	Bias (128 kHz AC):	μA	(Tuned to first peak)
Modulation:	6.18 μA	Modulation:	μA	
Skew:	7.79 %	Skew:	%	
Compensation:	21.95 %	Compensation:	%	
Output:	7.76 Vpp			
Field noise (10 Hz):	168 $fT/\sqrt{Hz}$	Field noise (10 Hz):	$fT/\sqrt{Hz}$	
Field noise (1 kHz):	149 $fT/\sqrt{Hz}$	Field noise (10 kHz):	$fT/\sqrt{Hz}$	

Tested by:	RC	**Date:**	9-Apr-11	**Pass/Fail:**	Pass

H225.xls Printed 4/14/2011

B.3. Datasheet: X-axis SQUID Calibration Certificate

STAR Cryoelectronics
25-A Bisbee Court • Santa Fe, NM 87508
Tel.: 505.424.6454 • FAX: 505.424.8225 • Email: info@starcryo.com
Internet: http://www.starcryo.com

SQUID Type:	M2780j12v1	**Process No.:**	JD304	**ID:**	B
SQUID:	2	**Customer:**	Stellenbosch Univ.		
S/N:	H224				
Feedback Coil Coupling:	10.5 μA/Φo	Mutual Inductance:	0.20 nH	Coil Inductance:	32 μH
Field Calibration B/Φ_0	33.5 nT/Φo				

Field noise (measured in closed-loop mode)

Mode:	2-XFMR				
Feedback Loop Cal.:	1.047 V/Φo	SQUID Type:	Custom	Sensitivity:	-
	31.96 nT/V	Feedback Resistor:	100 kΩ	Integrator Cap.:	10 nF
		Heater ON time:	10 sec	Heater OFF time:	30 sec

Cooled in zero field:		**Cooled in 80 μT field:**		
Bias (128 Hz AC):	54.07 μA	Bias (128 kHz AC):	μA	(Tuned to first peak)
Modulation:	4.51 μA	Modulation:	μA	
Skew:	-5.372 %	Skew:	%	
Compensation:	12.70 %	Compensation:	%	
Output:	6.00 Vpp			
Field noise (10 Hz):	186 $fT/\sqrt{Hz}$	Field noise (10 Hz):	$fT/\sqrt{Hz}$	
Field noise (1 kHz):	272 $fT/\sqrt{Hz}$	Field noise (10 kHz):	$fT/\sqrt{Hz}$	

Tested by:	RC	**Date:**	5-Feb-11	**Pass/Fail:**	Pass

H224.xls Printed 2/20/2011

B.4. Datasheet: Bio34 Dewar

Bio Series

Canister-Equipped Refrigerators

Product Features

- 11 models, from 2 to 36 litres capacity
- Strong, lightweight aluminium construction
- High thermal efficiency - ultra-low evaporative losses
- Numbered index location points for canisters
- Heavy-duty lockable enclosures offer excellent security
- 1.2, 2.0 or 5.0ml cryovials held on canes
- Roller bases and level alarms available

The Bio Series of refrigerators provide two lines as alternatives for storage of biological material, with High Capacity or Extended Hold Time variants.

All Bio Series containers are designed and manufactured in our purpose-built ISO9001 accredited facility using the very latest CAD technology. Advanced super-insulation and ultra-high vacuum techniques allow incredibly long holding times.

Included with every Bio Series container are internal storage canisters suitable for the storage of biological material in cryovials on canes or straws in goblets.

High Capacity Models

These units allow the storage of large quantities of biological material while still offering excellent holding times. All High Capacity units have wider neck openings for easy access.

Extended Hold-Time Models

With narrower neck openings for outstanding thermal efficiency, the extended hold time models offer long term storage possibilities with minimal LN2 consumption.

Canes and sleeves are available as well as a range of goblets and lifters for straw storage.

The Battery CryoGuard offers an LN2 level alarm facility without restricting use to areas where mains electricity is available.

Technical Data

	Extended Hold-Time						High Capacity				
Model	**Bio 2**	**Bio 3**	**Bio 8**	**Bio 10**	**Bio 20**	**Bio35**	**Bio 12**	**Bio 21**	**Bio 22**	**Bio 34**	**Bio 36**
Part No.	9902015	9902030	9902050	9902060	9902080	9902120	9902070	9902095	9902096	9902110	9902130
LN2 Capacity (litres)	2	3	8	10	20	35	12	21	21	34	36
Evaporation Rate (litres/day)	0.08	0.11	0.10	0.10	0.10	0.10	0.19	0.19	0.28	0.18	0.30
Static Holding Time (days)	25	27	80	100	200	350	63	110	75	189	120
[1]Field Working Time (days)	16	17	50	63	125	219	39	69	47	118	75
Weight Empty (kg)	3	4.3	8.6	7.9	11.1	18.6	10.8	15.6	15.7	17.8	19.1
Weight Full (kg)	4.6	6.7	15.1	16	27.3	46.9	20.4	32.6	32.7	45.3	47.4
Neck Diameter (mm)	32	51	51	51	51	51	70	89	120	89	120
Overall Height (mm)	390	464	475	640	640	730	470	579	537	710	710
Overall Diameter (mm)	185	216	407	305	407	480	408	480	480	480	480
Number of Canisters	3	6	6	6	6	6	9	6	10	6	10
Canister Dimensions D (mm)	25	38	38	38[2]	38[2]	38[2]	46	68	73	69	73
H (mm)	120	120	120	275	275	275	120	120	120	275	275
2ml Vial Capacity	NA	NA	NA	180	180	180	NA	NA	NA	684	1020
Straw Capacity (0.25cc	360	1200	1200	2400	2400	2400	4680	4920	8200	9840	16400
0.5cc)	120	500	500	1000	1000	1000	2200	2300	3800	4200	7800
Roller Base Part No.	NA	NA	9902082	NA	9902082	9902112	9902082	9902112	9902112	9902112	9902112
Mains CryoGuard Part No.	9702041	9702041	9702041	9702041	9702041	9702041	9702041	9702041	9702041	9702041	9702041
Battery CryoGuard Part No.	9702000	9702000	9702000	9702000	9702000	9702000	9702000	9702000	9702000	9702000	9702000
Temperature Logger Part No.	9701321	9701321	9701321	9701321	9701321	9701321	9701321	9701321	9701321	9701321	9701321

Notes
1. Field working time is a calculated value, this may vary according to container usage.
2. 38mm x 120mm canisters are also available for this model.

8 Tel: +44(0)191-4164104 Fax: +44(0)191-4150369 Email: cryobiology@statebourne.com

B.5. Datasheet: Conetic Mu-metal

Physical and Magnetic Data on Shielding Alloys

Available Co-Netic Sizes	Co-Netic AA Perfection Annealed	Co-Netic AA Stress Annealed*	Co-Netic B Stress Annealed*
Specific Gravity	8.74	8.74	8.18
Coefficient of Expansion, per °C x 10^{-6}	12.6	12.6	8.3
Tensile Strength, PSI x 10^3	64	85	80
Yield Strength, PSI x 10^3	18.5	33	27
Modulus of Elasticity, PSI x 10^6	25	30	24
Hardness, Rockwell B	50 Ref.	70 Ref.	68 Ref.
Elongation in 2 inches	27%	32%	32%
Melting Point	2650°F 1454°C	2650°F 1454°C	2600°F 1427°C
Thermal Conductivity (cal/sec/cm^2/cm/°c) at 20°	.138	.138	.037
Electrical Resistivity Micro-ohm-centimeters	55	55	48
Saturation Induction (Gauss)	8,000	After required annealing is done, magnetic properties are same as those for Perfection Annealed sheet.	15,000*
Initial Permeability	30,000		8,000*
Permeability at 40 B	75,000		12,000*
Permeability at 200 B	135,000		30,000*
Maximum Permeability	450,000		150,000*
Induction at μ max.	3,000		7,000*
Coercive Force Hc,Oersteds	.015		.05
Curie Temp.	850°F 454°C	850°F 454°C	840°F 449°C
Minimum Operating Temp.	4°K	4°K	4°K

Note: Magnetic data is for sheet material measured in a D.C. field.

**Stress annealed material must be annealed after fabrication for optimum magnetic shielding properties.*